

DTIC File Copy

8501950

(2)

AFATL-TR-89-41

Taylor Impact Testing

AD-A215 018

J W House

UNIVERSITY OF KENTUCKY
LEXINGTON, KENTUCKY, 40506-0046

SEPTEMBER 1989

DTIC
ELECTE
SEP 25 1989
S B D

FINAL REPORT FOR PERIOD JUNE 1987 - JANUARY 1989

APPROVED FOR PUBLIC RELEASE; DISTRIBUTION UNLIMITED

AIR FORCE ARMAMENT LABORATORY

Air Force Systems Command ■ United States Air Force ■ Eglin Air Force Base, Florida

89 9 25 018

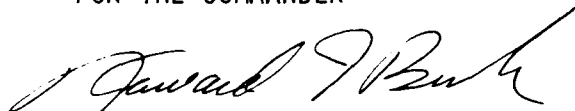
NOTICE

When Government drawings, specifications, or other data are used for any purpose other than in connection with a definitely related Government procurement operation, the United States Government thereby incurs no responsibility nor any obligation whatsoever; and the fact that the Government may have formulated, furnished, or in any way supplied the said drawings, specifications, or other data, is not to be regarded by implication or otherwise as in any manner licensing the holder or any other person or corporation, or conveying any rights or permission to manufacture, use, or sell any patented invention that may in any way be related thereto.

The AFATL STINFO program manager has reviewed this report, and it is releasable to the National Technical Information Service (NTIS). At NTIS, it will be available to the general public, including foreign nations.

This technical report has been reviewed and is approved for publication.

FOR THE COMMANDER



HOWARD J. BUSH, COL, USAF
Chief, Munitions Division

If your address has changed, if you wish to be removed from our mailing list, or if the addressee is no longer employed by your organization, please notify AFATL/MNW, Eglin AFB FL 32542-5434.

Copies of this report should not be returned unless return is required by security considerations, contractual obligations, or notice on a specific document.

UNCLASSIFIED

SECURITY CLASSIFICATION OF THIS PAGE

REPORT DOCUMENTATION PAGE

Form Approved
OMB No. 0704-0188

1a. REPORT SECURITY CLASSIFICATION Unclassified			1b. RESTRICTIVE MARKINGS		
2a. SECURITY CLASSIFICATION AUTHORITY			3. DISTRIBUTION / AVAILABILITY OF REPORT Approved for public release; distribution is unlimited		
2b. DECLASSIFICATION / DOWNGRADING SCHEDULE			5. MONITORING ORGANIZATION REPORT NUMBER(S) AFATL-TR-89-41		
4. PERFORMING ORGANIZATION REPORT NUMBER(S) N/A			7a. NAME OF MONITORING ORGANIZATION Warheads Branch Munitions Division		
6a. NAME OF PERFORMING ORGANIZATION The Graduate School of University of Kentucky		6b. OFFICE SYMBOL (If applicable)	7b. ADDRESS (City, State, and ZIP Code) Air Force Armament Laboratory Eglin AFB FL 32542-5434		
6c. ADDRESS (City, State, and ZIP Code) University of Kentucky Lexington KY 40506-0046		9. PROCUREMENT INSTRUMENT IDENTIFICATION NUMBER F08635 87-C-0125			
8a. NAME OF FUNDING / SPONSORING ORGANIZATION Munitions Division		8b. OFFICE SYMBOL (If applicable) AFATL/MNW	10. SOURCE OF FUNDING NUMBERS		
8c. ADDRESS (City, State, and ZIP Code) Air Force Armament Laboratory Eglin AFB FL 32542-5434		PROGRAM ELEMENT NO. 62602F	PROJECT NO. 2502	TASK NO. 06	WORK UNIT ACCESSION NO. 28
11. TITLE (Include Security Classification) Taylor Impact Testing					
12. PERSONAL AUTHOR(S) Joel W. House					
13a. TYPE OF REPORT Final		13b. TIME COVERED FROM June 87 TO Jan 89		14. DATE OF REPORT (Year, Month, Day) September 1989	
15. PAGE COUNT 129					
16. SUPPLEMENTARY NOTATION Availability of report is specified on verso of front cover.					
17. COSATI CODES			18. SUBJECT TERMS (Continue on reverse if necessary and identify by block number)		
FIELD	GROUP	SUB-GROUP	Plasticity, yield strength, microstructure, fracture elasticity.		
1904	1906	1106			
19. ABSTRACT (Continue on reverse if necessary and identify by block number)					
<p>The reaction of armor to penetration by a projectile is an interesting and important area of science. To assist the armor and armor penetrator designers, several penetration models have been developed. These models require data on the behavior of material under high strain rate conditions resulting from impact. In a paper published in 1948, G.I. Taylor proposed an impact experiment and concomitant analysis to help interpret dynamic material behavior. This experimental technique remains in general use today even though there have been many attempts over the years to modify Taylor's analysis of the test. Ultimately, the data obtained from such "Taylor" tests are used in models of penetration.</p> <p>This report presents a critical discussion of the Taylor test, some of the experimental setups for its performance, and one current analysis of the test. In addition, actual experimental results are presented and analyzed, and the resulting impact induced material microstructures are studied.</p>					
20. DISTRIBUTION / AVAILABILITY OF ABSTRACT <input type="checkbox"/> UNCLASSIFIED/UNLIMITED <input checked="" type="checkbox"/> SAME AS RPT. <input type="checkbox"/> DTIC USERS			21. ABSTRACT SECURITY CLASSIFICATION Unclassified		
22a. NAME OF RESPONSIBLE INDIVIDUAL Leonard L. Wilson			22b. TELEPHONE (Include Area Code) 904-882-2141		22c. OFFICE SYMBOL AFATL/MNW

PREFACE

This report describes an experimental and analytical approach to the determination of dynamic material behavior. Experimental data was collected to verify and refine a one-dimensional predictive model being developed as a design tool for weapon designers. The work was accomplished under contract F08635-87-C-0125, program element 62602F, JON 25020628, during the period from June 1987 to January 1989. The analytical and metallurgical work was accomplished by Mr. Joel W. House at the Graduate School of the University of Kentucky.

The Taylor Impact tests were conducted on Eglin Test Site C-64B. Mr. Leonard L. Wilson of the Air Force Armament Laboratory, Munitions Division, Warhead Branch (MNW) was the program manager.

Accession For	
NTIS GRA&I	<input checked="checked" type="checkbox"/>
DTIC TAB	<input type="checkbox"/>
Unannounced	<input type="checkbox"/>
Justification	
By	
Distribution/	
Availability Codes	
Avail and/or	
Dist	Special
A-1	

Acknowledgement

The author thanks his adviser, Dr. P. P. Gillis; and Dr. S. E. Jones, Dr. J. C. Foster Jr., and Dr. R. J. De Angelis for their guidance throughout this investigation.

The author is grateful to Mr. Leonard Wilson. Mr. Wilson's many years of experience conducting terminal ballistic tests were invaluable to this investigation.

The author is indebted to Kenneth Boggs for his assistance with the microstructural investigation.

TABLE OF CONTENTS

Section	Title	Page
I	INTRODUCTION	
	Dynamic Material Behavior	1
II	ONE-DIMENSIONAL MODELS	
	1. Background.	4
	2. Taylor's Analysis	5
	3. Improved Analysis by Taylor	10
	4. Hawkyard's Analysis	13
	5. α/β Analysis.	14
	6. Experimental Matrix	19
III	EXPERIMENTAL APPARATUS	
	1. Background.	21
	2. Description of the Experimental Apparatus	22
	3. Velocity Measurement Techniques	26
	4. Test Procedures	31
	5. Postmortem Measurements	35
IV	ANALYSIS OF TEST RESULTS	
	1. Introduction.	36
	2. Postmortem Measurement Reliability	37
	3. Static and Dynamic Strengths.	39
	4. Sensitivity Analysis.	40
	5. Effect of Specimen Geometry	43
	6. Mushroom Growth	50
	7. High Speed Photography.	52
V	MICROSTRUCTURE	
	1. Introduction.	55
	2. DPTE Copper	58
	3. 6061-T6 Aluminum.	58
	4. 2024-T4 Aluminum.	60
	5. OFHC Copper	60
	6. Microstructure Resulting From Impact	63
VI	TWO-DIMENSIONAL MODELS	
	1. Introduction.	73
	2. Constitutive Relationships.	73
	3. Two-Dimensional Modeling.	75
VII	CONCLUSIONS	
	1. Introduction.	78
	2. Experimental Apparatus and Methodology	78

TABLE OF CONTENTS

Section	Title	Page
3.	Physical Process Resulting From Impact	79
4.	α/β Model	80
	REFERENCES.	83
	BIBLIOGRAPHY.	84
Appendix		
A	TEST PROCEDURES	85
B	DATA FILES.	91
C	TENSILE SPECIMEN.	99
D	LOAD VERSUS TIME CHARTS	103
E	HUGONIOT MODEL.	109
F	RAW DATA SHEETS	117

LIST OF FIGURES

Figure	Title	Page
1	Plastic and Elastic Wave Motion in the Specimen	5
2	Nomenclature Used in the Taylor Analysis.	7
3	Schematic Diagram Showing the Volume of Material that Passes into the Plastic Zone.	8
4	Stress Ratio Contours Used for Determining, From the Exact Analysis, the Yield Stress.	12
5	Profile Geometry Predicted by Hawkyard's Energy Balance Analysis	14
6	Mass Transfer From the Undeformed Section of the Specimen	15
7	A Taylor Anvil Test Apparatus	23
8	Firing Line Components.	24
9	Target Design and Photographic Configuration	25
10	Block Diagram of the Signal Flow for the Pressure Transducer Measurement System. .	28
11	Typical Wave Forms Generated by the Pressure Transducers.	28
12	Propellant Weight Versus Velocity Curve for Different Specimen Masses	33
13	Detail Drawing of the Measurement Gauge .	35
14	Nondimensionalized Parameters, l_f/L , and L_f/L as a Function of the Impact Velocity	38
15	Values of the Yield Stress Plotted as a Function of the Specimen Aspect Ratio . .	44

LIST OF FIGURES

Figure	Title	Page
16	Nondimensional Form of the Undeformed Final Length as a Function of the Nondimensional Final Length Parameter. . .	47
17a	Ballistic Geometry Data, in Nondimensional Form, for the Current Investigation. . . .	48
17b	Ballistic Geometry Data, in Nondimensional Form, for 2024-T4 Specimens.	49
18	Final Diameter as a Function of the Impact Velocity	51
19	Strain at the Target/Specimen Interface as a Function of Time.	52
20	Position of the Undeformed End of the Specimen as a Function of Time	53
21	Optical Micrograph Showing the Microstructure of DPTE Copper.	58
22	Optical Micrograph Showing the Microstructure of 6061-T6 Aluminum	59
23	Optical Micrograph Showing the Microstructure of 2024-T4 Aluminum	60
24	Optical Micrograph Showing the Microstructure of Half Hard OFHC Copper. .	61
25	TEM Micrograph of Half Hard OFHC Copper. .	62
26	Optical Micrograph Showing the Microstructure of Annealed OFHC Copper . .	62
27	Impact Specimens of OFHC Copper.	64
28	Optical Micrograph Showing the Microstructure of Annealed OFHC Copper After Impact	65
29	Optical Micrograph Showing the Microstructure of Half-Hard OFHC Copper After Impact	65

LIST OF FIGURES

Figure	Title	Page
30	TEM Micrograph Showing Deformation Twins in OFHC Copper	67
31	Photo-Micrograph of a TEM Replica Showing a Shock Formed Twin in Half-Hard OFHC Copper After Impact.	68
32	Optical Micrograph Showing the Microstructure of DPTE Copper After Impact	70
33	Optical Micrograph Showing the Microstructure of DPTE Copper, After Impact, Near the Free Boundary Surface	70
34	Optical Micrograph Showing the Microstructure of 6061-T6 Aluminum After Impact	71
35	Optical Micrograph Showing the Microstructure of 2024-T4 Aluminum After Impact	72
36	Stress/Strain Response of Pure Copper Under High Strain-Rate Conditions	31
C-1	Dimensions of the Tensile Specimen	101
D-1	Load Response of OFHC Copper	105
D-2	Load Response of DPTE Copper	106
D-3	Load Response of 6061-T6 Aluminum.	107
D-4	Load Response of 2024-T4 Aluminum.	108
E-1	Schematic Diagram Showing the Parameters Used in the Hugoniot Model	111

LIST OF TABLES

Table	Title	Page
1	MECHANICAL PROPERTIES (QUASI-STATIC)	20
2	SPECIMEN DIMENSIONS.	34
3	LINEAR REGRESSION AND STATISTICAL DATA . . .	39
4	COMPARISON OF STATIC AND DYNAMIC YIELD STRESS VALUES.	40
5	EXPERIMENTAL TEST DATA	42
6	COMPUTED YIELD STRENGTH VALUES	43
7	MATERIAL COMPOSITION	57

SECTION I

INTRODUCTION

DYNAMIC MATERIAL BEHAVIOR

The factors common to any static, or dynamic, stress analysis problem consist of the following: the specimen geometry, the loading applied at the boundary, and the material of the specimen. These three factors will interact to produce the stress level inside the body. The response of the body to these stresses is important in most engineering endeavors. Frequently, a rational engineering design requires the ability to predict the stresses and material response in each component.

The most common approach to investigating the response of a material is to fix two of the three factors governing the stress problem. As an example, in a uniaxial tensile test the specimen geometry and loading have been standardized. This provides a uniform basis to compare the third factor, the specimen material. This test is based upon a straightforward method of calculating the stress level in the specimen.

There are several limitations to this type of materials investigation. First, the response of the material to the complex loadings experienced in service may not be accurately represented by such a simple test. Second, for some applications the experimental apparatus cannot provide the necessary loading requirements seen in service, e.g., high strain rates.

To overcome these restrictions the designer can take either of the two following approaches: use a large factor of safety, or proceed on a need to know basis. The former, though widely used, will not be discussed. The second approach usually begins by redefining the experimental technique in terms of the specific problem at hand. This approach is used frequently for

investigating materials response to rapidly applied loads. If the loading rate and magnitude are sufficiently high, the material response is called dynamic.

Dynamic material behavior has been characterized by the presence of inertial effects and wave propagation which affect the stress distribution inside the specimen. If an impulsive load, large enough to cause permanent deformation, is applied to the boundary of a specimen, the stress in the region nearest the load will be significantly higher than in any other portion of the body. The deformation which occurs in the specimen can be modeled by its wave-like motion through the material. If the deformation takes place rapidly, the particle being displaced will have some inertial energy. If the inertial energy is large enough, it can have a significant effect on the final configuration of the specimen.

Certain aspects of dynamic behavior have been known since the 19th century. British investigators showed that an iron wire could resist permanent deformation under large loads for short periods of time. This test proved that a relationship existed between the yield stress in a material and the rate at which the load was applied.

In the 1940's, G.I. Taylor, Reference 1, met with some success at characterizing this behavior. He proposed an experiment to measure what was then called the dynamic yield strength.

The experiment proposed by Taylor has become a standard test in laboratories that study the behavior of materials at high rates of deformation. The Taylor test consists of impacting a plane-ended cylindrical projectile against a relatively rigid, massive anvil. What should come out of the Taylor test is the

yield stress level for a material that is rapidly, or impulsively, loaded. The Taylor test was designed to standardize the specimen geometry and the loading pattern applied to the specimen boundary. As previously mentioned, the last component of the internal stress problem would be the material under investigation.

One use for the information generated by the Taylor test is in the development of armor and armor penetrators. Models of the interaction between a target and a penetrator, References 2 and 3, require that the materials be characterized by their dynamic strength values. Another use for the Taylor test is as an accuracy check of two-dimensional computer models of deformation behavior, References 4 and 5.

The object of this report is fourfold. First, it is to examine aspects of both two-dimensional and one-dimensional modeling used with Taylor testing. Second, it is to describe in detail a recently constructed Taylor test apparatus. Third, it is to provide an analysis of data obtained experimentally and used in the one-dimensional models. Fourth, it is to report on observations made on the microstructure found in test specimens.

SECTION II

ONE-DIMENSIONAL MODELS

1. BACKGROUND

One-dimensional models of the Taylor experiment are used to calculate the yield stress level of a material from post-test measurements of specimen deformation. Historically, all one-dimensional models are based on the analysis developed by Taylor, Reference 1. Over the years various investigators have proposed modifications to his analysis by changing the basic equations or using different types of material constitutive relationships. Therefore, the discussion of one-dimensional models should begin with a development of Taylor's original analysis of the problem.

At impact, a wave of compressive stress will be generated at the anvil face. If the velocity of the projectile is sufficiently high, the stress wave will separate into two components. The first, or leading, component is an elastic compressive wave, moving through the material at the speed of sound. The amplitude of the stress level behind the compressive wave front is below the yield strength of the material. The second component, a plastic compressive wave, will follow the elastic compressive wave at a greatly reduced velocity. At the plastic front the stress level exceeds the yield strength of the material. The high compressive stress causes severe deformation to occur in the form of radial motion outward away from the specimen axis, accompanied by axial shortening of the specimen.

As the event proceeds, the elastic compressive wave will arrive at the free-end of the specimen, where it is reflected as a tensile wave of equal magnitude. The tensile wave will move through the specimen until it encounters the plastic compressive wave front, located within the specimen, Figure 1, Reference 6. The motion of the elastic wave and the interaction with the

plastic compressive wave will have two important effects. First, the velocity of the plastically undeformed portion of the rod will be reduced as the elastic wave moves through the material. Second, the reflected tensile wave will superimpose with the compressive plastic wave to reduce the overall stress at the plastic wave front. After repeated occurrences, the motion of and stress within the specimen will both be reduced to zero.

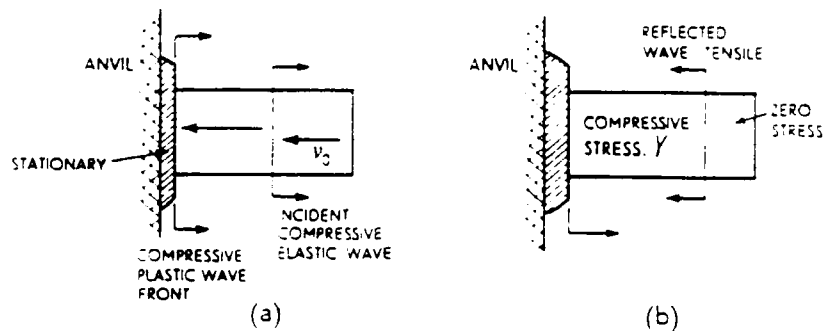


Figure 1. Plastic and Elastic Wave Motion in the Specimen

2. TAYLOR'S ANALYSIS

To construct a model of the impact event, Taylor makes three assumptions in his analysis: the material stress-strain relationship is rigid, plastic; radial inertia effects can be neglected; and, a condition of uniaxial stress exists across the elastic/plastic interface. The relative effects of these assumptions have stirred numerous debates and papers regarding the validity of his analysis. The simplicity of the experimental technique and subsequent reduction of data are incentives to accept these assumptions. It must, however, be kept in mind by the user of such data the level of approximation that was used in the construction of the analysis.

Taylor's analysis relates the altered geometry of the specimen after impact to the dynamic yield strength of the material. In this way, Taylor could extract the crucial dynamic

strength from only two postmortem measurements of the deformed specimen. Taylor formulates his analysis through equations that relate various kinematic parameters during the impact event, such as the time required for an elastic wave to travel down the rigid portion of the specimen and back to the plastic wave front, the incremental change in the position of the plastic wave front, the foreshortening of the rigid portion of the rod, and the incremental change in the velocity of the undeformed portion of the rod. By eliminating the speed of sound in the material, he generates a set of differential equations. These differential equations define the velocity of the plastic wave, the rate of foreshortening of the undeformed portion of the rod and its deceleration.

To begin the development of the analysis by Taylor, it is first necessary to define the nomenclature to be used, Figure 2. Let L represent the original length of the specimen, and S , the time dependent displacement of the undeformed portion of the rod relative to the initial configuration. At some time after impact, X represents the extent of the plastic zone relative to the original configuration. The position of the plastic front is h , measured relative to the anvil face. The current length of the undeformed portion is given by l . A relationship exists between the time dependent quantities, S , l , h , and the original length

$$L = S + l + h \quad (1)$$

Differentiating Equation (1) with respect to time gives

$$0 = \dot{S} + \dot{l} + \dot{h} \quad (2)$$

or

$$\dot{h} = -(\dot{S} + \dot{l}) \quad (3)$$

But \dot{S} is simply the velocity, v , of the back end of the specimen, and, \dot{h} is renamed, λ , the Eulerian plastic wave speed, to give

$$\lambda = -(v + \dot{l}) \quad (4)$$

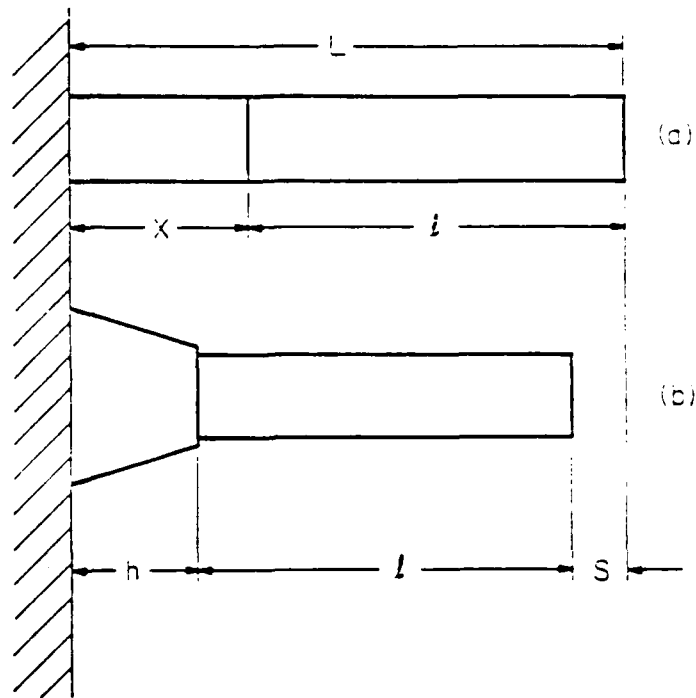


Figure 2. Nomenclature Used in the Taylor Analysis

The term, \dot{l} , describes the rate of foreshortening of the undeformed section of the rod and can be written

$$\dot{l} = -(\dot{v} + \dot{\lambda}) \quad (5)$$

By applying Newton's second law to the undeformed portion of the rod the equation of motion can be written as

$$\frac{dv}{dt} = -\frac{Y}{(\rho l)} \quad (6)$$

Where Y and ρ are, respectively, the material yield stress and mass density.

Taylor continues the analysis by writing equations describing conservation of mass and momentum across the plastic wave front. A differential slice of the undeformed portion of the rod, dx ,

Figure 3, with cross sectional area A_0 , crosses the plastic front and is now contained in the volume described by the new area, A , and the differential thickness, dh . The elemental length, dX , can be written in terms of the undeformed section using the relationship, $dX = -d\ell$, Figure 2(a). The equation for the conservation of mass can be written as

$$\rho A dh = \rho A_0 dX \quad (7)$$

Dividing both sides by ρdt , Equation (7) becomes

$$\frac{A dh}{dt} = A_0 \frac{dX}{dt} \quad (8)$$

After substituting for dX in terms of $d\ell$, Equation (8) can be rewritten as

$$A \lambda = - A_0 (\dot{\ell}) \quad (9)$$

Substituting from Equation (5) gives

$$A \lambda = A_0 (v + \lambda) \quad (10)$$

Taylor assumes the material behaves in such a way that when it crosses the plastic front it comes to rest instantaneously. This assumption imposes a condition on the model that describes the intermediate states of the event as having a strain discontinuity at the elastic/plastic interface, Figures 1 through 3. This strain discontinuity is created by the

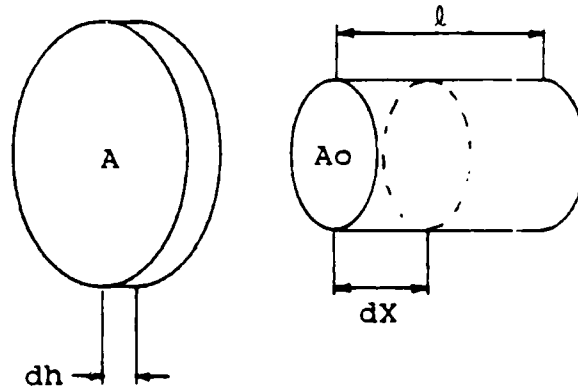


Figure 3. Schematic Diagram Showing the Volume of Material That Passes into the Plastic Zone

instantaneous change in cross sectional area of the material passing through the plastic front.

The linear momentum equation is written

$$\rho A v dl = Y(A - A_0) dt \quad (11)$$

The left hand side of the equation is the change of momentum of the differential element, dl , having an initial velocity, v , and a final velocity of zero. The right hand side is the impulse term, where the force is calculated from the stress in the body, assumed uniform over the cross section, times the relative change in area.

To construct an analysis based on the postmortem measurements of the yield boundary, Taylor must describe the motion of the elastic/plastic interface. By combining Equations (6), (10), and (11), Taylor showed that the plastic front moves approximately linearly with time. Having determined this from the analysis, he subsequently imposes this as a constraint on the model when developing the expression for the yield stress.

The expression Taylor uses for computing the yield stress is generated from the equation of motion of the undeformed portion of the rod, Equation (6). The independent variable, however, has been changed from that of time to the incremental change in the length of the undeformed section of the rod. This gives

$$\frac{dv}{dt} = \frac{dv}{dl} \frac{dl}{dt} = - \frac{Y}{(\rho l)} \quad (12)$$

Equation (5) can be substituted into Equation (12) to give

$$\frac{dv}{dl} = \frac{Y}{\rho l (v + \lambda)} \quad (13)$$

After separating the variables, integrating and substituting the appropriate initial and final conditions, the equation becomes

$$\frac{Y}{\rho} \ln \left[\frac{L_f}{L} \right] = - \frac{1}{2} v^2 - v\lambda \quad (14)$$

where L_f is the final length of the specimen.

To eliminate the constant plastic wave speed, λ , Taylor assumes that the rear end deceleration of the rod is also constant. This assumption allows the duration of the impact event, T , to be calculated two ways. First, from the assumption of constant plastic wave speed

$$T = \frac{(L_f - l_f)}{\lambda} \quad (15)$$

Here the term, l_f , is the final length of the undeformed segment of the specimen. Then from the assumption of constant deceleration

$$T = \frac{2(L - L_f)}{V} \quad (16)$$

Eliminating T between Equations (15) and (16) the plastic wave speed is determined in terms of the impact velocity and the final specimen geometry

$$\frac{\lambda}{V} = \frac{(L_f - l_f)}{2(L - L_f)} \quad (17)$$

Using Equation (17) to eliminate the plastic wave speed in Equation (14), the yield stress is determined as a function of density, impact velocity, original length, final undeformed length, and the final total length. This gives the following expression for the yield stress:

$$Y = \frac{\rho V^2 (L - L_f)}{2 (L - L_f)} \frac{1}{\ln\left[\frac{L}{L_f}\right]} \quad (18)$$

3. IMPROVED ANALYSIS BY TAYLOR

In a second approach, Taylor concedes that the rear end deceleration is not constant. He suggests a more exact measure of the flow stress can be made by applying a correction factor to the values determined in the above simplified analysis. This correction factor is calculated from the error introduced by assuming that the rear end deceleration was uniform.

To determine the correction factor, Taylor establishes a set of equations relating the plastic wave speed and the rear end motion to the length of time for the deformation to occur. This set of expressions can be solved when l_f/L and L_f/L are known quantities. To simplify the process, a graph was constructed with l_f/L as the ordinate and L_f/L as the abscissa, Figure 4, Reference 1. The appropriate correction factor, Y/Y_1 , can be quickly determined from the coordinate position on the graph. The term Y_1 describes the yield stress calculated by Equation (18). In general, the more exact analysis will increase the yield stress level of the material.

Taylor's analysis predicts that the cross sectional area of the deformed region will vary in a uniform manner. At the elastic/plastic interface, where the state of stress exceeds the yield strength of the material, the material will deform radially an amount which is dependent on the current velocity of the undeformed segment of the specimen. Taylor imposes the condition that the deceleration of the rear end be uniform; therefore, the cross sectional area in the deformed region must be changing uniformly. In reality, the specimen profile in some materials will be noticeably nonuniform and will depend greatly on the strength of the material and the velocity of the impact. Such discrepancies between predicted deformation geometry and actual observation is related to the assumptions regarding the material's stress-strain relationship and to the effect of radial inertia. A rigid, plastic material behavior model neglects the effects of complex material behavior at high strain rates. A more comprehensive constitutive model might contain terms to predict such phenomena as strain hardening, thermal softening, strain rate effects, dislocation motion, grain size effects, and possibly the effects due to the formation of deformation twins.

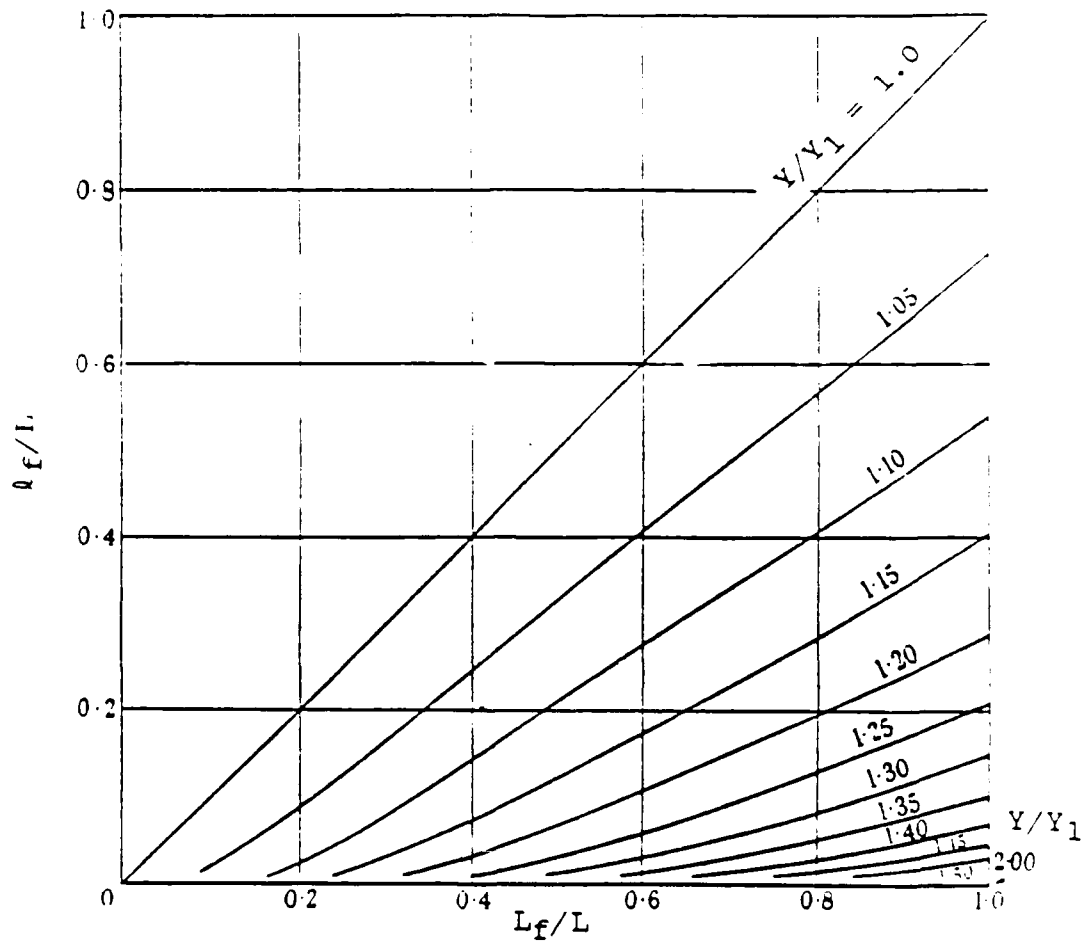


Figure 4. Stress Ratio Contours Used for Determining, from the Exact Analysis, the Yield Stress

4. HAWKYARD'S ANALYSIS

Hawkyard, Reference 7, modified Taylor's analysis of the problem by employing an energy balance expression for a differential element crossing into the plastic zone. The work comes from slowing the elemental slice of the specimen from its current velocity v to zero. Additional work is supplied by the force acting on the elemental piece by the undeformed section. These two terms combine to form the following expression for the energy:

$$\text{Energy} = -A_0 \frac{\dot{l} \rho v^2}{2} + Y A_0 (-\dot{l} - \lambda) \quad (19)$$

Equation (4) can be used to make substitutions in both terms to give

$$\text{Energy} = A_0 \frac{(v + \lambda) \rho v^2}{2} + Y A_0 (v) \quad (20)$$

Hawkyard equates this expression to the rate of doing plastic work in uniaxial compression on an element.

$$A_0 (v + \lambda) Y \ln \left[\frac{A}{A_0} \right] = A_0 \frac{(v + \lambda) \rho v^2}{2} + Y A_0 (v) \quad (21)$$

Using mass conservation across the plastic front and force equilibrium of the rigid segment, an expression can be developed that predicts the profile geometry. Hawkyard's analysis has achieved a certain measure of success in predicting a concave profile, which has been observed in experiments, Figure 5, Reference 7.

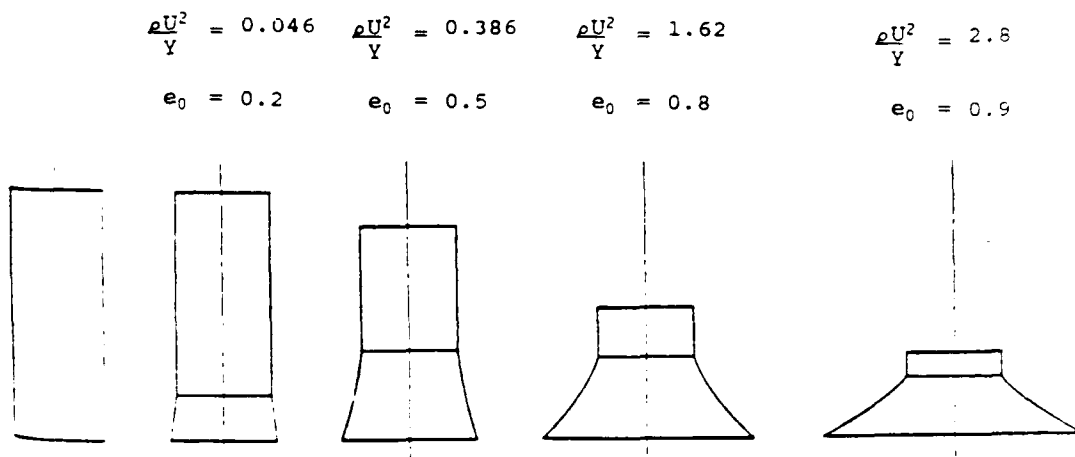


Figure 5. Profile Geometry Predicted By
Hawkyard's Energy Balance Analysis

5. α/β ANALYSIS

Critiques of the analysis by Taylor suggest that the momentum equation across the elastic plastic interface was not an accurate application of the conservation of momentum. Jones, Gillis, and Foster, Reference 8, report that a more precise expression for the linear impulse/momentum equation should contain a term accounting for the mass loss in the undeformed portion of the rod, Figure 6, Reference 8. At some time, t , after impact the undeformed length can be given by

$$l = L - X \quad (22)$$

At a small increment of time later, $t + \Delta t$, the undeformed segment has shortened by an amount equal to ΔX . If the physical system is defined to be the initially undeformed portion of the rod, the impulse equation gives

$$\begin{aligned} \rho A_0 \Delta X u + \rho A_0 (L - X - \Delta X) (v + \Delta v) - \rho A_0 (L - X) v \\ = \frac{(2P + \Delta P) \Delta t}{2} \end{aligned} \quad (23)$$

The first term on the left side is the momentum of the differential element, ΔX , at a velocity u , as it passes into the plastic zone. The second term accounts for the momentum of the undeformed segment, which has undergone a mass transfer, and has a new velocity $v + \Delta v$. The mass, transferred from the undeformed segment, is defined in terms of the original cross sectional area, A_0 , and the differential change in the extent of the plastic zone, ΔX , relative to the original configuration.

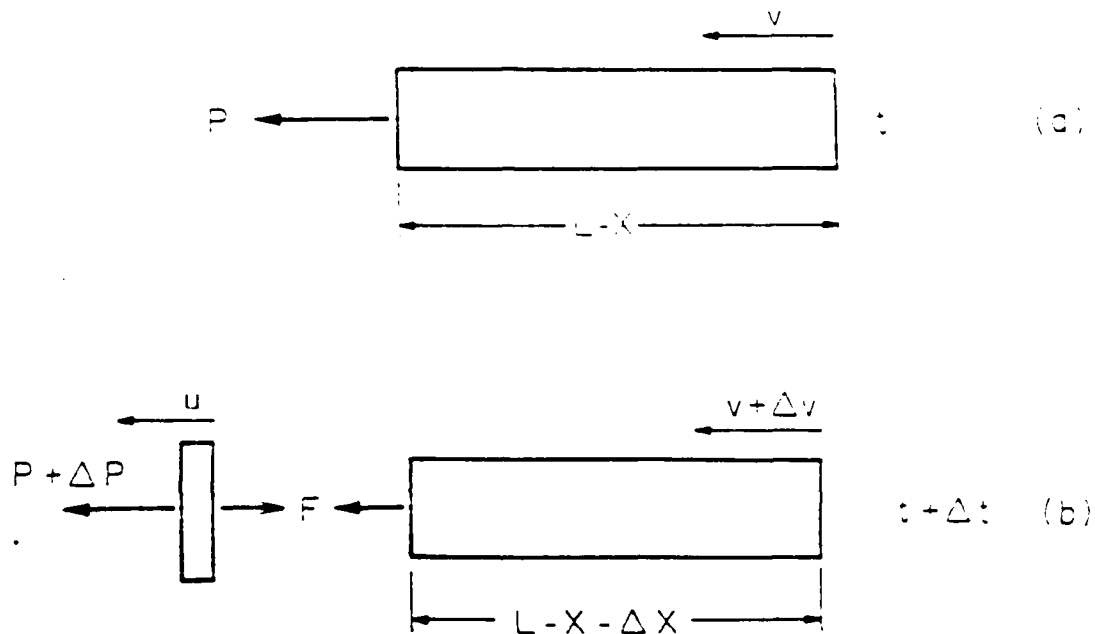


Figure 6. Mass Transfer From the Undeformed Section of the Specimen

The last term on the left is the original momentum of the system. The right hand side of the equation is the impulse applied during the time increment.

A new form of the equation of motion of the undeformed segment of the rod results from Equation (23). After dividing both sides by Δt , taking limits, and making appropriate substitutions Equation (23) becomes

$$l\dot{v} + \dot{l}(v - u) = \frac{P}{\rho A_0} \quad (24)$$

The force, P, can be replaced by

$$P = \sigma A = \frac{\sigma A_0}{(1 - e)} \quad (25)$$

Here σ is the engineering stress; and e is the longitudinal compressive strain. Now

$$\rho \dot{v} + \rho(v - u) = \frac{\sigma}{(1 + e)} \quad (26)$$

describes the motion of the rigid portion of the specimen.

If there is no change in particle velocity across the interface, $v=u$, and the longitudinal compressive strain, e , is set equal to zero, then Equation (26) reduces to Equation (6) used in Taylor's analysis. From the conservation of mass, Equation (10), it is evident that Taylor intended the model to describe the elastic/plastic front as a strain discontinuity. This led Jones et al, Reference 8, to criticize the methods used by previous investigators. It is the velocity discontinuity, $v \neq u$, across the interface that causes the deformation.

Jones et al developed the analysis by assuming, as Taylor did, that the material crossing from the rigid portion of the rod into the plastic zone is brought instantaneously to rest, $u=0$. The equation of motion can then be written as

$$\frac{d(\rho v)}{dt} = \frac{\sigma}{(1 + e)} \quad (27)$$

Using a Lagrangian coordinate system, the strain at the plastic front can be described by a relationship among the kinematic variables.

$$e \dot{l} = (v - u) \quad (28)$$

Using the assumption that the material in the plastic zone has zero velocity, $u=0$, the strain can be described in terms of the rear end velocity divided by the rate of foreshortening of the rigid portion of the rod. If the plastic wave speed is assumed constant, the rate of foreshortening can be described by

Equation (5). The strain can now be described by the rear end velocity and the plastic wave speed. Substituting for the strain in the equation of motion gives

$$\frac{d(lv)}{dt} = \frac{\sigma(v + \lambda)}{\rho\lambda} \quad (29)$$

Using the chain rule, Equation (29) can be written making dl the independent variable

$$\frac{d(lv)}{dt} = \frac{d(lv)}{dl} \frac{dl}{dt} = \frac{\sigma(v + \lambda)}{\rho\lambda} \quad (30)$$

Which can be further manipulated after substituting from Equation (5) to give

$$\frac{d(lv)}{dl} = \frac{-\sigma}{\rho\lambda} \quad (31)$$

Following the use of the product rule, Equation (31) can be written as

$$l \frac{dv}{dl} + v = \frac{-\sigma}{\rho\lambda} \quad (32)$$

The variables can now be separated, and the resulting expression integrated, to give an explicit expression for l in terms of the velocity, v .

$$\ln\left(\frac{L}{l}\right) = - \int_V^v \frac{dv}{\frac{-\sigma}{\rho\lambda} - v} \quad (33)$$

Before the right hand side of Equation (33) can be integrated a constitutive relationship must be invoked to specify σ . Using the perfectly plastic material model gives

$$\sigma = -Y \quad (34)$$

Jones et al, make the assumption that the dynamic yield stress is approximately a constant for any given impact velocity. After substituting Equation (34) into Equation (33), the undeformed length is given as a function of the impact velocity, the density, the yield strength, and the plastic wave speed,

$$\ln\left(\frac{L}{l}\right) = - \int_V^v \frac{dv}{\frac{c^2}{\lambda} - v} \quad (35)$$

where

$$c^2 = \frac{Y}{\rho}$$

Evaluating Equation (35) gives

$$\frac{L}{l} = \frac{\frac{c^2}{\lambda} - v}{\frac{c^2}{\lambda}} \quad (36)$$

After substituting the appropriate final conditions, Equation (36) can be manipulated into the form

$$\frac{L}{l_f} = 1 - \left(\frac{\lambda}{V}\right) \left[\frac{\rho V^2}{Y}\right] = 1 - \alpha\beta \quad (37)$$

where

$$\alpha = \frac{\rho V^2}{Y}$$

$$\beta = \frac{\lambda}{V}$$

The parameters, α and β , are the nondimensional forms of the yield strength and the plastic wave speed, respectively.

Equation (37) contains the unknowns, λ and Y , and, therefore, a second independent equation is required.

The second equation can be generated from the equation of motion used in the form given by Equation (29). After using the product rule, Equation (29) can be rewritten as

$$l \frac{dv}{dt} + v \frac{dl}{dt} = \frac{\sigma(v + \lambda)}{\rho \lambda} \quad (38)$$

Substituting from Equations (5) and (34) into Equation (38), then separating the variables gives

$$t_f = \int_0^V \frac{l dv}{\frac{Y(v + \lambda)}{\rho \lambda} + v(v + \lambda)} \quad (39)$$

Where the limits have been chosen to reflect the final conditions, $v=0$, and $t=t_f$. The velocity dependent term, l , can be expressed by Equation (36) and substituted into Equation (39) to give

$$L \left[\frac{Y}{\rho \lambda} - V \right] = \int_0^V \frac{dv}{(v + \lambda) \left[\frac{Y}{\rho \lambda} + v \right]^2} \quad (40)$$

After evaluating the integral, making appropriate substitutions, and performing some algebraic manipulation, Equation (40) gives

$$\frac{L_f - l_f}{L} = \left[\frac{\beta(1 - l_f/L)^2}{(1 + \beta(1 - l_f/L))} \right] - \left[\frac{\beta(l_f/L)(1 - l_f/L)}{(1 + \beta(1 - l_f/L))} \right] \ln \left[\frac{\beta(l_f/L)}{1 + \beta} \right] \quad (41)$$

Using suitable experimental data, Equation (41) can be solved numerically for the parameter β . By substituting the value of β into Equation (37) the parameter α is determined. Knowing α and β , the material flow stress, Y , and the Eulerian plastic wave speed, λ , are easily found.

6. EXPERIMENTAL MATRIX

An experimental matrix was constructed to test the model proposed by investigators Jones, Gillis, and Foster, Reference 8. This matrix consisted of several types of materials. The specimen geometries used in this investigation covered a wide range of aspect ratios (length/diameter). The influence of

specimen geometry is a factor that has been debated in the literature by several investigators, References 9 and 10.

The materials chosen consisted of two types of aluminum and copper. The aluminum materials were alloys 2024-T4 and 6061-T6. The copper materials were Oxygen Free High Conductivity (OFHC) copper and a Phosphorous Deoxidized Tellurium copper alloy (DPTE); both coppers were received in a half-hard condition. The materials were chosen with regard to the sensitivity of the yield stress to the rate of straining. The 6061-T6 material is known to be relatively insensitive to rate effects, whereas the 2024-T4 and the OFHC copper are known to be rate-sensitive materials. The DPTE copper is a solution strengthened copper/tellurium alloy, chosen for comparative purposes with the higher purity copper.

Mechanical properties of the test materials were determined from tensile tests and hardness measurements. A typical load versus time chart produced from a tensile test of each material can be found in Appendix D. Results of these test and hardness measurements are reported in Table 1.

TABLE 1. MECHANICAL PROPERTIES (QUASI-STATIC)

MATERIAL	YIELD STRENGTH MPa	TENSILE STRENGTH MPa	PERCENT ELONGATION	HARDNESS Rb
OFHC COPPER	—	350	17.6	33.5
DPTE COOPER	—	300	12.2	32.0
2024-T4	400	500	23.0	75.5
6061-T6	315	340	18.1	45.7

SECTION III

EXPERIMENTAL APPARATUS

1. BACKGROUND

In order to conduct the proposed test matrix, a suitable experimental apparatus was required. Several factors determined by experience with a compressed air gun made it imperative that a new apparatus be constructed. The baseline operational requirements called for a flexible, repeatable, and efficient system design. The perspective from which the new apparatus was developed can be better understood following a brief summary of the configuration and capabilities of the compressed air gun system.

The gas gun system was simply a high pressure tank, or vessel, attached to the breech end of a gun barrel. The muzzle end of the gun barrel was permanently fixed against the side of a holding tank. The target was positioned in the holding tank at a standoff distance of approximately 38 cm from the muzzle.

The operation of the gas gun required several steps. First, a thin metal diaphragm (bursting disk) was placed over the discharge orifice of the pressure tank. Next, a specimen was loaded into the gun barrel, after which the barrel and the pressure vessel were bolted together, sealing the pressure tank orifice. At this point, the vessel could be pressurized to the desired level. Once the prescribed pressure level was established, the diaphragm was punctured, via a mechanical striker, allowing the pressurized gas to escape and accelerate the specimen through the barrel.

A number of deficiencies were experienced with the use of such an apparatus. At best, the gas gun system efficiency was quite poor. After each shot, it was necessary to unbolt the pressure tank from the barrel. In addition, it took several

minutes to build up the operating pressure needed for the test. In terms of operational capability, the system had very poor repeatability.

The lack of repeatability was caused by two main problems: the bursting disk often ruptured prematurely and variations in the machining of the specimen allowed gas to escape past the specimen. For shots made at equal tank pressure, the impact velocities would vary widely if leakage occurred.

The apparatus had built-in limitations with regard to flexibility. The pressure vessel had, for safety reasons, an upper limit of 5.17 MPa. Hence, the total available energy was fixed. For high density materials, this energy level was not sufficient for experiments in the desired velocity range. Often, the lack of adequate energy was manifested by oblique impact with the target. Since the muzzle and target positions were fixed, the standoff distance could not be adjusted. For these reasons, a new apparatus, Figure 7, was developed based on the use of a smokeless gun powder as a propellant.

2. DESCRIPTION OF THE EXPERIMENTAL APPARATUS

The launch tube was machined from 4340 steel and was center bored to an inside diameter of 7.620 mm. Two ports were drilled into the gun barrel near the muzzle. The ports were 2.54 cm apart and were tapped to receive pressure transducers. Monitoring the electrical signals of the transducers was one method of determining the projectile velocity near the muzzle of the launch tube.

The breech end of the launch tube was chambered to accept a 0.308 caliber cartridge case. The bullet and original powder charge were removed from a 0.308 rifle cartridge so that the primed cartridge case could be used. In place of the original powder charge, a specific quantity of smokeless powder (Red Dot)

To prevent the expanding powder gas from leaking past the specimen, a plastic obturator was used to form a seal. The obturator was positioned between the cartridge and the specimen, Figure 8. The end of the obturator nearest the cartridge was hollowed to facilitate radial expansion of the remaining material under pressure. Thus, the expanding gas deforms the obturator to form a seal against the gun bore wall. In this manner, the energy of the propellant was used entirely for accelerating the specimen.

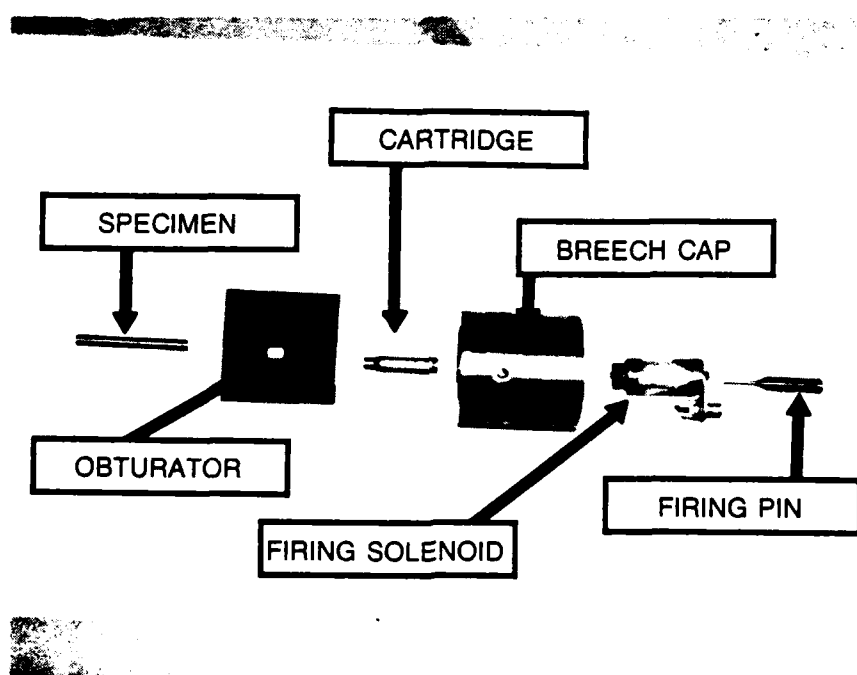


Figure 8. Firing Line Components

The launch tube was fixed in position by a set of v-block mounts. This construction allowed rapid change of the standoff distance between the muzzle and the target. Typically, the standoff was in the range of 7 to 20 cm.

The target was a 23-cm diameter, by 20 cm in length, cylinder of hardened 4340 steel. Both ends were machined parallel and lap finished. The design of the target and target rest, Figure 9,

optimized the available surface area for impact tests. After each test, the target could be rotated to provide a new surface for impact. If no permanent deformation occurred in the target surface, several tests were conducted using the same area of the anvil. After completing one revolution of the target, the center line of the cylindrical anvil could be lowered with respect to the projectile flight line to provide a new surface area for impact. To lower the target, a layer of the polypropolux base material was removed from under the target rest. This process of lowering the anvil center line could be continued until the entire surface area was used. Subsequently, the parallel faces of the anvil could be reversed and the process repeated prior to remachining. This optimized the available area on the target and reduced the down time required for remachining and polishing of the surface.

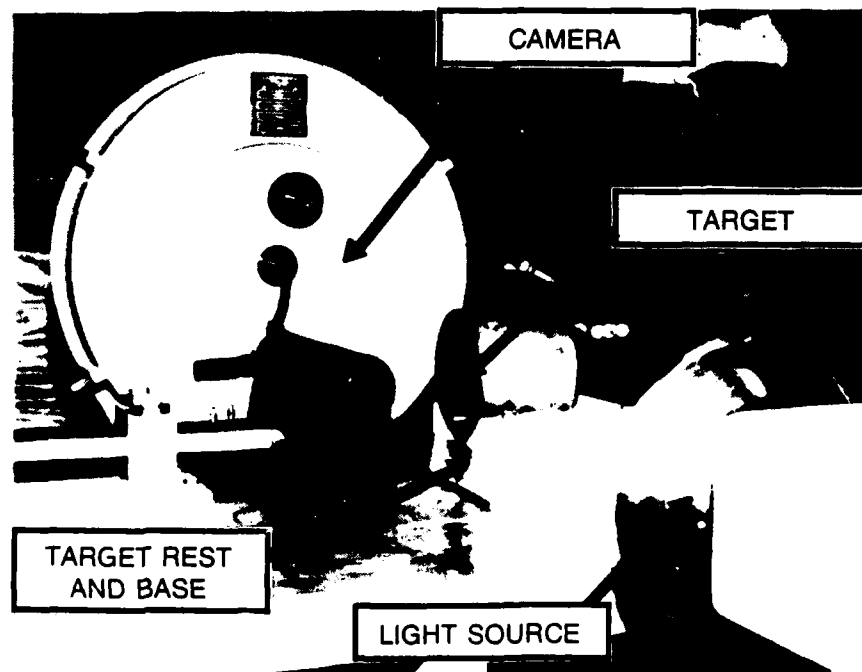


Figure 9. Target Design and Photographic Configuration

The target and the muzzle of the launcher were covered by an aluminum housing. Two slots were cut into the housing parallel

to the flight line of the projectile. These slots were covered with 6.35 mm thick plexiglass, providing windows which allowed the incoming projectile and its subsequent deformation to be photographed. The housing prevented the rebounding projectile from causing undesirable damage. The inside of the housing was lined to prevent secondary deformation from occurring on the specimen. However, a large number of specimens were slightly deformed on the rear end of the projectile because of impact with the muzzle face of the barrel after rebounding from the target.

3. VELOCITY MEASUREMENT TECHNIQUES

During the test, as many as three techniques were used to determine the projectile velocity. As previously mentioned, the gun barrel was instrumented with two piezoelectric pressure transducers. The outputs from the transducer amplifiers were fed into a dual trace oscilloscope. From the oscilloscope, the time required for the expanding gas of the propellant to pass between the two transducers could be measured. Knowing the time, and the distance between the transducer ports, the velocity was easily calculated.

A learning period was necessary to determine what threshold sensitivity level to set on the transducer amplifiers for the various pressure levels seen in the barrel. If the amplifiers were set too sensitively, the signal would be erratic, possibly from the elastic wave in the gun itself. If the sensitivity was set too low, no response would be obtained. In both cases, the necessary sensitivity level was always pressure dependent. Eventually, the amount of propellant became the best source of a priori information on how to set the sensitivity level.

Error in the velocity found by using the pressure transducers can be analyzed by examining the source for the data. The signals from the pressure transducers, located near

the muzzle end of the launch tube, are sent through a signal amplifier before being displayed on a digital oscilloscope, Figure 10. The signals displayed on the oscilloscope can be measured with the sweep cursor to determine a time interval necessary for calculating the muzzle velocity, Figure 11(a). It was considered for this analysis that uncertainties, or systematic errors, in the measurement system, i.e., line noise, transducer and electronic circuit response characteristics, etc., were small by comparison to the error introduced by misidentifying the starting and ending points of the interval to be measured.

The Nicolet oscilloscope displays a digitized form of the signal as a series of individual points. Each point represents a segment of time, which for this study was $1 \mu\text{s}$. The total time displayed could vary depending on the necessary resolution. A desirable wave form would show a smooth baseline, before the obturator passes the transducer port, followed by a sharp point, the response of the transducer to the propellant gas pressure, Figure 11(a). A poor signal would have a slowly changing response, or curved wave form, prior to a rapid deflection, Figure 11(b).

The former type of signal would provide the necessary information to determine the time interval to within $2 \mu\text{s}$. The accuracy from a measurement of a projectile having a velocity of 200 m/s , using this type of wave form would be $\pm 3 \text{ m/s}$. The second type of wave form would have greater uncertainty because of the subjectivity of establishing a suitable baseline and break point for the signal.

The second signal from the amplifier was sent to a multitrack recorder. The transducer signals were played back to provide an additional method of digitizing the data. A strip chart output of the recorded signals and a reference timing signal was produced. These data were digitized by establishing a timing base-

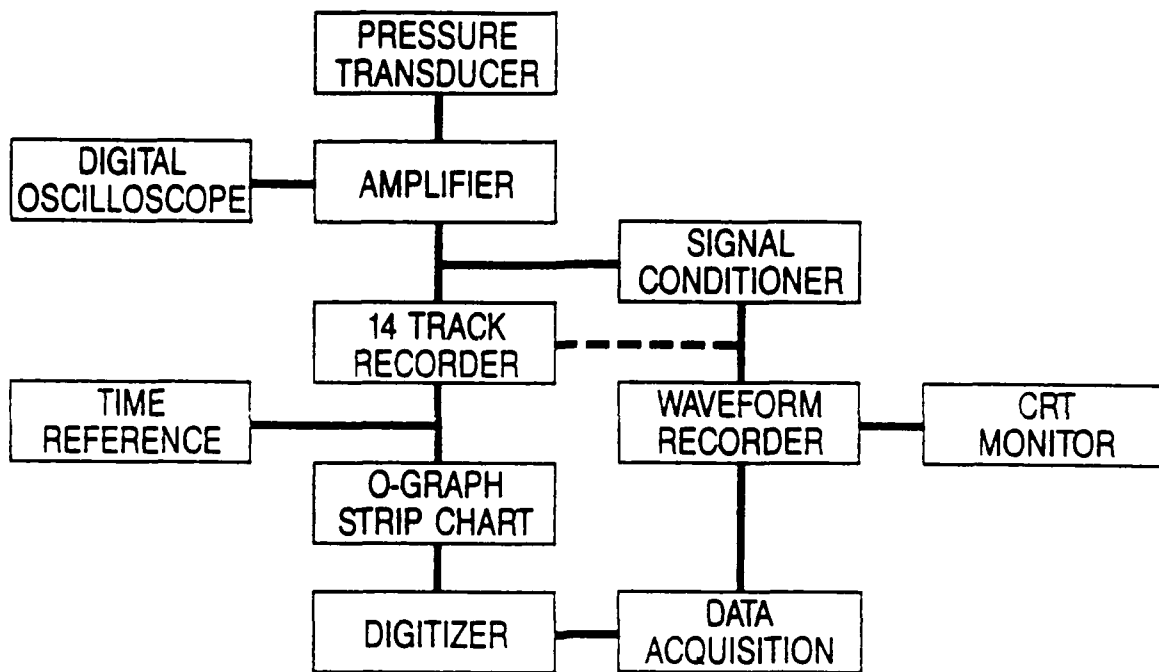


Figure 10. Block Diagram of the Signal Flow for the Pressure Transducer Measurement System

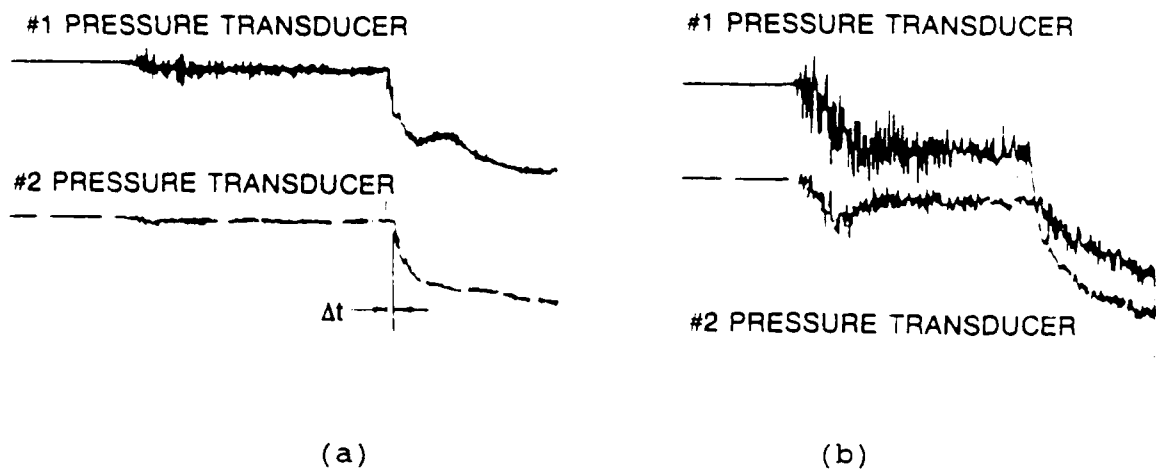


Figure 11. Typical Wave Forms Generated by the Pressure Transducers

line from the reference signal ($100 \text{ kHz} \pm 1 \text{ Hz}$). The starting and ending points were identified and the interval of time could be established. Similar to the digital oscilloscope, the choice of starting and ending points on the interval was subjective. The quantitative amount of error possible was dependent on the signal wave form. In general, measurements taken directly from the digital oscilloscope were considered to be the more accurate of the two methods, primarily because of the higher level of resolution of the wave form.

As a second measure of the projectile velocity, a high speed movie camera was also used. The 16 mm camera was capable of 10,000 frames per second. Using a $1/4$ frame format, a frame rate of 40,000/s could be obtained. A shadowgraphic technique was used to photograph the incoming projectile and its deformation at the anvil face. To do so required a light source located behind the specimen, as shown in Figure 9.

A fiducial marker (cylindrical magnet), of known diameter and length, was placed on the anvil face directly above the point of impact. With this in the field of view of the camera, it was possible to determine the degree of obliquity the camera had with the anvil face. By through-the-lens alignment, the camera was set as near parallel as possible to the anvil face. As a check, the profile image of the fiducial recorded on the film could be measured to determine if the length, viewed from the position of the camera, has been either elongated or shortened. The actual position of the anvil face, at the flight line, could then be located.

To determine a velocity from the film, it was necessary to find the time for the particular distance traversed. The time was calculated by multiplying the number of frames by the frame rate. An average value of the frame rate was determined by timing marks recorded on the film. The distance traveled could be measured using a film analyzer. A reference point at a

particular frame was established by positioning the vertical cross hair on the leading edge of the specimen, then setting the digital counter to zero. By moving the cross hair to the same location on the specimen at a different frame, a distance traversed could be measured. A scaling factor, for the magnification, was determined by measuring the specimen diameter in digital counter units. Multiplying the scaling factor with the counter distance measured for the traverse distance gives the actual distance.

Limits on the accuracy of such a technique were from two sources. First, the frame rate had to be averaged over a significantly larger portion of film than was used in the velocity measurement. Secondly, the location of the cross hair on the leading edge of the specimen was subjective. The motion of the specimen during the actual exposure caused the image to be slightly blurred. However, the overall technique was estimated to be accurate to within ± 10 m/s over the range of velocities used in this study.

On some of the test shots, the movie camera was replaced with a high speed framing camera to produce a detailed shadowgraphic recording of the impact event. This high speed Cordon camera was operated at 0.30 million frames per second. At this framing rate the resolution of the data generated was one photograph every $3.3 \mu\text{s}$. By comparison, the movie camera produced one photograph every $25 \mu\text{s}$.

Unfortunately, the complex design of the framing camera allowed only 82 frames, 35 mm size, to be recorded. This created a timing window, $160 \mu\text{s}$, in which several events had to occur. In this particular camera design, when it came up to the desired operating speed the shutter was automatically triggered. This created the situation where the light source controlled the film exposure level. By its very nature, the lighting found in high speed photography requires extremely specialized equipment. For

this camera, it was necessary to produce a large quantity of light energy for a very precise period of time. Too little light would produce poor film quality, while a lengthy exposure caused overwriting or a double image.

The timing window also required that the light source be synchronized with the projectile's arrival at the target face. This synchronization was accomplished by using the pressure transducers, located at the muzzle of the launch tube, with an appropriate delay circuit.

A third measurement system for the velocity relied on infrared beams and detectors between the anvil and the muzzle to record the position of the incoming projectile. The hardware used for this system can be seen in Figure 7, near the anvil face. The concept of the system was to use the beam emitters to produce a high voltage state in the detector circuit. Once the projectile passed into the beam, the detector would drop to a low voltage state. Monitoring the voltage states of the two detectors with an oscilloscope provided a time increment for the projectile to pass between the beams. Knowing the distance between the beams, the velocity was determined.

In this system the limitations were related to the response time characteristics of the circuitry. To reduce the error, the components used were individually compared with their counterpart to ensure both detector systems responded at equal rates. In general, the velocities measured by the infrared detectors were considered the most accurate of the three methods. All of the methods usually gave values within 5 percent of each other for the range of velocities used.

4. TEST PROCEDURES

The basic procedures for conducting the experiment can be broken into three groups: operations prior to firing the gun,

the actual test, and recovery and postmortem measurements. A step by step listing can be found in Appendix A.

The initial operation consisted of weighing and measuring the diameter and length of the specimen. Knowing the mass of the specimen and the velocity of interest, a propellant charge could then be specified. Initially, the process of using the smokeless powder was one of trial and error. However, after acquiring sufficient data on mass, velocity, and propellant weight, a graph was produced to provide a quick source for this information, Figure 12.

Prior to arming the launch tube, a number of instrumentation checks and cleaning operations were performed. As an example, debris often fell on the infrared detector lens, which had to be removed for the device to operate properly. Other operations included rotating the anvil and checking the alignment between its face and the launch tube muzzle. At this point, it was appropriate to set the standoff distance between the muzzle and the target. In parallel with these operations, the alignment and loading of the high speed movie camera were normally conducted. After alignment and checkout of the instrumentation, the aluminum housing was placed over the target and the muzzle of the launch tube.

The actual test was conducted by first loading the specimen and obturator into the launch tube. A gauge was used to position the specimen and obturator at the same location in the tube for each test. The cartridge was then placed into the chamber behind the obturator, Figure 8. The end cap was screwed onto the launch tube until marks, scribed on the gun and cap, were aligned. The electric solenoid with the firing pin was then placed on the end cap. Electrical cables, from the safe/arm control box, were then connected to the solenoid.

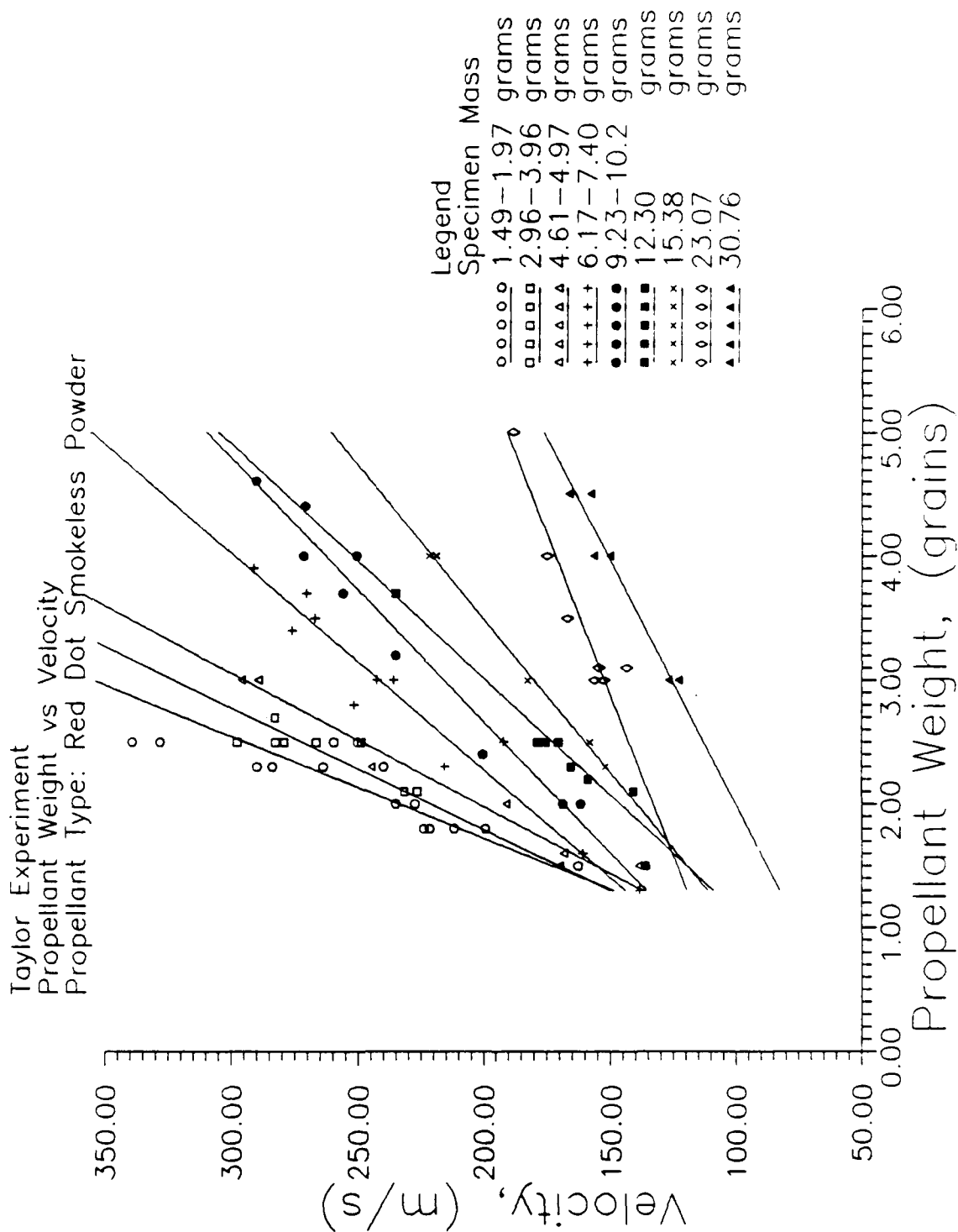


Figure 12. Propellant Weight Versus Velocity Curve for Different Specimen Masses

After arming the device, the photo lamps were turned on. At 3 seconds prior to firing, the movie camera was switched on. This allowed time for the camera to come up to its maximum framing rate before recording the impact event. At firing, an electrical signal was sent to the solenoid, which then drove the firing pin into the primer. The detonation of the primer caused the propellant to react, producing the volume of expanding gas necessary to accelerate the specimen. Following impact, the specimen was recovered from under the aluminum housing.

The material used in this investigation was received as rods 8 mm in diameter by 3.66 m in length. Each of the rods were cut into 5 smaller sections. From each section, two tensile specimens of the material were machined, a total of ten from each rod. The remainder of the section was machined, on a precision lathe, to 7.595 mm in diameter, before being cut into specimens of the desired lengths, Table 2. The range of aspect ratios covered in this investigation was from 1.5 to 10.

TABLE 2. SPECIMEN DIMENSIONS

QTY	LENGTH	DIAMETER
5	11.43 mm	7.595 mm $\begin{smallmatrix} +.000 \\ -.025 \end{smallmatrix}$
5	15.24 mm	"
5	22.86 mm	"
5	30.48 mm	"
10	38.10 mm	"
10	57.15 mm	"
15	76.20 mm	"

5. POSTMORTEM MEASUREMENTS

For making postmortem measurements, a gauge was developed to provide rapid and accurate measurements of the undeformed length, Figure 13. The gauge was machined from a piece of round stock 2.5 cm diameter by 6.3 cm in length. A 7.595 mm through hole was machined in the gauge. Then it was counterbored from one end until only a very thin portion of the original diameter hole was remaining.

Placing the undeformed end of the specimen into the through hole, measuring 7.595 mm, the plastic zone of the impact specimen would extend out of the top of the gauge. Taking the difference between the final specimen length L_f and the length of the plastic zone protruding from the gauge determines the final undeformed specimen length, l_f . This method proved quite successful at reducing scatter in the data when compared with previously used methods.

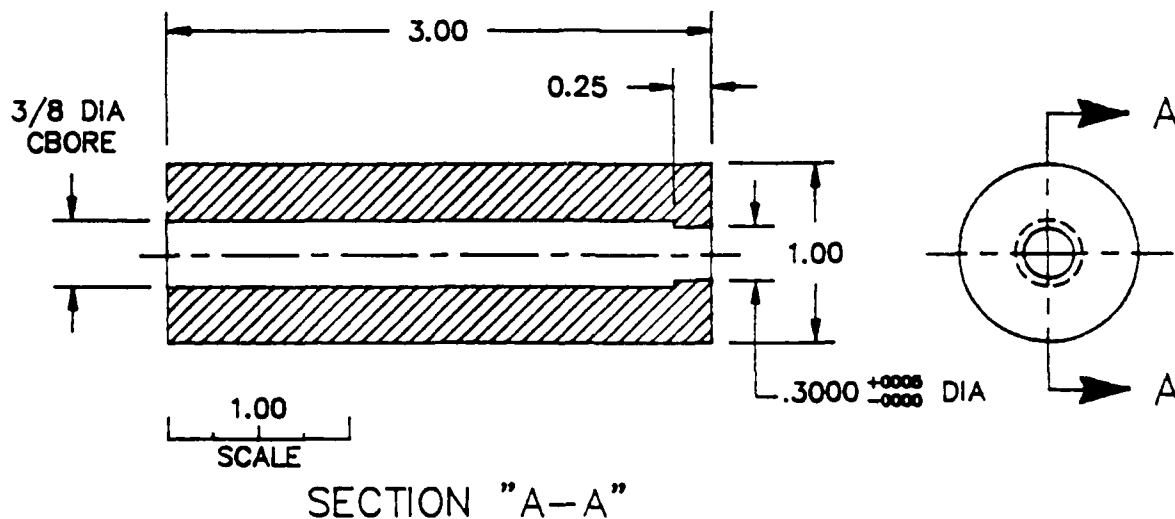


Figure 13. Detail Drawing of the Measurement Gauge

SECTION IV

ANALYSIS OF TEST RESULTS

1. INTRODUCTION

The primary goal of the experimental work was to provide a data base to use with various computer models. Information contained in the data base was used to calculate the yield stress and to construct graphs of the yield stress as a function of various experimental parameters. In addition, a study was made of the sensitivity of the computed yield stress to perturbations in the experimental data. From this study an estimate of the quantitative amount of error possible in the calculations of the yield stress can be made. This report will give evidence supporting the use of the α/β model, Reference 8, for predicting the material behavior under impact conditions.

The test matrix was designed to generate data covering a wide range of velocities, material types, and specimen aspect ratios. The experimental data, along with results calculated from the various analytical models, were organized by material type and can be found in Appendix B.

The range of impact velocities used in this investigation was 120 to 330 m/s. For a particular material, the upper boundary for the impact velocity was limited by radial cracking. For pure copper, the maximum impact velocity was approximately 200 m/s. The DPTE copper alloy had a maximum velocity of 160 m/s. For the aluminum alloys, the 2024-T4 material had a maximum velocity of 290 m/s, while the 6061-T6 had a maximum velocity of 330 m/s.

2. POSTMORTEM MEASUREMENT RELIABILITY

The reliability of the experimental measurements can be judged by monitoring the trends in the data as a function of a process variable. Figure 14 shows how the nondimensional forms of the final length, L_f/L , and the final undeformed length, l_f/L , vary with the impact velocity for the four test materials. These data show that the final length and undeformed length decrease approximately linearly with increasing velocity of impact.

After curve fitting the data by linear regression, a statistical analysis, Table 3, reveals the level of uncertainty to be found in the postmortem measurements. For the final length measurement, the largest average deviation and maximum deviation were 1.41 and 4.35 percent, respectively. A similar analysis revealed a considerable amount of scatter was present in the data for the final undeformed length. The largest average and maximum deviations were 6.75 and 42.09 percent, respectively.

The primary source of scatter in the measurement of the final undeformed length is from non-symmetric deformation. Oblique impact with the target was often found to be the source of such deformation. When a specimen impacts the target obliquely, the plastic zone will extend further down one side of the specimen than on the other. The measurement technique for determining the final undeformed length used a gauge developed with the premise that the specimen deformed in an axisymmetric manner. Specimens that were visually identified as having impacted obliquely were not measured.

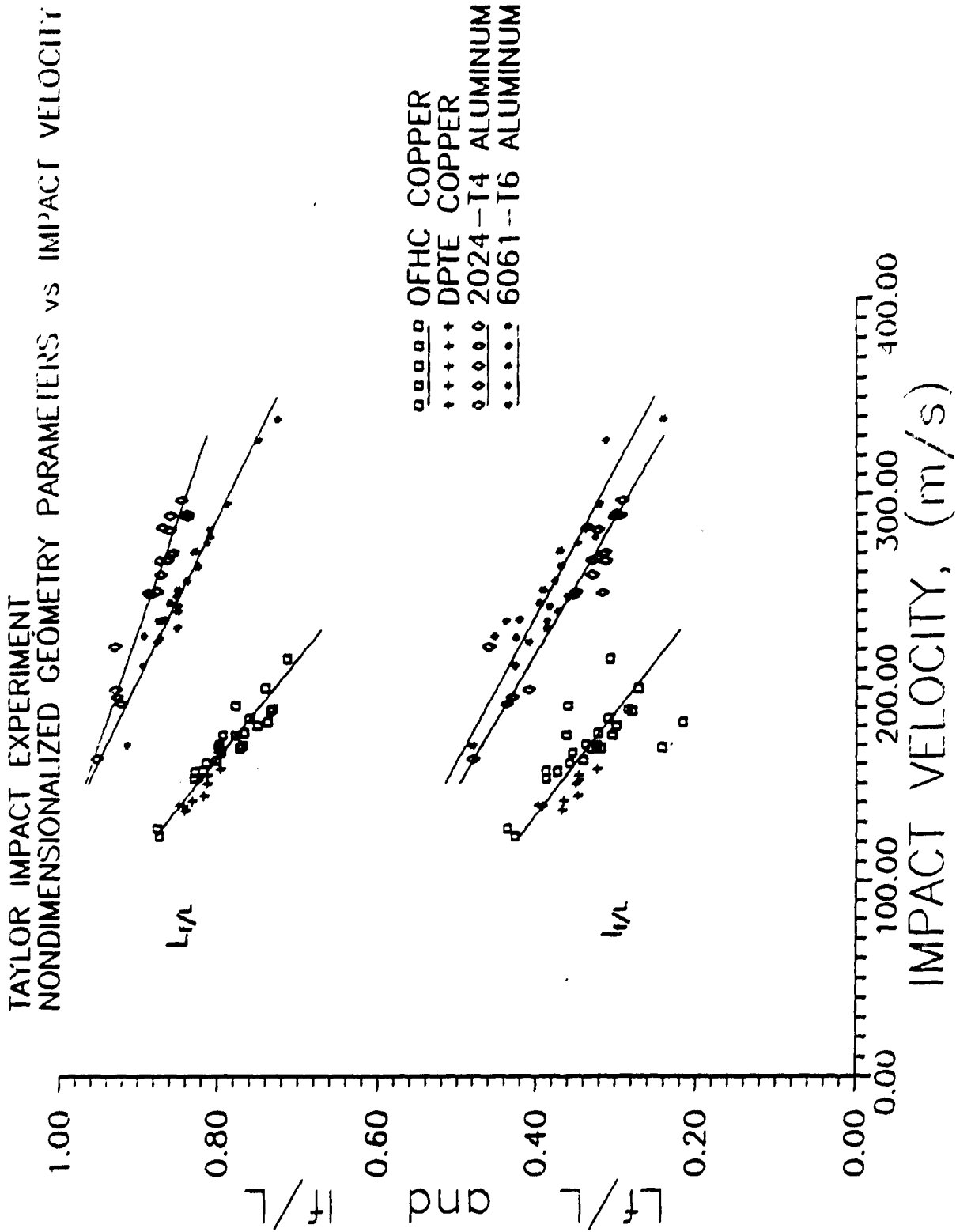


Figure 14. Nondimensionalized Parameter, L_f/L , and L_f/L as a Function of the Impact Velocity

TABLE 3. LINEAR REGRESSION AND STATISTICAL DATA

MATERIAL	DATA	SLOPE (1/cm/s)	Y-INTERCEPT (cm/cm)	AVERAGE % DEVIATION	MAXIMUM % DEVIATION
OFHC	L_f/L vs V	- 0.0020	1.124	1.41	4.35
OFHC	i_f/L vs V	- 0.0018	0.644	6.75	42.09
DPTE	L_f/L vs V	- 0.0022	1.145	0.81	1.71
DPTE	i_f/L vs V	- 0.0032	0.8327	3.32	7.22
2024-T4	L_f/L vs V	- 0.0008	1.088	0.80	2.48
2024-T4	i_f/L vs V	- 0.0014	0.712	3.70	13.95
6061-T6	L_f/L vs V	- 0.0012	1.140	0.83	2.79
6061-T6	i_f/L vs V	- 0.0013	0.712	4.02	10.36

3. STATIC AND DYNAMIC STRENGTHS

The strength of the materials, at low strain rates, was determined by quasi-static tensile tests. Specimens for the test were machined from various sections of each of the rods. The specifications for the fabrication of the tensile specimens can be found in Appendix C. The tensile tests were conducted on a screw-driven Instron machine at a crosshead displacement rate of 8.5×10^{-3} mm/s. Typical load versus time plots can be found in Appendix D.

The data obtained from the impact tests was used in a computer program which determines the dynamic yield stress of the material. The program was designed to solve for the nondimensional plastic wave speed, β , and the nondimensional yield stress, α . The parameter β is determined by Equation (41), page 19. The computer program uses an interval halving technique to solve Equation (41) for the parameter β . The parameter α is determined by Equation (37), page 18, and is directly calculable once β has been found. Knowing α and β , the yield

stress and the plastic wave speed can be easily determined from their definitions given following Equation (37), page 18.

The values of the yield stress from tensile test and those computed by the α/β model are shown in Table 4. In general, the dynamic yield stress is approximately 1.5 to 2 times the quasi-static value of the yield stress. This increase in the yield strength in the material corresponds to a change in the strain rate of 7-8 orders of magnitude.

In Table 4, the yields stress values for the two copper materials were not reported. The response of the copper

TABLE 4. COMPARISON OF STATIC AND DYNAMIC YIELD STRESS VALUES

MATERIAL	QUASI-STATIC (TENSILE TEST)		DYNAMIC (IMPACT TEST)
	YIELD STRESS	ULTIMATE STRESS	YIELD STRESS
OFHC	—	350 Mpa	550 Mpa
DPTE	—	300 Mpa	520 Mpa
2024-T4	400 Mpa	500 Mpa	750-900 Mpa
6061-T6	315 Mpa	340 Mpa	550 Mpa

materials to loading was affected by the high dislocation density pre-existing in the material. This material condition created a load versus time curve, Appendix D, in which the stress level rose linearly to a maximum value and then immediately decreased. The high dislocation density in the material effectively eliminated the work hardening region of the stress versus strain curve.

4. SENSITIVITY ANALYSIS

An estimate of the error found in the computed value of the yield stress can be determined from a sensitivity analysis.

This analysis was conducted by estimating the level of accuracy associated with each experimental measurement, e.g., the final undeformed length. The value of the yield stress was recalculated after the data were perturbed an amount equal to the uncertainty in each measurement. A quantitative estimate of the possible error is found by comparing the baseline value of the yield stress with those found in the sensitivity analysis.

The measurements of specimen geometry, the final length, and the final undeformed length were estimated to be accurate to within ± 0.025 mm and ± 0.076 mm, respectively. The velocity measurements were considered accurate to within ± 3 m/s. The accuracy imposed on the velocity measurement system is taken from an analysis of the uncertainty of data generated by the pressure transducers. It was assumed for this analysis that the wave forms recorded provided the optimum level of resolution and the information was collaborated by the infrared detector and the high speed photography techniques previously discussed. Correlating the velocity data between the various measurement systems provided an increased level of confidence in the accuracy of the measurement. By choosing the results of a particular impact test as a baseline, the effect of possible inaccuracies in the experimental parameters on the computed yield stress can be studied.

Table 5 shows a set of baseline values for two different pure copper specimens with aspect ratios of 1.5 and 10. By examining the data from specimens with different geometries, the relative influence of possible inaccuracies can be considered. Perturbed values of these parameters, according to the assumed accuracy of the measurement, are shown in the columns headed with a plus and a minus sign.

In Table 6, the dynamic yield stress values are given for the baseline and from computations using the perturbed parameter

TABLE 5. EXPERIMENTAL TEST DATA

MEASUREMENT	ASPECT RATIO					
	1.5			10		
	-	BASELINE	+	-	BASELINE	+
L_f	9.093 mm	9.119 mm	9.144 mm	60.528 mm	60.554 mm	60.579 mm
l_f	3.708 mm	3.785 mm	3.861 mm	27.000 mm	27.076 mm	27.153 mm
V	165.3 m/s	168.3 m/s	171.3 m/s	163.0 m/s	166.0 m/s	169.0 m/s

values. In making the calculations only one of the three measurements were varied from the baseline value. For example, in the first row, using a specimen with L/D of 1.5, the yield stress was calculated using a value of the final length of 9.093 mm, 9.119 mm, and 9.144 mm; the baseline values were used for the other two parameters, l_f and V . In the second and third row of Table 6, the perturbed parameter was the undeformed length and velocity, respectively. A quantitative estimate of the uncertainty can be determined from a ratio of the difference between the computed yield stresses found using the perturbed experimental parameters to the baseline value. The percent errors were 3.4, 2.0, and 7.2, for measurements of L_f , l_f , V , respectively, for a specimen with an aspect ratio of 1.5. By comparison, the second set of data produced percentage error values of 0.6, 0.4, and 7.2, from measurements of L_f , l_f , and V , respectively. The velocity measurement provided the greatest source of uncertainty in both data sets. By comparison to the velocity measurement, the deformed specimen geometry had little influence on the overall uncertainty of the computed yield stress value.

An argument could be made that additional combinations of the various parameters would produce a larger deviation from the baseline value. Note in Table 6 that a reduction of the geometry parameters, L_f and l_f , had an opposite effect on the computed yield stress value. Reducing the final undeformed length, l_f ,

increases the stress value, while a reduction in the final length, L_f , decreases the calculated stress. It was considered that the actual uncertainties in postmortem measurements would be small, or possibly cancel one another, by comparison to those found in the velocity measurement. Therefore, the yield stress values reported in Table 6 as baseline values and those given in Appendix B, are accurate to within ± 5 percent.

TABLE 6. COMPUTED YIELD STRENGTH VALUES

VARIANCE	ASPECT RATIO					
	1.5			10		
	-	BASELINE	+	-	BASELINE	+
L_f	549 Mpa	559 Mpa	568 Mpa	510 Mpa	512 Mpa	513 Mpa
l_f	564 Mpa	559 Mpa	553 Mpa	513 Mpa	512 Mpa	511 Mpa
V	539 Mpa	559 Mpa	579 Mpa	493 Mpa	512 Mpa	530 Mpa

5. EFFECT OF SPECIMEN GEOMETRY

The influence of initial specimen geometry on the calculated yield stress was another effect of interest in this investigation. Figure 15 shows the calculated value of yield stress as a function of the aspect ratio, L/D , of the specimen. These data show that the specimen geometry did not influence the yield stress value calculated by the model, with the exception being the 2024-T4 material.

The 2024-T4 aluminum shows an increase in the yield stress with short specimens. The value of the yield stress varies from 750 MPa, for L/D 's of 5 and greater, to near 900 MPa, for L/D 's of 1.5 and 2. While the uncertainty is somewhat greater for smaller specimens, in terms of the yield calculations, there are sufficient data to suggest the indication of a specimen geometry related trend.

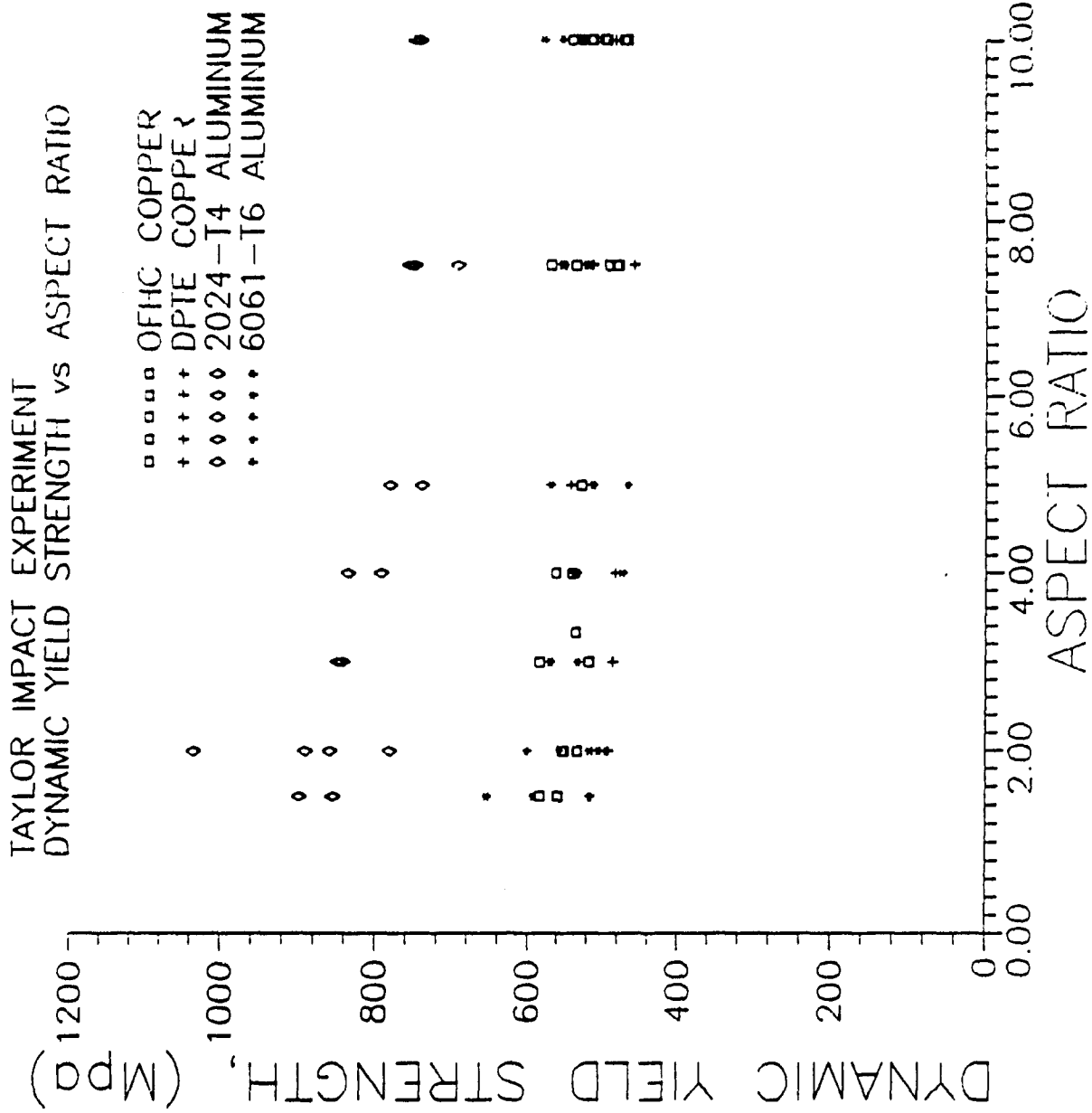


Figure 15. Values of the Yield Stress as a Function of the Specimen Aspect Ratio

If the increase in yield stress occurred because of inaccuracies in the postmortem measurements, the results for the other three materials should be affected as well. This supports the indication that the specimen geometry does influence the yield stress for this type of material. How the specimen geometry affected the results can be studied by examining the data obtained from the experiment.

Recall that the nondimensional forms of the final length and final undeformed length were shown to decrease linearly with increasing velocity, Figure 14. The statistical analysis, Table 3, shows that the curve fit by linear regression of the data produced a slope that was equal for the two parameters, with the exception being the 2024-T4 alloy. Data for the 2024-T4 material show that the final undeformed length changed at a faster rate, with velocity, than did the final length of the specimen. These results indicate direct physical evidence of a unique material behavior for this alloy.

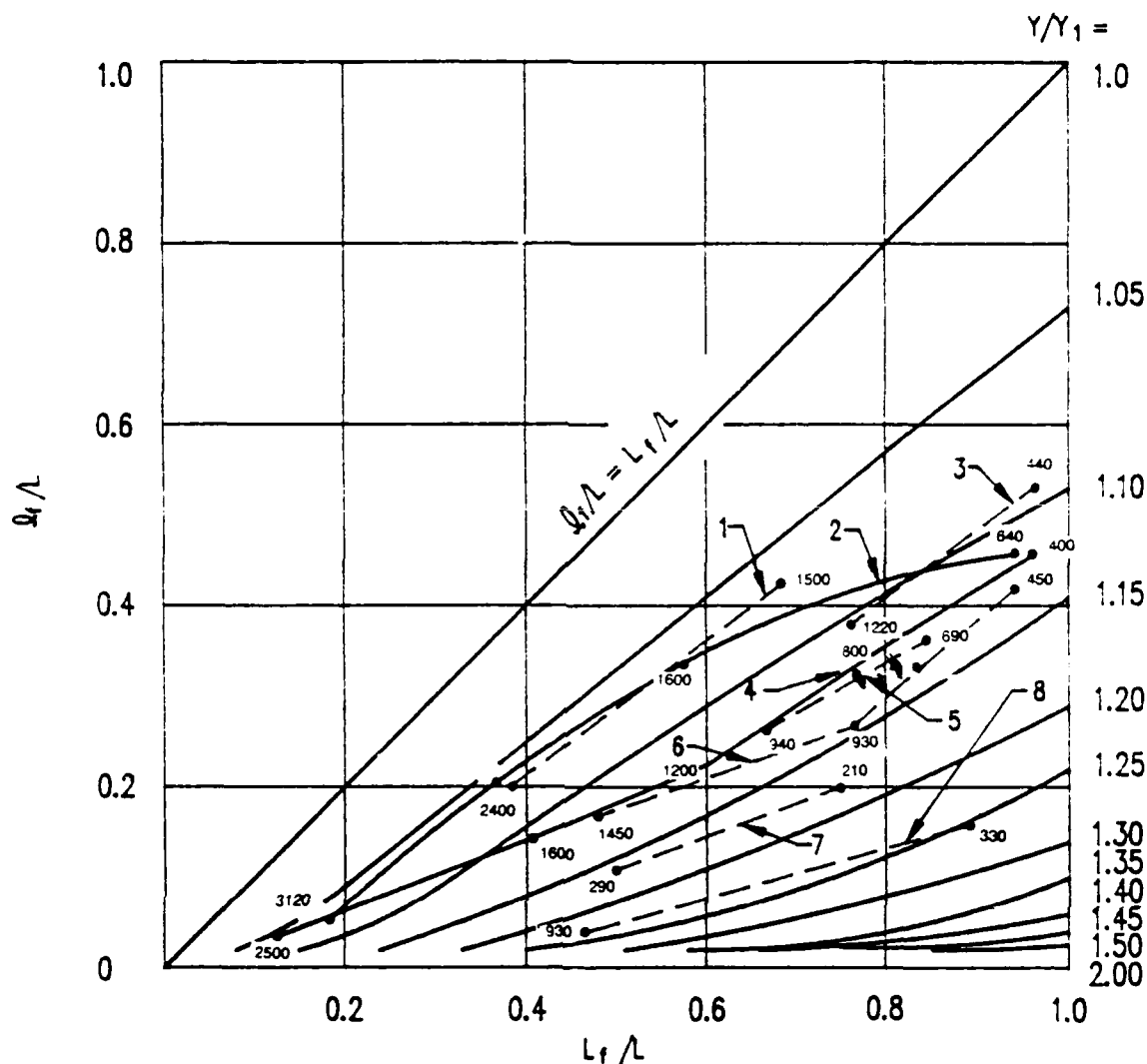
One of the methods used to characterize material behavior by Whiffin, Reference 9, in the original investigation was to plot the nondimensional form of the final undeformed length against the nondimensional form of the final length, Figure 16, Reference 9. For the current investigation similar data are plotted in Figures 17(a) and 17(b). Whiffin used this method of displaying the data to comply with a requirement of the Taylor model, from which the value derived from an explicit formula of the yield stress, Equation (18), page 10, could be used to calculate a more precise value using the correction contours.

The purpose for showing Figures 16 and 17, is to discuss the results of the original investigation in light of the current work. The results shown in Figure 16 for Normal Dural are to be compared with the results shown in Figure 17 for the 2024-T4 material.

The velocities shown next to the data points in Figure 16 indicate that the complex state of stress in the material accompanying fracture was not considered in that investigation. Therefore, only one of the four data points shown for Normal Dural would be acceptable in regard to the no fracture requirement imposed on the current test data. The data point for impact velocity of 640 ft/s, (195 m/s), is in agreement with the values in the current investigation.

Whiffin draws the conclusion from the data that for a specific value of l_f/L , the ductility of various materials can be identified from the parameter L_f/L . Whiffin identifies the trend that at a specific value of l_f/L higher values of L_f/L occur for more ductile materials. In Figure 17, it can be seen that for a specific value of the final undeformed length parameter, l_f/L , increased ductility will decrease the value of the final length, not increase it. For example, the 2024-T4 material has less ductility than does 6061-T6, and is, therefore, found to the right of the data for 6061-T6. This misinterpretation of the data occurred because of the limited amount of data that was available and the relatively crude measurement technique employed to make the postmortem measurements.

A trend in the data can be identified, for the 2024-T4 alloy, when the aspect ratio of the specimen is plotted on the data point, Figure 17(b). In general, the lower L/D 's are shifted toward higher values of the nondimensional final length parameter. This trend in the data identifies the relationship between the postmortem geometry measurements that are influencing the computed value of the yield stress. As shown by the sensitivity analysis, reducing the final undeformed length produces an increase in the yield stress. Consequently, this shift in the data for specimens with lower L/D 's produced the results shown in Figure 15.



REF. NO.	MATERIAL	STATIC STRENGTH (TONS/SQ. IN.)	AVERAGE DYNAMIC STRENGTH (TONS/SQ. IN.)
1	ARMOUR PLATE	73	115
2	"NORMAL" DURAL	19	31
3	HARD DURAL	25-85	39
4	MILITARY STEEL	18	49
5	ARMCO IRON	--	50
6	SOFT DURAL	8-15	19
7	LEAD	--	2.8
8	COPPER	--	15.5

THE SMALL FIGURES IN THE DIAGRAM SHOW THE STRIKING VELOCITY EMPLOYED.

Figure 16. Nondimensional Form of the Undeformed Final Length as a Function of the Nondimensional Final Length Parameter

TAYLOR IMPACT EXPERIMENT

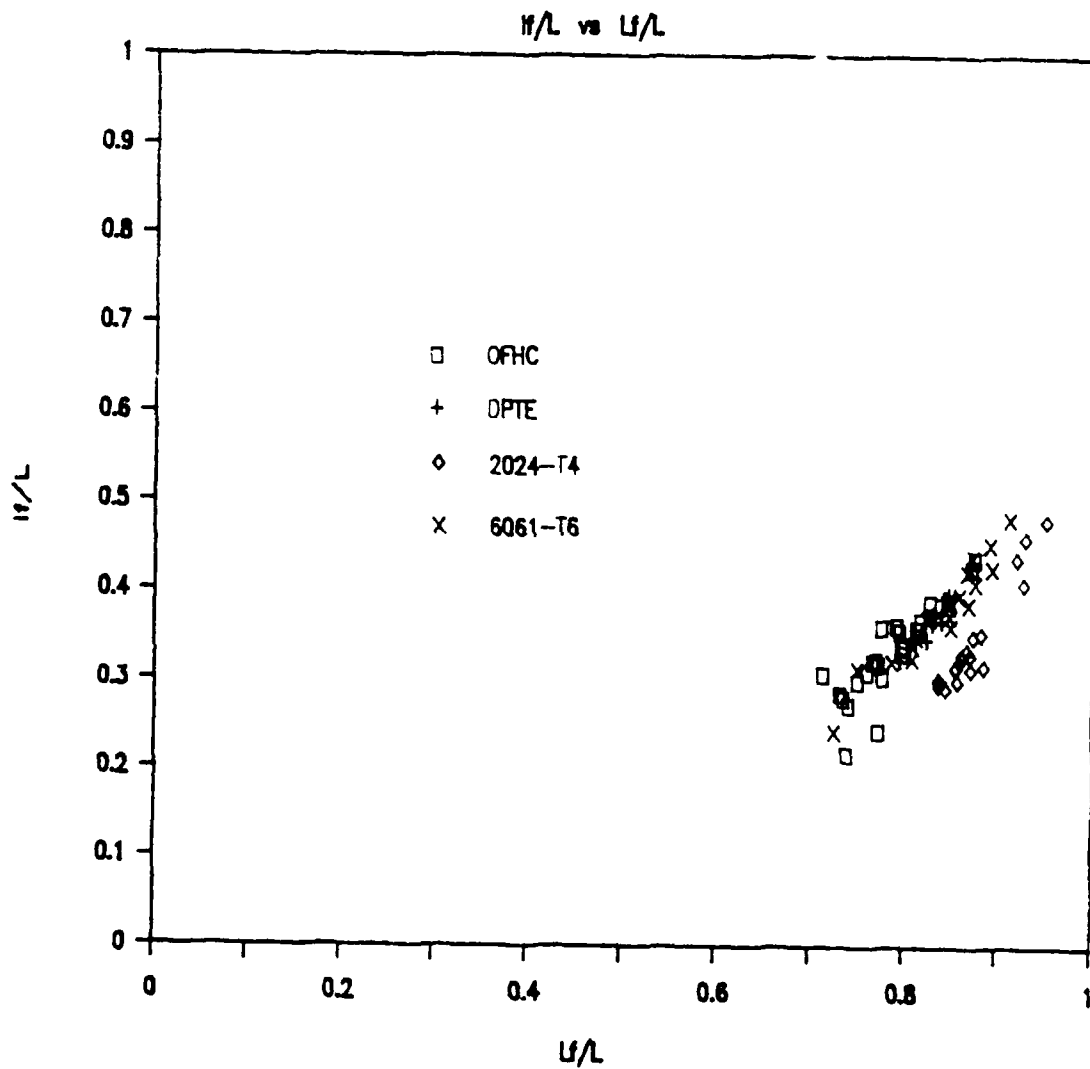


Figure 17a. Ballistic Geometry Data, in Nondimensional Form, for the Current Investigation

TAYLOR IMPACT EXPERIMENT

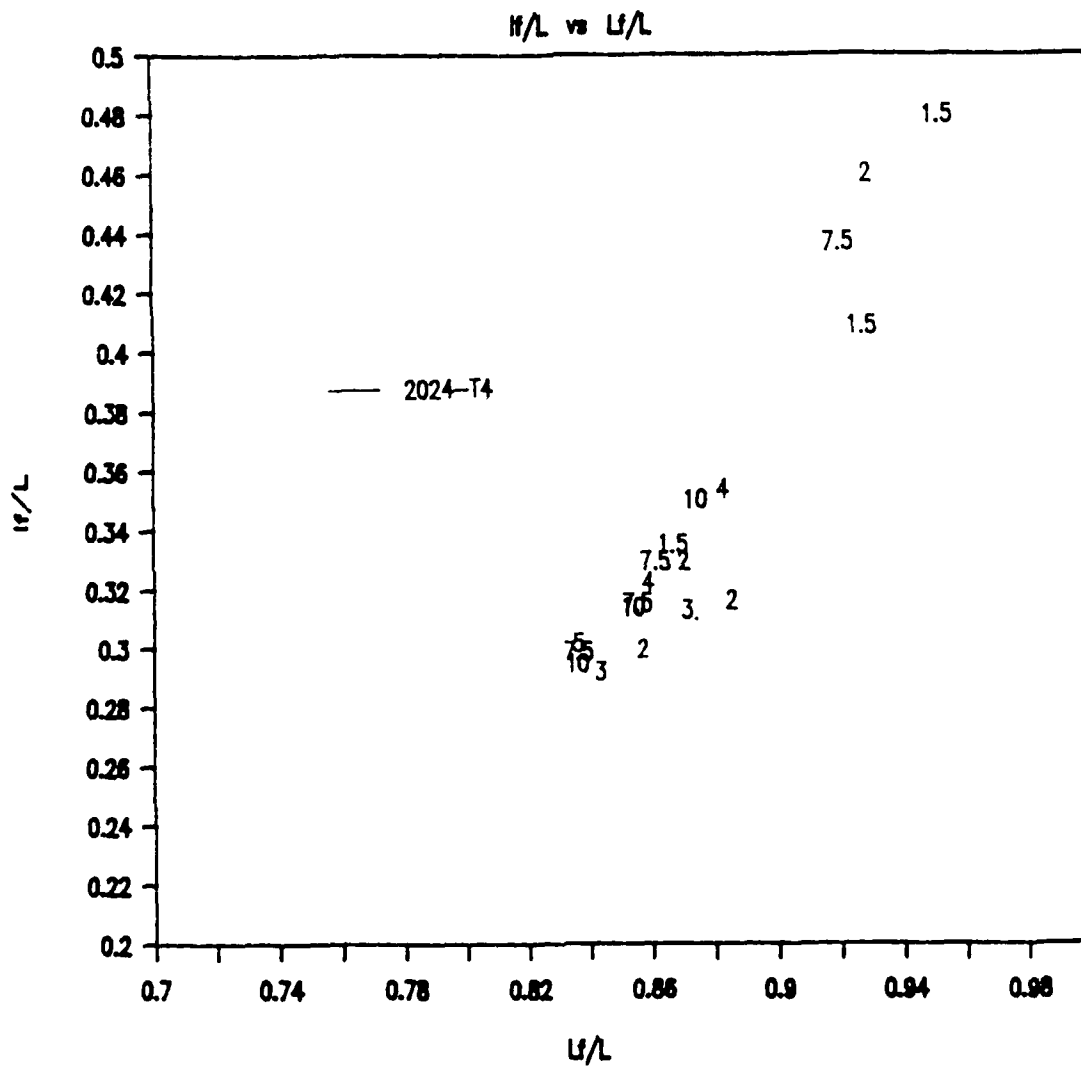


Figure 17b. Ballistic Geometry Data, in Nondimensional Form, for 2024-T4 Specimens

6. MUSHROOM GROWTH

The measurement of the final diameter of the specimen at the target/specimen interface indicates that the mushroom growth is correlated with the available energy on impact, Figure 18. A comparison between short and long specimens shows that the final diameter is proportionally greater for longer specimens, depending on the mass increase, for equal impact velocities. These results indicate that the final diameter of the mushroom is dependent on the strength of the material and the kinetic energy at impact.

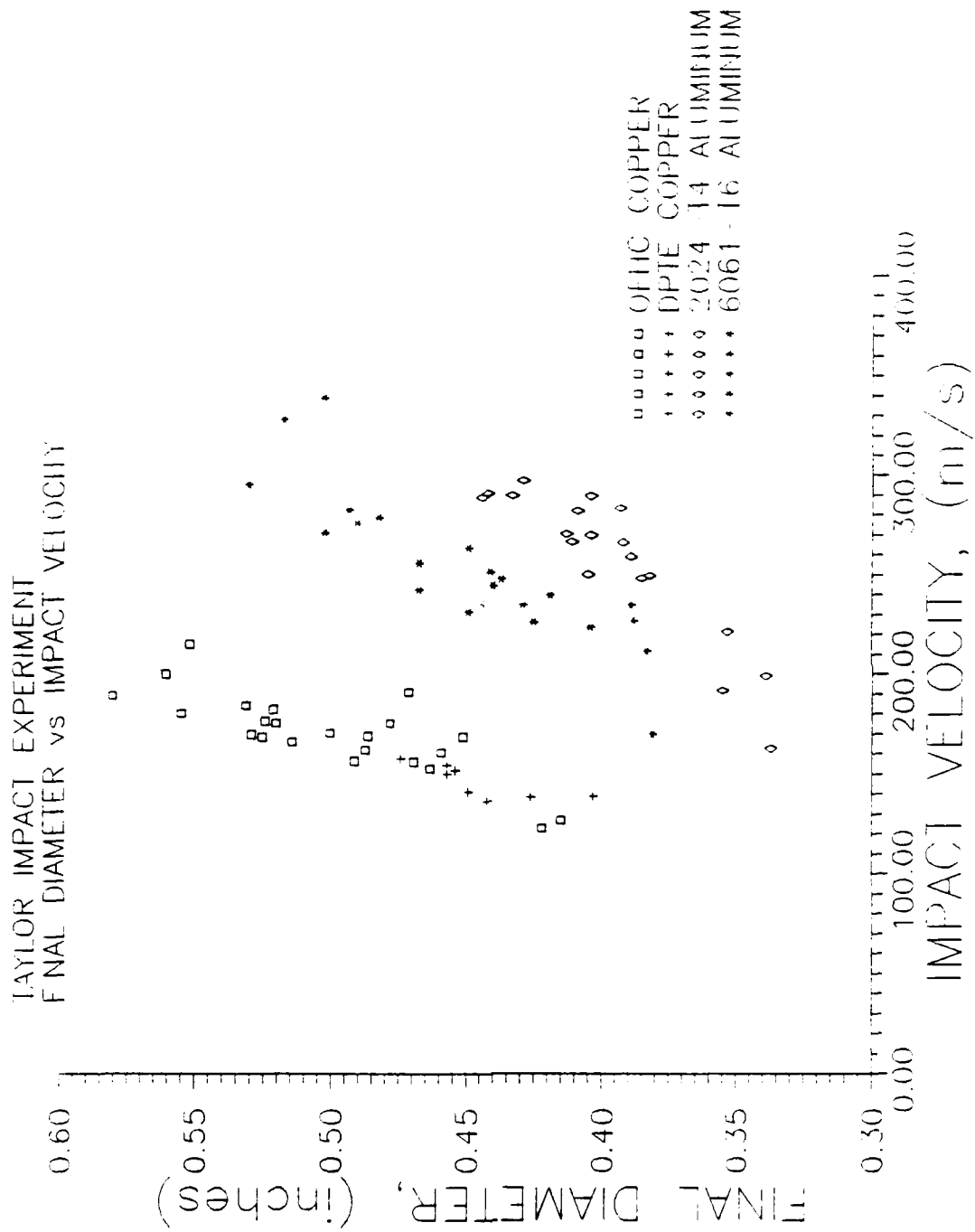


Figure 18. Final Diameter as a Function of the Impact Velocity

7. HIGH SPEED PHOTOGRAPHY

The Cordon framing camera was used to generate a photographic record of a particular impact test (UK-145). The camera was operated at a framing rate of 300,000 frames per second. At this rate, the resolution of the photographic data was $3.33 \mu\text{s}$. The impact event was photographed using a shadowgraph technique. Measurements taken directly from the photographs provided data on the mushroom growth and the rear end position both as a function of time.

The data obtained on the mushroom growth rate, Figure 19, indicates the magnitude of the strain rates seen at the

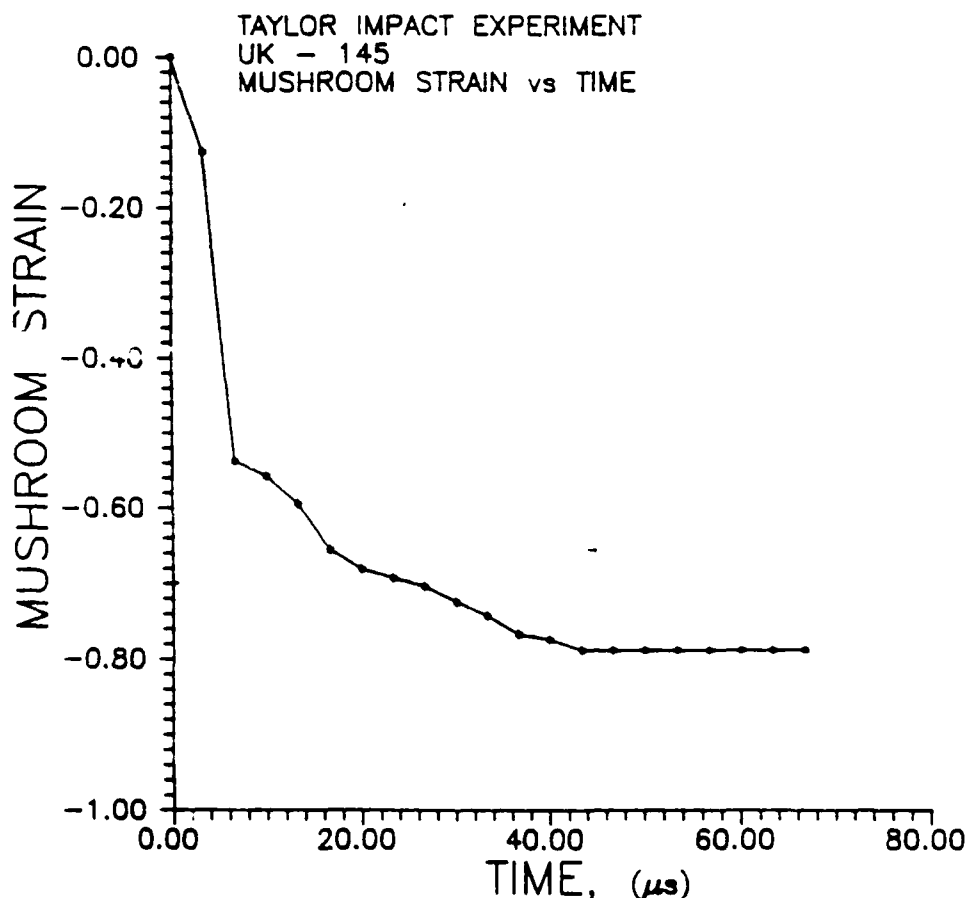


Figure 19. Strain at the Target/Specimen Interface as a Function of Time

specimen/target interface. The photographs show that the bulk of the mushroom growth process occurs within the first few microseconds and is completed by 40 μ s after impact. The slope of the curve in Figure 19 gives a strain rate of 7.5×10^4 /s during the first 7 μ s.

The data on the position of the rear end of the specimen as a function of time shows that it took 120 μ s to bring the specimen to rest, Figure 20. The velocity of the rear end is simply the slope of the curve. The data show that the initial velocity, 190 m/s, did not change until approximately 45 μ s after impact.

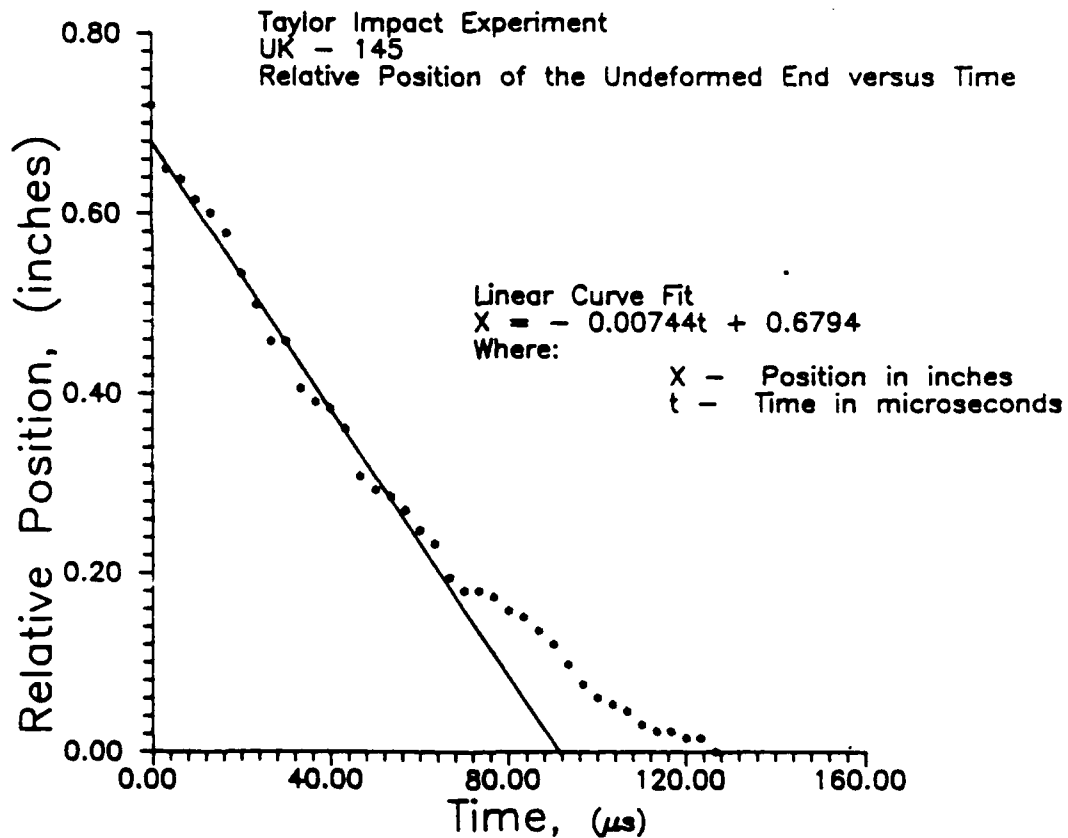


Figure 20. Position of the Undeformed End of the Specimen as a Function of Time

The analytical models which attempt to describe the physical process assume that the plastic front moves at a uniform velocity throughout the event. The calculated plastic wave speed from the α/β model should be considered to be an average value. For the particular test that was photographed with the framing camera, a comparison of the plastic wave speed calculated from the model can be made with experimental results. Knowing the duration of the event and the distance traveled by the plastic wave, a velocity was determined. For test UK-145, the model computed a value of 202 m/s for the parameter, λ . From the photographs, the plastic wave speed is calculated to be 212 m/s, which is in good agreement with the value predicted by the model.

SECTION V

MICROSTRUCTURE

1. INTRODUCTION

The materials considered for this investigation varied widely in their microstructural features. The differences in deformed geometries reflect how the microstructure of each material influenced the mechanisms for plastic deformation. The principal aspect of this study is how the basic microstructure affects the way the material absorbs the energy of impact.

Macroscopically, the features of a deformed specimen were similar for all of the materials. The grains on the axis near the anvil, which are subjected to high compressive loads, are extensively deformed. The longitudinal compressive strains impart radial motion to the deforming body to produce the characteristic mushroomed profile. The extent of the deformation process is governed by various aspects of the microstructure, which is controlled by the thermo-mechanical history of the material and its chemical composition.

The structures found in the materials used for this investigation were of three types: single phase, multiphase containing inclusion particles, and multiphase containing inclusions and coherent precipitates. The first of these structures is found in OFHC copper (99.99 Cu). The second type is found in DPTE copper and in 6061-T6 aluminum. The last type is found in 2024-T4 aluminum. The constituents found in each of the materials are given in Table 7. The heat treatments specified for the aluminum materials correspond to a solution anneal followed by artificial aging, for 6061, and natural aging, for 2024. Some specimens of OFHC copper were annealed for 1 hour at 600°C in a vacuum. The nomenclature annealed copper and half hard copper will henceforth be used to denote

the CFHC copper in the annealed and as-received conditions, respectively.

All of the materials were examined by optical microscopy both before and after impact. The OFHC coppers were more extensively studied. In addition to optical examination, X-ray diffraction and transmission electron microscopy (TEM) techniques were used to study the microstructure and the effect of high strain rate deformation.

2. DPTE COPPER

The DPTE copper material is a copper/tellurium alloy. Tellurium is added as a solution strengthening element in small amounts. A small concentration of phosphorous is added as a deoxidizer. The phosphorous removes oxygen from the copper matrix by forming oxide inclusion particles. During hot rolling of the material these inclusions are broken up and elongated in the rolling direction. The final structure after cold working the material shows a fine grain structure with an extensive number of stringers elongated parallel to the rod axis, Figure 21.

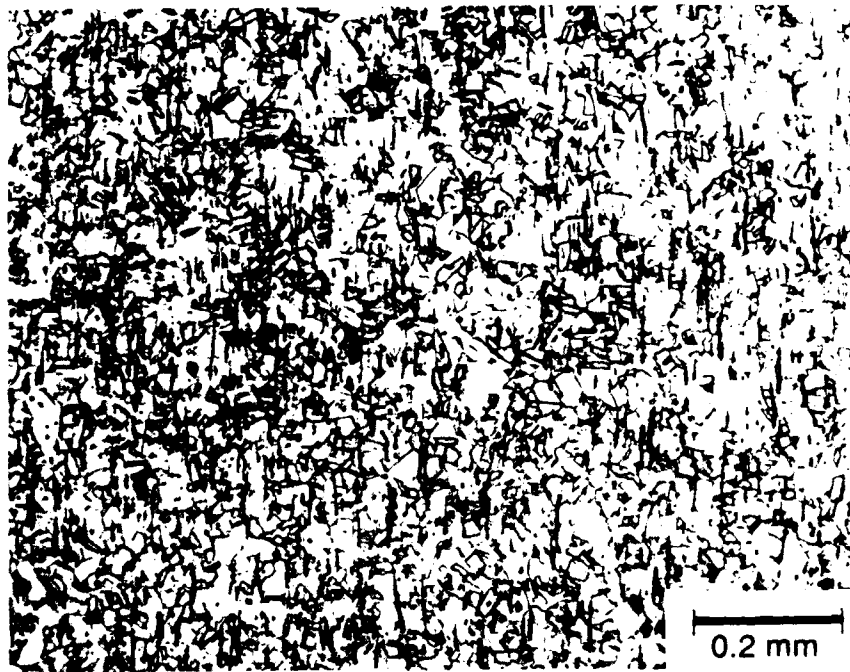


Figure 21. Optical Micrograph Showing the Microstructure of DPTE Copper

3. 6061-T6 ALUMINUM

The 6061-T6 is a ternary aluminum alloy containing small concentrations of silicon and magnesium. Age hardening will produce a matrix of aluminum with magnesium in solution and precipitates of Mg_2Si . These precipitate particles will be

spherical in shape, Figure 22, and will be incoherent with the matrix. In commercial grades, inclusions of aluminum oxides and iron/silicon compounds will be found that are not affected by subsequent heat treatment. The size of the misfit between lattice types, the aluminum matrix and the precipitate, produces a small internal strain field surrounding each precipitate. This small strain field produces little disruption to the motion of dislocation which occurs under an applied load.



Figure 22. Optical Micrograph Showing the Microstructure of 6061-T6 Aluminum

The shape of the precipitate particles reduces the number of potential sites for localized stress concentration. In turn, preventing the localized buildup of stress inhibits crack nucleation and growth. This microstructure in the 6061-T6 alloy provides a relatively low yield strength, but gives it a high toughness, i.e., the ability to absorb energy before fracture.

4. 2024-T4 ALUMINUM

The 2024-T4 is a ternary aluminum alloy containing copper and magnesium. Allowing the material to naturally age after solution anneal provides the opportunity for coherent Al_2Cu precipitates to form on (001) habit planes. In addition, magnesium and aluminum oxides form inclusion particles in the matrix, Figure 23. The formation of the coherent Al_2Cu precipitates, which have a large misfit with the matrix, prevents the easy motion of dislocations on the slip planes. Therefore, the material shows increased strength by comparison to the 6061-T6 alloy, see Table 1.

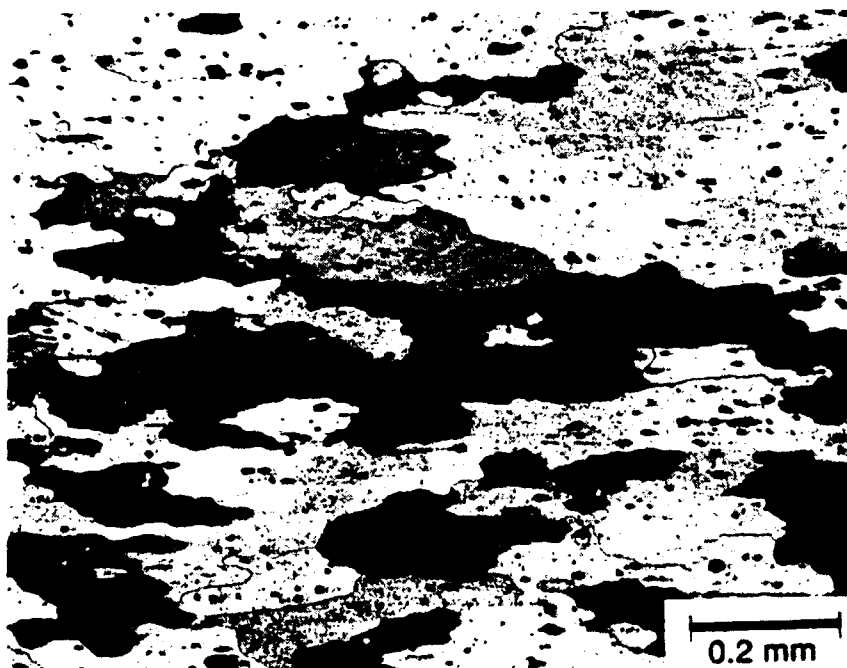


Figure 23. Optical Micrograph Showing the Microstructure of 2024-T4 Aluminum

5. OFHC COPPER

Optical examination of the half hard OFHC copper material shows that slip is the primary mode of accommodating the deformation introduced by drawing, Figure 24. TEM thin foils of

the material showed an extensive substructure containing an inhomogeneous distribution of dislocations, Figure 25. The parallel bands seen in Figure 25 indicate that deformation twins were formed during the processing of the material.

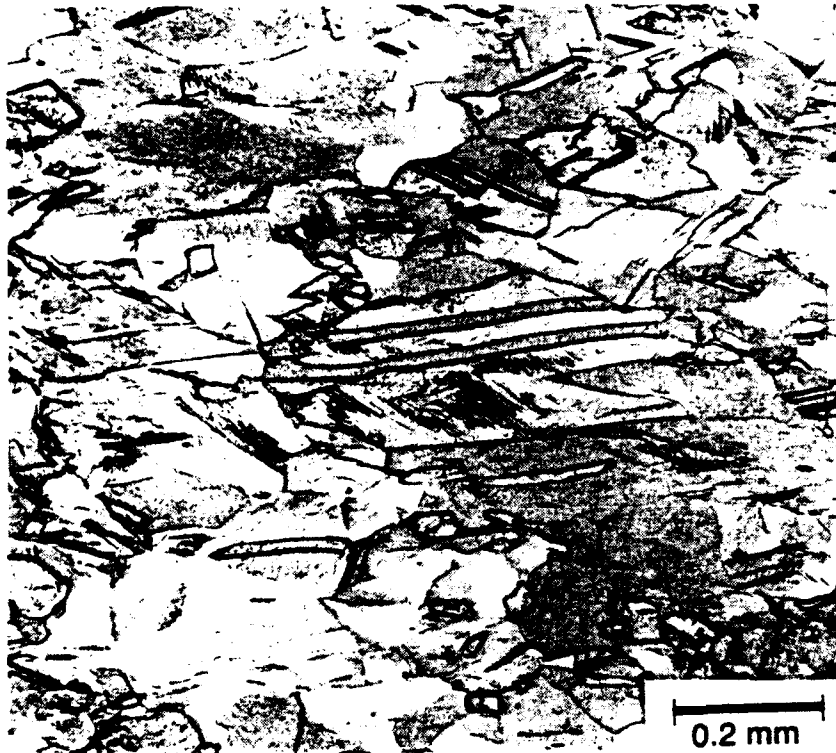


Figure 24. Optical Micrograph of the Microstructure of Half Hard OFHC Copper

Reports by Ahlborn and Wassermann, Reference 11, and Wassermann, Reference 12, cite evidence that the following conditions give an increased incidence of mechanical twinning in drawn copper wire:

- a. lowering the deformation temperature, Reference 13,
- b. increasing the amount of deformation,
- c. lowering the stacking fault energy by alloying.

The as received material was in a half-hard condition, which means that following the final anneal there was a reduction in cross sectional area of 30 to 60 percent. This amount of straining satisfies condition b, reported above, and is confirmed by the TEM observations in Figure 25.

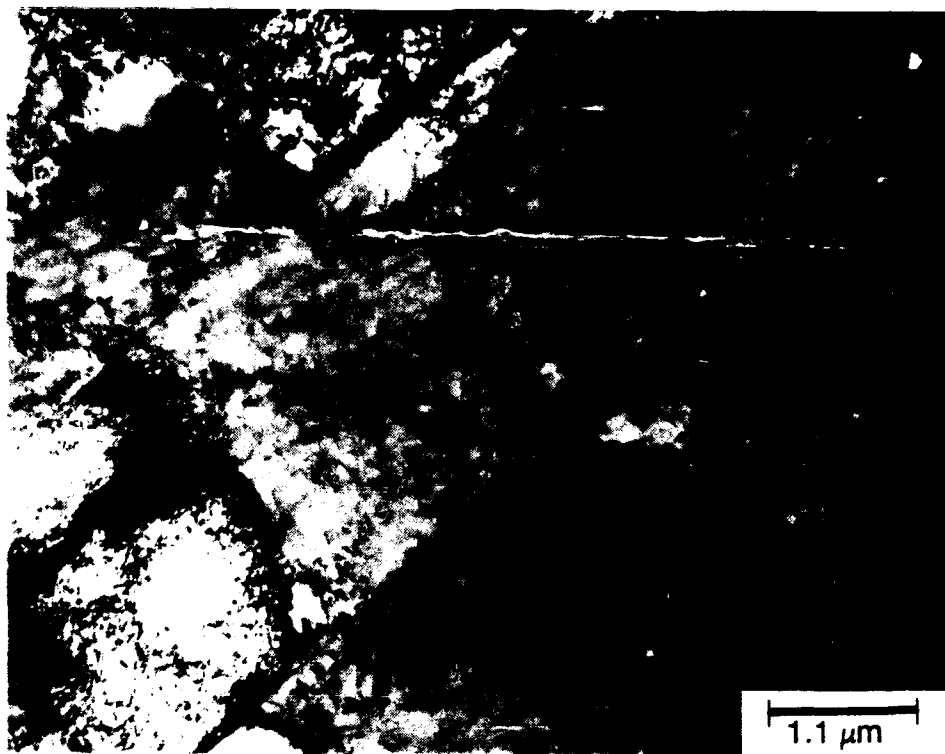


Figure 25. TEM Micrograph of Half Hard OFHC Copper



Figure 26. Optical Micrograph of the Microstructure of Annealed OFHC copper

Pole figures were generated to determine the textures of the half-hard and annealed OFHC copper materials. Because of the drawing operation, the texture in the half hard material was found to be oriented parallel to the rod axis and was a superposition of (111) and (001) fiber textures. The annealed material had a random grain orientation with an approximate grain size of 40 μm . Compare Figures 24 (half hard) and 26 (annealed).

6. MICROSTRUCTURE RESULTING FROM IMPACT

With different metallurgical histories, two copper specimens which impact the target at similar velocities accommodated the energy in significantly different ways. Examination of the post-impact geometries reveal how the microstructure influenced the deformation, Figure 27. The specimen on the left was deformed in the half-hard condition. The specimen on the right was deformed in the annealed condition. The three post-mortem measurements of the geometry that were visibly influenced by the microstructural differences are the final mushroom diameter, the final length, and the extent of the plastic deformation in the specimen.

The half-hard copper specimen had a much greater change in diameter. The annealed specimen had a greater reduction in final length and was traversed entirely by the plastic wave in the material. From these observations, it is quite evident that the dislocation density in the material had a significant role in how the impact energy was absorbed.

Following impact, both types of copper specimens were sectioned parallel to the rod axis. An optical examination was conducted near the mushroom face close to the original rod axis, Figures 28 and 29. The large compressive loads are evident by the collapse of the grains. After impact, the grains of the annealed material run parallel to the target face, Figure 28.

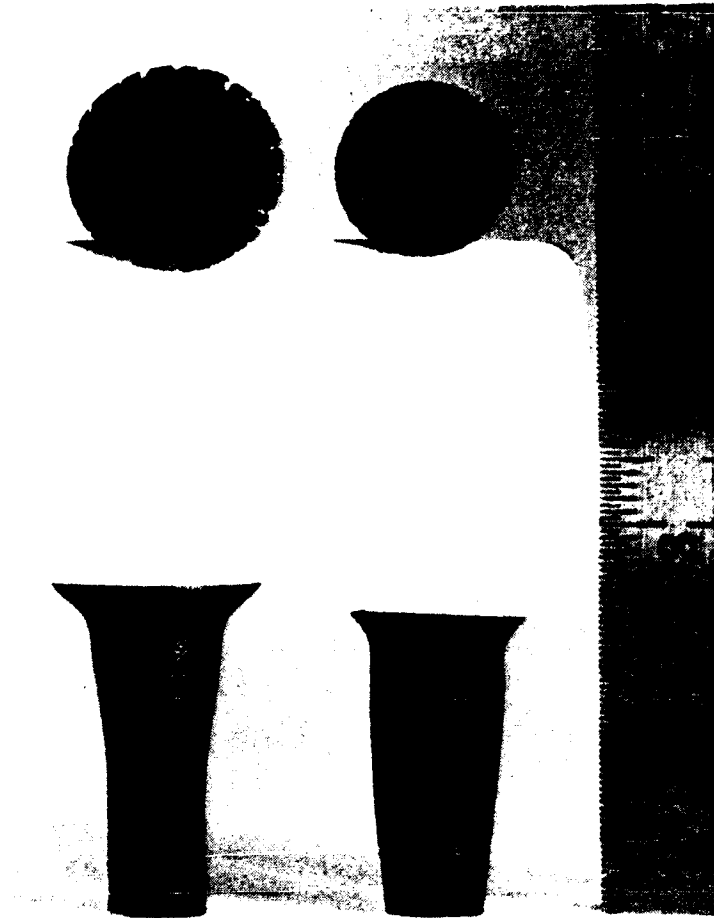


Figure 27. Impact Specimens of OFHC Copper

In contrast, the half-hard copper specimen contains small, randomly oriented grains, Figure 29. These grains indicate that the mechanical history of the material created a condition suitable for recrystallization to occur as a result of impact.

To confirm this observation, back reflected Laue patterns were generated from both types of impact specimens. The x-ray beam was positioned to strike near the same location as shown in the optical micrographs. Results for the annealed impact specimens showed two diffuse rings. The impact specimen used in the half-hard condition showed two rings made up of numerous intense spots. These bright spots occur because of the increase

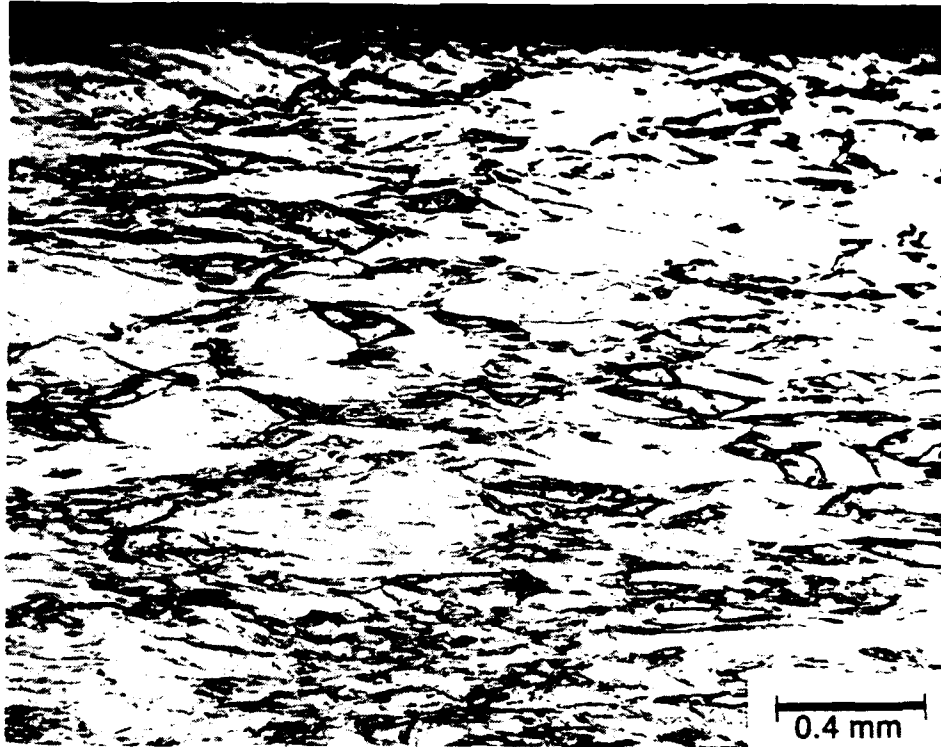


Figure 28. Optical Micrograph Showing the Microstructure of Annealed OFHC Copper After Impact



Figure 29. Optical Micrograph Showing the Microstructure of Half Hard OFHC Copper Specimen After Impact

in size of the coherently diffracting domain created by the recrystallization process.

The high dislocation density in the half hard material had a significant effect on the behavior in both impact tests and tensile tests. In tensile tests, performed for quasi-static characterization of the material, the high dislocation density effectively eliminated the strain hardening region of the load versus time plot, Appendix D. The load increased linearly until localized plastic deformation occurred so that the yield and ultimate strengths of the material coalesced into one point. During the deformation on impact, the dislocation density influenced how the material absorbed the energy. As previously mentioned, this observation is evident by the macroscopic features of the post-impact geometry, Figure 27. The post-impact geometries suggests that recrystallization occurred in the half-hard material because the heat generated by plastic work was more intense. In addition, the increase in stored energy in the material caused by cold working reduces the amount of energy required for recrystallization. The temperature for the recrystallization of copper is 225°C.

After impact, TEM thin foils were made from both types of copper materials. The half-hard material showed a high incidence in the number of deformation twins, Figure 30. Since the material had contained twins initially, the source of the twins could have been either the impact event or the processing of the original rod stock. However, deformation twins were also found in the specimens of annealed material. These could only have been produced by impact.

TEM replicas were taken from the surface of the sectioned half-hard impact specimen. Examination of these replicas revealed an orientation relationship that identified the formation of a twin with the impact event, Figure 31. Previous investigators, Reference 14, identified similar artifacts as

compression twins formed in shock loaded single crystals of pure copper. (See Figure 14, in Reference 14.)



Figure 30. TEM Micrograph Showing Deformation Twins in OFHC Copper

Brilhart and coworkers, Reference 15, investigated the formation of deformation twins in polycrystalline pure copper by shock loading the material using flyer plate experiments. In these experiments the pressures responsible for the formation of deformation twins were on the order of 7.5 GPa.

The observation of deformation twins in pure copper Taylor test specimens suggests the level of pressure in the material on impact. The pressure on contact between the specimen and the target was estimated by a model constructed using Hugoniot relationships, as detailed in Appendix E. From this analysis the pressure at the moment of impact, in a copper specimen striking a steel anvil at an initial velocity of 200 m/s, is 3.9 GPa. This estimated pressure is nearly an order of magnitude above the dynamic yield stress of the material.

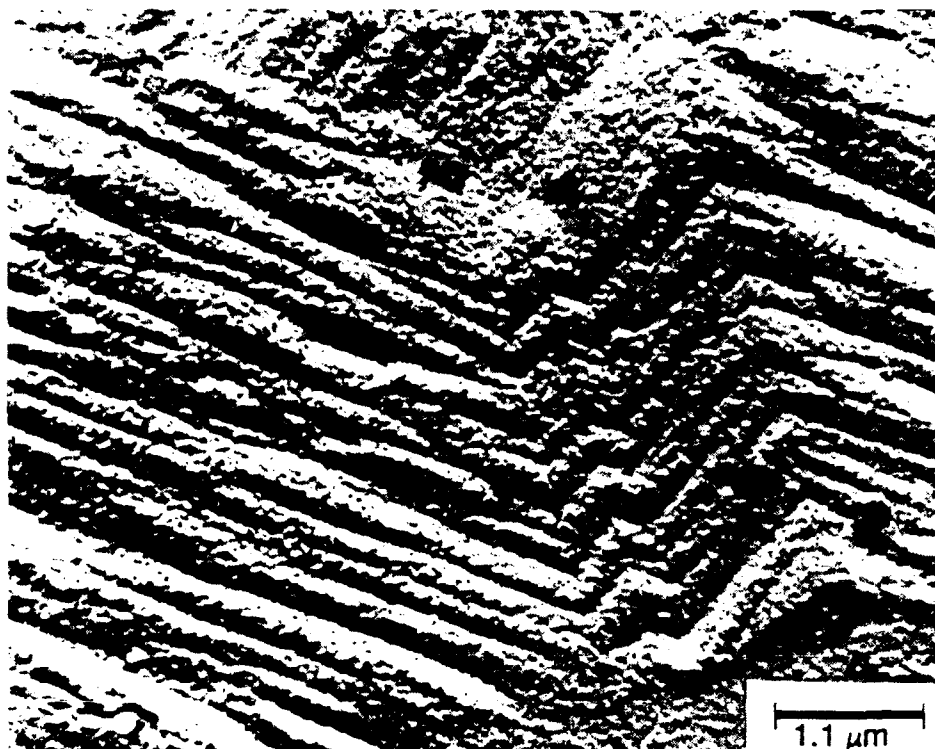


Figure 31. Photo-Micrograph of a TEM Replica Showing a Shock Formed Twin in Half-Hard OFHC Copper After Impact

The mechanical behavior of copper was significantly affected by increasing the impurity content. Increasing impurity content reduced ductility. In static tests, the percent elongation, or strain, at which failure occurred was lower in the DPTE copper than in the OFHC copper.

In dynamic tests, the data showed that the DPTE copper failed, by fracture on the periphery of the mushroom diameter, at impact velocities greater than 160 m/s. Failure of the impact specimen resulted from the large circumferential strains produced by the radial motion of the deforming material. Among DPTE copper specimens which had not cracked radially, the largest mushroom diameter measured was 20 percent less than for OFHC copper specimens.

The type of fracture found in the DPTE copper material was indicative of the microstructure. The high level of impurities

provided numerous locations within the material for the localized build up of stress. The ability of the matrix to accommodate the strain was reduced by the addition of tellurium. Numerous sites for stress concentrations, and reduced matrix ductility, produced a material that fractured at relatively low strain levels. The mode of failure was by brittle fracture as indicated by the grainy texture of the fracture surfaces.

By comparison, the OFHC copper specimens failed in a ductile manner. Close observation of the mushroom periphery in Figure 27 shows the early stages of crack growth. Note the region of deformation which surrounds each crack and is typical of ductile failure.

The inclusions, or stringers, in the DPTE copper material provide a unique way of examining the results of deformation within the specimen. During the original processing of the rod stock the oxide inclusions were broken and elongated in a direction parallel with the axis of the rod. After impact, examination of the new orientation of the stringers and grain boundaries within the material revealed certain aspects about the deformation resulting from impact. During impact, the grains compress in the direction of the specimen axis, while expanding radially. Comparison of the grain boundaries before and after impact, Figures 21 and 32, reveals that the grains at the axis now run parallel to the anvil. To accommodate the large compressive strains, the free boundary moves radially outward. In the region nearest the free surface stringers that are initially oriented axially reorient as the free surface changes shape, Figure 33. Therefore, the shortening of these stringers is less than those near the specimen axis, allowing these inclusion stringers to retain their basic shape. The radial expansion that has occurred in the material is depicted by the new alignment of the stringers. Compare Figures 21, 32, and 33.

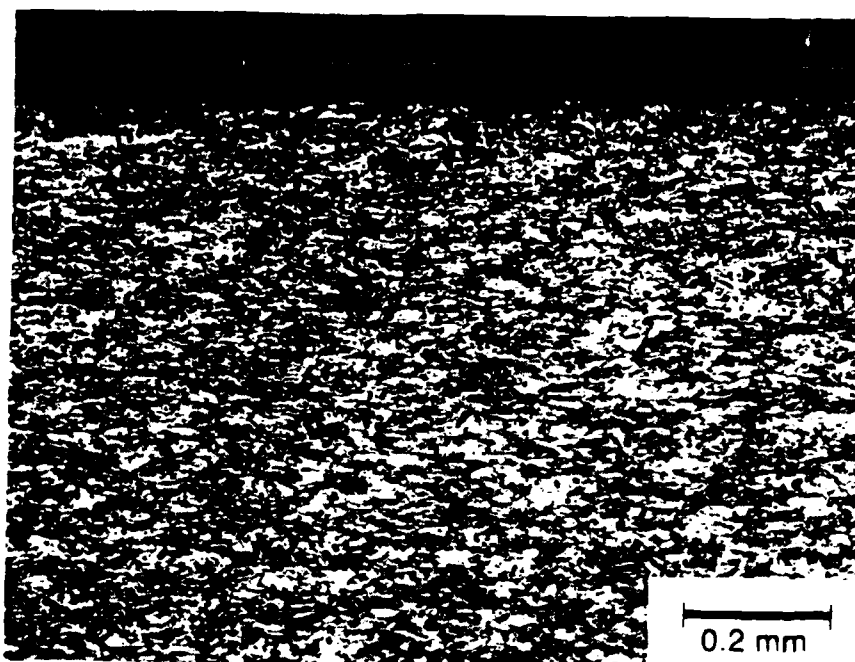


Figure 32. Optical Micrograph Showing the Microstructure of DPTE Copper After Impact

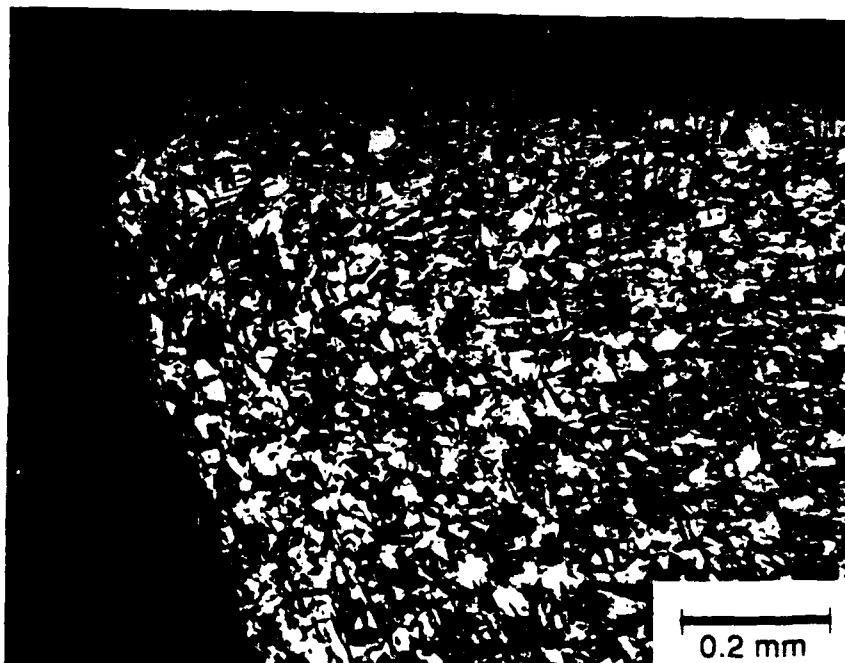


Figure 33. Optical Micrograph Showing the Microstructure of DPTE Copper, After Impact, Near the Free Boundary Surface

The two aluminum materials responded to the deformation in a manner consistent with their respective microstructures. The grains on the axis of the 6061-T6 aluminum alloy readily deformed, Figure 34. However, the 2024-T4 material, Figure 35, resisted the large amount of deformation seen in the 6061-T6 alloy. This is evidence of what effect second phase particles have on the dislocations as opposed to incoherent intermetallic particles. The finely dispersed second phase precipitates in the 2024-T4 alloy act as pegs for the dislocations, which attempt to move along the slip planes in response to the applied stress. It can be seen in Figure 35 that slip bands have been formed in certain grains. These grains have crystallographic orientation which maximizes the shear stress found on the slip plane. Once the Al_2Cu precipitate is sheared, additional

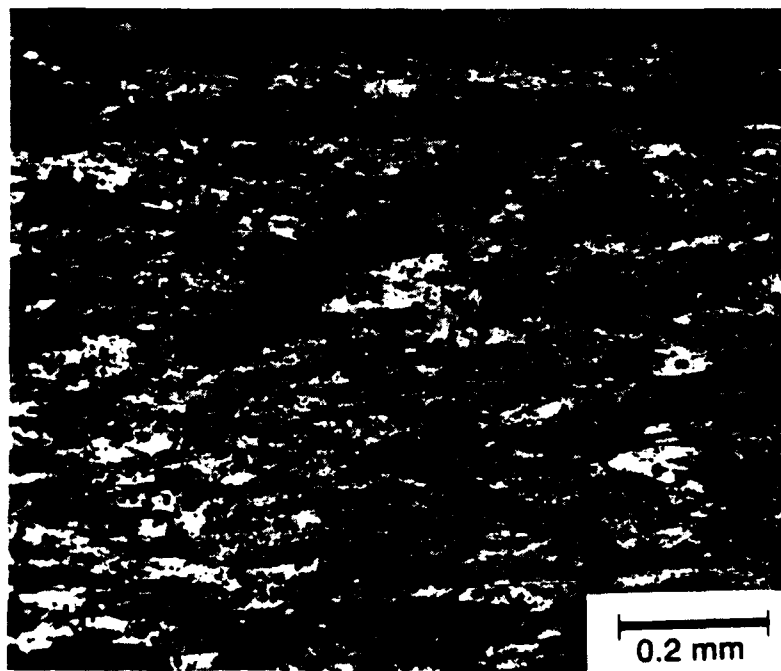


Figure 34. Optical Micrograph Showing the Microstructure in 6061-T6 Aluminum After Impact

dislocations readily move through the material. The inclusion particles of 6061-T6 aluminum being larger in size and spaced further apart than the precipitates in 2024-T4 provides little resistance to the motion of dislocations.

The energy which can be absorbed by a material is defined by its toughness and is indicated in the Taylor anvil test by the strain to failure and the extent of the plastic deformation. The 2024-T4 alloy has high strength, but relatively low toughness, compared with the 6061-T6 alloy. The geometry of the inclusion particles found in 2024-T4 are very irregular, Figure 23. This shape produces localized stress concentrations which

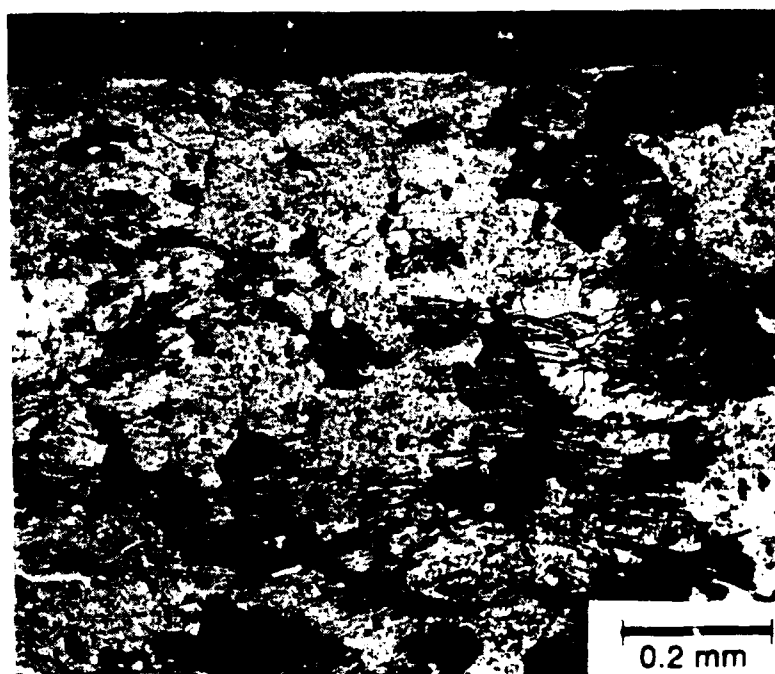


Figure 35. Optical Micrograph Showing the Microstructure in 2024-T4 Aluminum After Impact

lead to crack nucleation. Once initiated, the crack propagates through the material at the interface between the inclusion particles and the matrix. In contrast, the 6061-T6 alloy is relatively tough because of the spherically shaped particles, which do not significantly increase the local stress level, Figure 22. Similarly, the DPTE copper had low toughness, while the OFHC copper could absorb an extensive amount of energy by plastic deformation.

SECTION VI

TWO-DIMENSIONAL MODELING

1. INTRODUCTION

One-dimensional interpretations of the Taylor test have been discussed previously. In addition, the Taylor test can provide experimental information to be used with other types of computer models. These models consist of two-dimensional simulations of the impact event. The key element in such computer programs is the constitutive relationship that predicts the material response in the event.

2. CONSTITUTIVE RELATIONSHIPS

The constitutive relationship needed in the model must provide a relationship between the independent variables, i.e., strain, strain-rate, temperature, and the dependent variable, stress. Often, these terms are combined in a generic formula along with various material dependent adjustment factors. The adjustment factors will take into consideration the sensitivity of the stress level in the material under various conditions. For example, a common term used in this type of characterization is work hardening of the material. Typically, this strain dependent term has a coefficient, which dictates the amount of work hardening, and an exponent term, which governs the rate of work hardening. The coefficient and the exponent are material dependent factors within the equation. One example of such an expression, used with some success by investigators Johnson and Cook, Reference 4, is as follows:

$$\sigma = (A + B\epsilon^n)(1 + C\ln\dot{\epsilon})(1 - T^{*m}) \quad (42)$$

where A, B, C, n, m, are material parameters which must be determined in laboratory test for the material under investigation. The parameter T^* is the homologous temperature.

The first term on the right-hand side of Equation (42) is the expression given by Ludwik, Reference 16, for describing the parabolic work hardening behavior of a metal. The second and third terms contain the influence of strain rate and temperature, respectively, on the stress-strain curve.

Other investigators, Zerilli and Armstrong, Reference 5, have modified the equation proposed by Johnson and Cook. The investigation by Zerilli and Armstrong provided an enhanced material behavior description for use in multi-dimensional models. It was pointed out that Equation (42) was an improvement over previously used constitutive relationships, e.g., elastic/plastic, or, elastic/plastic with linear strain hardening. However, Equation (42) was deficient in describing certain aspects of observed material behavior. Factors known to have an affect on the material behavior, i.e., grain size, dislocation density, etc., were noticeably absent. An equation proposed by Zerilli and Armstrong for face centered cubic (fcc) material is as follows:

$$\sigma = \Delta\sigma_G + k\bar{l}^{-0.5} + C_2\epsilon^{0.5}\exp(-C_3T + C_4T\ln\dot{\epsilon}) \quad (43)$$

where k is the microstress intensity at the grain boundary and \bar{l} is the average grain size. The term $\Delta\sigma_G$ is a stress component associated with the effect of solute atoms and the original dislocation density in the material. The influence of the microstructure is incorporated into the first and second terms on the right hand side of Equation (43), as well as in the material dependent coefficients, C_2 , C_3 , C_4 . The last term combines the influences of strain, strain rate, and temperature on the material behavior.

A similar expression was constructed for body centered cubic (bcc) materials. This expression was modified slightly from Equation (43) by separating the strain hardening term from the strain rate and temperature components. As suggested by Zerilli and Armstrong, Reference 5, this modification is in agreement

with observed behavior of bcc materials. In addition, Zerilli and Armstrong suggest that a term may be necessary in the expression to account for deformation twin formation, which is known to occur in deformed bcc materials.

3. TWO-DIMENSIONAL MODELING

Once a suitable constitutive relationship is chosen, and the material parameters determined, a mesh, or grid, model of the target and projectile is constructed. In this type of model, the mass of the material within the elements is distributed at the connecting points throughout the body.

To initialize the model, a velocity is given to all of the elements in the model which describe the projectile. At some time after impact, the computer program will calculate the deformation behavior of the material for the particular impact velocity chosen. This process can be run iteratively until the projectile is brought to rest.

The major advantage of this type of modeling is the ability to generate a historical record of the deformation as it proceeds to the final ballistic geometry. This capability of multidimensional modeling provides a tool to study the details of the deformation event. One measure of success for the constitutive relationship is how well its prediction of the final geometry agrees with the experimental results.

The inherent difficulties associated with this type of modeling is the amount of testing required to suitably characterize a material and the computational resources necessary to run the model. With regard to the former, an extensive test matrix must be constructed and executed to adequately characterize the material. If the processing history of the material is altered, then the characterization is no longer valid because of changes in the microstructure of the

material. As an example, the parameters determined for pure copper tested in the annealed condition would not be equal to those found for copper tested in a half-hard condition.

In addition, the constants used to characterize the material are generally not determined under the conditions found in an impact event. Therefore, using the constitutive relationships in impact studies represents an extrapolation of the material model into a regime where little or no prior information exists. Data used to characterize a material are often obtained at strain rates several orders of magnitude below those found in the actual event. At sufficiently high rates of deformation certain physical properties, i.e., pressure, temperature, density, etc., become increasingly important in the behavior of the material. The temperature terms found in Equations (41) and (42) are attempts to account for the thermodynamic influences on the material behavior.

The requirements for computer resources are large in multidimensional models. To handle the extensive amount of data which represents the current state, or condition, of the specimen and target requires large core memory storage. In addition, thousands of calculations are necessary to accurately increment the process a small step in time. In combination, these two basic requirements of storage and computational speed eliminate the personal computer as an effective tool. Cost to the user, because of the computer resource requirements, is the primary drawback of multidimensional modeling techniques. If the factor of cost can be overcome then the use of multidimensional modeling is appropriate for the investigation of the details surrounding the deformation process.

In general, the interest in multidimensional modeling has developed simultaneously with that of one-dimensional models. In both cases, the investigators are attempting to provide materials

characterization so that predictive models in the area of target/penetrator interaction can be developed.

Multidimensional models are useful in target/penetrator interaction for studying the details of the deformation process. The assumption in multidimensional modeling is that if the final configuration predicted by the model is matched by experimental results, then the constitutive relationship is a success at modeling the process. Unfortunately, success at predicting the outcome is not a sufficient criteria for judging our knowledge of the mechanisms at work in the penetration process. The transient nature of the penetration process makes it difficult to obtain useful data to confirm the results of multidimensional models.

For one-dimensional analyses, the measure of success is the ability to predict the depth of penetration into a target material. Such analyses can be performed after the target and penetrator materials have been characterized by the Taylor test method. This provides the armor/armor penetrator designer with a straightforward technique for predicting the results of the target/penetrator interaction to a first approximation level. By using a one-dimensional technique, the effectiveness of a material as a candidate for a penetrator or armor can be estimated prior to the effort and expense of experimental verification.

SECTION VII

CONCLUSIONS

1. INTRODUCTION

This investigation has produced results in the following areas: evaluation of the experimental apparatus and procedures, further insight into the physical process resulting from impact, evaluation of the α/β model. The conclusions resulting from the analysis of these areas can be described separately, but it must be kept in mind that they represent areas of knowledge developed in parallel during the investigation. Improvements to the test apparatus and methodology resulted in further understanding of the physical process; which in turn, expands the basis for evaluation of the engineering model. Overall the results show that the investigation has been effective in improving the experimental technique and understanding of the physical process, which can be applied towards the enhancement of predictive models.

2. EXPERIMENTAL APPARATUS AND METHODOLOGY

The engineering design has succeeded in meeting the baseline goal for producing an efficient and flexible test apparatus having good repeatability. The efficiency of the design provides a cost-effective source for material characterization data. In addition, the test apparatus has designed-in flexibility by comparison with systems previously used. Experimentally the most important goal is repeatability. This factor allows the structure of experiments to focus on extracting information from each test, as opposed, to the concern that the test methodology will obscure trends in the data.

Improvements in the technologies for measuring projectile velocity and ballistic geometry have revealed certain trends in the data. With these capabilities the physical process is more

readily understood, and the possible enhancement of analytical models is likely.

3. PHYSICAL PROCESS RESULTING FROM IMPACT

During this investigation several features of the physical process were revealed, which had previously not been reported in the regime of velocities studied. By the observation of recrystallization and deformation twins in pure copper specimens it was evident that the initial pressure was significantly higher than previously thought. A model constructed on the basis of shock wave theory was in good agreement with the evidence found in the microstructure of the specimen.

The magnitude of the pressure found in materials used in a Taylor test was significant in that the basic analysis of the process, including the current model, uses traditional plastic and elastic wave motion as its foundation. In actuality, there is sufficient evidence to indicate that the deformation in the specimen is initiated as a shock process, though it is relatively short lived by comparison to the total length of time of the event. Evidence which supports the conclusion that the deformation process cannot be described strictly as a plastic and elastic wave process is found in the results from the high speed photography. Data shown in Figure 20 indicates that to a reasonable approximation the rigid rod velocity did not change until the event was half over. Plastic/elastic wave analysis suggests that the undeformed end of the specimen would have a change in velocity within the first 30 μ s of the event. This suggests that the shock process is altering the time frame of events, such as the completion of mushroom growth and the change in velocity of the rigid rod, relative to theory on plastic and elastic wave motion in materials.

The questions that arise from these conclusions are: when does the shock wave attenuate into plastic and elastic waves; what is the shape of the wave front, in the specimen, which is considered planar for simplicity in the analysis? The first of these questions could be addressed by examining the rate at which a shock wave is attenuated as it moves through a material. In addition to attenuation by the motion of the shock front, the free boundary of the material produces a release wave which will have some influence on the process. The second question could be addressed by a careful examination of the microstructure resulting from impact. Since shock waves are produced by pressure levels that have certain effects on the microstructure, it may be possible to determine the shape and extent of the shock process by a thorough microstructural examination.

4. α/β MODEL

The Taylor test was developed as a simple method of obtaining data to characterize the strength of a material under impact conditions. The α/β model, Reference 8, was successful as an analysis which accounted for mass transfer from the rigid portion of the rod. This analysis was constructed based on the assumptions that the constitutive relationship was perfectly plastic, that radial inertia effects could be ignored, and that the process is described by plastic and elastic wave motion. The assumption, regarding the constitutive relationship and the effects of inertia, characterize the analysis as a first approximation suitable as an engineering model.

The term engineering model, as used here, is defined as an analysis which is based on the assumption that an interrelationship exists among the test variables, i.e., density, velocity, geometry, etc., that will reveal the strength of a material on impact. The fact that the analysis was developed as an engineering model must be considered when evaluating its success.

A recently proposed model of high strain rate behavior in pure copper provides a measure of success for the current investigation. A stress/strain curve, Figure 36, generated by a model proposed by Follansbee and Kocks, Reference 17, shows the predicted behavior of pure copper under high strain rate conditions. Given the level of approximation found in the α/β model, it has provided data which is in good agreement with the strength of pure copper given by the model of Follansbee and Kocks. At the level of approximation for which it was designed, the α/β model is successful at predicting the strength of a material under impact conditions.

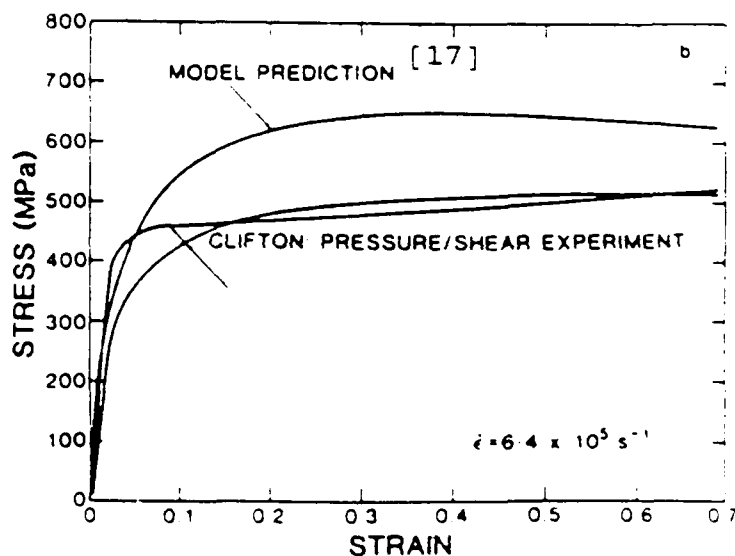


Figure 36. Stress/Strain Response of Pure Copper Under High Strain-Rate Conditions

The information obtained from the Taylor test and the analysis developed by investigators Jones, Gillis, and Foster, Reference 8, will provide the armor/armor penetrator designer with a relatively simple, yet effective, tool for the estimation of material strength at high rates of deformation. While the model is not intended to describe the detailed behavior of the physical process, it does provide a first approximation approach

to determining the material property necessary in the development of terminal ballistic models.

REFERENCES

1. G.I. Taylor, Proc. R. Soc. London, Series A, 194, 298 (1948).
2. A. Tate, J. Mech. Phys. Solids, 15, 387 (1967).
3. S.E. Jones, P.P. Gillis, and J.C. Foster, Jr., J. Mech. Phys. Solids, 35, 121 (1987).
4. G.R. Johnson and W. Cook, Proceedings of the Seventh International Symposium on Ballistics, The Hague, The Netherlands, pp. 541 (1983).
5. F.J. Zerilli and R.W. Armstrong, J. Appl. Phys. 61, 1825 (1987).
6. N. Cristescu, Dynamic Plasticity, (John Wiley and Sons, Inc. New York, 1967).
7. J.B. Hawkyard, Int. J. Mech. Sci. 11, 313 (1969).
8. S.E. Jones, P.P. Gillis, and J.C. Foster, Jr. J. Appl. Phys. 61, 499 (1987).
9. A.C. Whiffin, Proc. R. Soc. London, Series A, 194, 300 (1948).
10. M.L. Wilkins and M.W. Guinan, J. Appl. Phys. 44, 1200 (1973).
11. H. Ahlborn and G. Wassermann, Z. Metallk. 54, 1 (1962).
12. G. Wassermann, Z. Metallk. 54 (1963).
13. T.H. Blewitt, R.R. Coltman, and J.K. Redman, J. Appl. Physics, 28, 651 (1957).
14. R.J. De Angelis, and J.B. Cohen, Proceedings of the AIME - IMD Conference on Deformation Twinning (Gordon and Breach Publishers, New York, 1964) p. 430.
15. D.C. Brillhart, R.J. De Angelis, A.G. Preban, J.B. Cohen, and P. Gordon, Trans. AIME, 239, 836 (1967).
16. P. Ludwik, Elemente der Technologischen Mechanick, (Springer, Berlin, 1909), p 32.
17. P.S. Follansbee and U.F. Kocks, Acta Metall. 36, 81 (1988).

BIBLIOGRAPHY

- S.E. Axter, W.B. Jones, and D.H. Polonis, *Metallography*, 8, 425 (1975).
- J.D. Campbell, Dynamic Plasticity of Metals, (Udine, New York, 1970).
- W.E. Carrington and M.L.V. Gayler, *Proc. R. Soc. London, Series A*, 194, 323 (1948).
- R.J. Clifton, *J. Appl. Mech.* 50, 941 (1983).
- P. Gordon, R. Karpp, S. Sanday, M. Schwartz, *J. Appl. Phys.* 48, 172 (1977).
- H.A. Grebe, H.R. Pak, and M.A. Meyers, *Metal. Trans. A*, 10A, 569 (1979).
- J.B. Hawkyard, D. Eaton, and W. Johnson, *Int. J. Mech. Sci.* 10, 929 (1968).
- I.M. Hutchings and T.J. O'Brian, *Int. J. Mech. Sci.* 23, 255 (1981).
- W.B. Jones and H.I. Dawson, Metallurgical Effects at High Strain Rates, (Plenum, London, 1973) p. 443.
- E.H. Lee and S.J. Tupper, *J. Appl. Mech.* 21, 63 (1954).
- G. Regazzoni, U.F. Kocks, and P.S. Follansbee, *Acta Metall.* 35, 2865 (1987).
- J.S. Rhinehart and J. Pearson, Behavior of Metals Under Impulsive Loads, (ASM, Cleveland, 1954).
- A.K. Sengupta, G.J. Wigglesworth, S.K. Ghosh, W. Johnson, and S.R. Reid, *J. Mech. Eng. Sci.* 24, 31 (1982).
- C.S. Smith, *Trans. AIME*, 214, 574 (1958).
- T. von Karmen and P. Duwez, *J. Appl. Phys.* 21, 987, (1958).

APPENDIX A
TEST PROCEDURES

APPENDIX A
TEST PROCEDURES

- 1) Remove target housing cover. Clean debris, if any, off of the plexiglass windows.
- 2) Remove and clean pressure transducers, if necessary.
- 3) Prior to mounting the pressure transducers in the muzzle, apply a thin layer of silicon grease over the piezo-crystal surface to act as a damper on the pressure wave.
- 4) Check the voltage output from the infrared detector circuit. A low voltage state indicates debris is covering the detector lens and must be removed.
- 5) Clean the infrared detector lens, if necessary.
- 6) Rotate the target, if necessary, and position the fiducial (magnet) on the target face one-half inch above the point of impact.
- 7) Bore sight the high speed camera, or the framing camera, if necessary. The camera lens should be as near parallel to the target face as possible.
- 8) If high speed photography is to be used, load the camera with film.
- 9) Set the desired standoff distance between the muzzle and the anvil. Tighten the bolts on the v-block mounts to secure the launch tube.
- 10) Replace the target housing cover.
- 11) Weigh specimen. (grains)
- 12) Measure specimen diameter. (inches)
- 13) Weigh propellant charge. (grains)
- 14) Load the measured quantity of propellant into a cartridge.
- 15) Insert a ball of cotton into the cartridge case and pack against the propellant.
- 16) Obtain the safe/arm panel keys.
- 17) Insert a specimen, followed by an obturator, into the breech end of the launch tube.

- 18) Position the specimen and obturator at the correct depth in the launch tube using depth measurement gauge.
- 19) Insert the cartridge case behind the specimen and obturator. Screw the breech cap on the barrel until the scribed marks are aligned.
- 20) Attach the firing solenoid to the breech.
- 21) Remove shunting connector from the firing line and connect the firing line to the firing solenoid.
- 22) Insert the firing pin to the prescribed depth into the firing solenoid.
- 23) Remove shorting plug from firing line and connect firing line to firing power supply output panel.
- 24) Arm the firing power supply circuit.
- 25) Arm the firing signal control panel.
- 26) After arming the firing signal control panel, monitor the charge level of the firing power supply until the predetermined voltage level is reached. Once the appropriate energy level is reached the firing countdown can begin.
- 27) At t minus 20 seconds, the multitrack signal recorder is turned on.
- 28) At t minus 5 seconds, when using the high speed movie camera, the photographic light is turned on.
- 29) At t minus 3 seconds, the high speed camera is turned on.
- 30) At t equal to 0, the firing signal is sent to the high speed movie camera and to the firing solenoid.
- 31) Disarm the control panel.
- 32) Disarm the firing circuit.
- 33) Remove the firing circuit wire connected to the firing solenoid.
- 34) Unscrew the breech end cap and extract the spent cartridge case.
- 35) Clean debris from the launch tube bore with a gun cleaning rod tool.

- 36) Remove target cover and retrieve the impact specimen and obturator. Discard obturator.
- 37) Remove high speed movie film, or framing camera film, if necessary.
- 38) Measured from the oscilloscope, record the duration of time between the leading edge of the pressure transducer signals.
- 39) Obtain a strip chart output of the transducer signals from the multichannel recorder.
- 40) Using the strip chart output, digitize the reference signal (frequency = 100 khz). Digitize the leading edge of the pressure transducer signals.
- 41) Obtain a print out of the digitized data converted to specimen velocity.
- 42) Measure the final diameter of the mushroomed portion of the specimen.
- 43) Measure the final length of the specimen.
- 44) Measure the undeformed length of the specimen.

APPENDIX B

DATA FILES

MATERIAL: OFHC COPPER
 YIELD STRENGTH: Mpa 304 Mpa
 ULTIMATE STRENGTH: 304 Mpa
 DENSITY: 8.94 GRAMS/CUBIC CENTIMETER
 FILE WAS UPDATED ON OCTOBER 15, 1988

SHOT NUMBER	L/D	VELOCITY ft/s	VELOCITY m/s	LF INCHES	IF INCHES	FINAL DIAMETER INCHES	YIELD STRENGTH MPa	TAYLOR MPa	PROPELLANT CHARGE Grains	MASS GRAMS	SEE REMARKS	ENERGY JOULES	ALPHA	BETA	LAMBDA m/s
25	1.5	260.6	79.43	0.408	0.201	0.338	305.9	207.69	1	4.61 b		14.55	0.1842	3.0033	238.55
26	1.5	447.8	136.49	0.352	0.144	0.46	334.1	228.45	1.5	4.61 b		42.97	0.4984	1.3645	186.24
128	1.5	552	168.25	0.359	0.149	0.451	558.7	379.09	1.6	4.61		65.30	0.453	1.4766	248.44
55	1.5	626.1	190.84	0.349	0.162	0.471	582.4	454.86	2	4.61		84.01	0.559	1.1449	218.49
56	1.5	839.7	255.94	0.319	0.134	0.535	754.2	583.71	2.5	4.61 c		151.11	0.7765	0.9044	231.47
127	2	527	160.63	0.488	0.215	0.459	550.6	386.74	1.5	6.15		79.36	0.4189	1.5317	246.04
147	2	556	169.47	0.475	0.217	0.4778	516.1	387.19	1.9	6.15		88.33	0.4977	1.2826	217.36
64	2	705.9	215.16	0.427	0.184	0.551	532.5	421.45	2.3	6.15		142.38	0.7771	0.8922	191.96
59	2	769.8	234.64	0.407	0.161	0.58	560.6	425.98	2.7	6.15 a		169.33	0.8779	0.8334	195.54
58	2	817.4	249.14	0.366	0.14	0.651	465.4	375.22	3	6.15 a		190.92	1.1923	0.643	160.20
129	3	531	161.85	0.72	0.307	0.487	517.6	359.06	2	9.23		120.85	0.4524	1.4564	235.72
63	3	656.3	200.04	0.665	0.245	0.56	583.1	383.60	2.4	9.23		184.62	0.6135	1.1863	237.31
61	3	743	226.47	0.613	0.201	0.613	583.3	372.88	3	9.23 a		236.62	0.7863	0.9877	223.68
60	3	775.7	236.43	0.582	0.18	0.672	553.5	351.92	3.5	9.23 a		257.90	0.9028	0.8861	209.50
62	3	825.4	251.58	0.771	0.243	0.486	533.2	299.28	4.2	9.23 a		292.01	*****	*****	ERR
5	3.33	554	168.86	0.714	0.199	*****	564	306.53	2	10.24		146.02	0.4763	1.5892	268.35
135	3.33	651	198.42	0.676	0.172	*****	662.8	156.76	2.6	10.24 a		201.63	0.6241	1.2835	254.68
2	3.33	655.7	199.86	0.641	0.172	*****	521.5	299.74	3	10.24 b		204.55	0.5388	1.7947	358.68
134	3.33	741	225.86	0.641	0.172	*****	521.5	299.74	3	10.24 a		261.23	0.8745	0.7082	205.12
1	3.33	891	271.58	0.956	0.405	0.5	562.1	389.41	5	10.24 a		377.70	*****	*****	ERR
65	4	558.8	170.32	0.931	0.365	0.52	540.5	358.49	2.5	12.30		178.45	0.4613	1.4362	244.62
126	4	575	175.26	0.856	0.328	*****	565.5	398.12	2.5	12.30		188.95	0.508	1.3697	240.05
136	4	700	213.36	0.785	0.248	0.66	523.4	358.45	3	12.30 a		280.03	0.7197	1.0097	215.43
53	4	769.8	234.64	0.796	0.258	0.663	577.4	373.81	3.7	12.30 a		338.66	0.9402	0.8118	190.48
54	4	769.9	234.67	1.106	0.325	0.521	528.1	289.90	3.7	12.30 a		338.74	0.8525	0.9208	216.08
16	5	598	182.27	1.079	0.408	0.58	516.5	356.43	3	15.38		255.46	0.5624	1.3929	253.88
133	5	656	199.95	1.006	0.243	0.613	579.4	297.95	3.6	15.38		307.41	0.6921	1.0519	210.33
36	5	716	218.24	1.01	0.353	*****	518.5	353.57	4	15.38 d		366.22	0.7348	1.1404	248.88
132	5	725	220.98	1.01	0.353	*****	518.5	353.57	4	15.38 a		375.48	0.842	0.9082	200.69
15	5	725.8	221.22	*****	*****	*****	*****	*****	4	15.38 a		376.31	*****	*****	ERR

Continues on the following page

MATERIAL: OFHC COPPER (Cont.)
YIELD STRENGTH: 304 Mpa
ULTIMATE STRENGTH: 304 Mpa
DENSITY: 8.94 GRAHNS/CUBIC CENTIMETER
FILE WAS UPDATED ON OCTOBER 15, 1988

SHOT NUMBER	L/D	VELOCITY ft/s	VELOCITY m/s	Lf INCHES	lf INCHES	IF INCHES	FINAL DIAMETER INCHES	YIELD STRENGTH MPa	TAYLOR MPa	PROPELLANT CHARGE Grains	MASS GRAMS	SEE REMARKS	ENERGY JOULES	ALPHA	BETA	LAHBDA m/s
73	7.5	500.6	152.58	1.862	0.872	0.463	0.463	534.6	390.36	3	23.07		268.53	0.3893	1.5733	240.06
72	7.5	511.9	156.03	1.861	0.842	0.469	0.469	567.9	401.18	3	23.07		280.79	0.3833	1.6327	254.75
146	7.5	591	180.14	1.685	0.674	0.5544	0.5544	481.2	336.01	4.5	23.07		374.27	0.604	1.1598	208.92
57	7.5	616.8	188.00	1.65	0.631	0.568	0.568	490.1	335.69	5	23.07		407.66	0.6447	1.1162	209.85
145	7.5	620	188.98	1.64	0.642	0.58	0.58	477.8	335.92	4.5	23.07		411.90	0.6689	1.0684	201.90
74	10	402.6	122.71	2.615	1.281	0.422	0.422	495.6	353.57	3	30.76		231.57	0.2716	2.1097	258.89
75	10	415.7	126.71	2.624	1.312	0.415	0.415	538.5	389.97	3	30.76		246.89	0.2665	2.1112	267.50
21	10	513.1	156.39	2.451	1.103	0.491	0.491	530.1	377.98	4	30.76		376.14	0.4125	1.5329	239.73
23	10	544.7	166.02	2.384	1.066	0.514	0.514	511.7	374.28	4.5	30.76		423.90	0.4816	1.3386	222.24
144	10	517	157.58	2.403	0.995	0.472	0.472	501.7	338.16	5	30.76		381.88	0.4426	1.51	237.95
143	10	552	168.25	2.313	0.975	0.525	0.525	465.7	332.22	5	30.76		435.33	0.5437	1.2415	208.88
139	10	557	169.77	2.305	0.971	0.529	0.529	466.3	333.81	5	30.76		443.26	0.5526	1.2239	207.79
141	10	579	176.48	2.311	0.966	0.512	0.512	512.5	363.08	5	30.76		478.96	0.5435	1.2476	220.18
142	10	579	176.48	2.295	0.956	0.524	0.524	496.8	353.34	5	30.76		478.96	0.5606	1.2154	214.49
140	10	604	184.10	2.278	0.929	0.531	0.531	528.2	371.12	5	30.76		521.22	0.5736	1.2035	221.56
130	10	617	188.06	2.272	0.926	*****	*****	544.8	383.58	5	30.76 d		543.89	0.5804	1.1912	224.02
131	10	624.2	190.26	2.192	0.871	*****	*****	484.7	345.11	5	30.76 d		556.66	0.6677	1.0629	202.22

NOTES:

- EXCESSIVE DEFORMATION
- OBLIQUE IMPACT
- A FAILED SECTION OF THE OBTURATOR AFFECTED THE SPECIMEN DIMENSIONS
- ELLIPSOIDAL MUSHROOM GEOMETRY

MATERIAL: DPTE COPPER
YIELD STRENGTH: Mpa
ULTIMATE STRENGTH: 300 Mpa
DENSITY: 8.94 GRAMS/CUBIC CENTIMETER
FILE WAS UPDATED ON DECEMBER 16, 1988

SHOT NUMBER	L/D	VELOCITY ft/s	VELOCITY m/s	Lf INCHES	lf INCHES	FINAL DIAMETER INCHES	YIELD STRENGTH MPa	TAYLOR CHARGE MPa	PROPELLANT CHARGE GRAINS	REMARKS GRAMS	ENERGY Joules	ALPHA	BETA	LAMBDA m/s
138	1.5	434	132.28	0.389	0.195	0.4	530.4	391.01	1.4	4.61	40.37	0.2949	1.9213	254.1557
79	1.5	455.5	138.84	0.381	0.179	0.403	516.3	367.08	1.5	4.61	44.46	0.3338	1.8041	250.4747
137	1.5	583	177.70	0.352	0.15	*****	554.4	393.30	1.5	4.61 a	72.84	0.5092	1.3092	232.6427
80	1.5	672.2	204.89	0.323	0.134	*****	511	385.41	2	4.61 a	96.83	0.7345	0.9561	195.8920
78	1.5	786.3	239.60	*****	*****	*****	*****	*****	2.5	4.61 a	132.50	*****	*****	ERR
118	2	454	138.38	0.505	0.236	0.426	493.2	351.47	1.3	6.15	58.90	0.3471	1.7476	241.8314
108	2	548	167.03	0.469	0.228	*****	450.6	366.00	1.5	6.15 a	85.81	0.5536	1.12	187.0740
107	2	563	171.60	0.461	0.214	*****	449.7	354.55	1.8	6.15 a	90.57	0.5854	1.0989	188.5738
90	2	658.7	200.77	0.432	0.21	*****	446.7	398.43	2	6.15 a	123.98	0.8068	0.8057	161.7618
89	2	714.9	236.80	*****	*****	*****	*****	*****	2.5	6.15 a	172.47	*****	*****	ERR
97	3	446	135.94	0.756	0.331	0.442	485.6	326.31	1.5	9.23	85.26	0.3402	1.8581	252.5916
95	3	536.1	163.40	0.719	0.293	*****	535.8	356.66	2	9.23 a	123.18	0.4455	1.5139	247.3762
96	3	545.3	166.21	0.714	0.283	*****	541.3	354.05	1.8	9.23 a	127.45	0.4462	1.8581	308.8300
94	3	732	223.11	*****	*****	*****	*****	*****	3	9.23 a	229.66	*****	*****	ERR
109	4	462	140.82	0.997	0.439	0.449	482.9	330.44	2.1	12.30	121.98	0.3671	1.7275	243.2624
111	4	521	158.80	0.951	0.389	*****	483.9	325.91	2.2	12.30 a	155.12	0.3659	1.4505	230.3405
110	4	543	165.51	0.928	0.369	*****	471.3	317.21	2.3	12.30 a	168.50	0.3497	1.3326	220.5538
98	4	586.4	178.73	0.916	0.352	*****	525.7	347.65	2.5	12.30 a	196.51	0.3432	1.3009	232.5159
100	5	498.3	151.88	1.235	0.521	0.454	541.9	360.23	2.3	15.38	177.38	0.3806	1.715	260.4773
99	5	515.2	157.03	1.203	0.487	*****	507.1	334.20	2.5	15.38 a	189.61	0.3477	1.5535	243.9507
105	7.5	471	143.56	1.837	0.784	0.46	457.4	310.17	3.1	23.07	237.71	0.4078	1.6175	232.2095
93	7.5	506.7	154.44	1.827	0.78	0.457	512.5	349.75	3.1	23.07	275.11	0.3661	1.5702	242.5050
92	7.5	546.9	166.70	1.757	0.704	*****	499.5	335.23	3.5	23.07 a	320.49	0.3474	1.3815	230.2893
88	7.5	573.7	174.86	1.729	0.669	*****	517.3	341.96	4	23.07 a	352.68	0.3286	1.4853	259.7251
86	10	492.5	150.11	2.436	1.051	0.457	481.5	331.86	4	30.76	346.54	0.4186	1.5529	233.1120
87	10	516.8	157.52	2.385	0.972	0.474	487.4	324.52	4.5	30.76	381.58	0.4051	1.4853	233.9654
91	10	573.1	174.68	2.298	0.881	*****	510.9	336.00	5	30.76 a	469.25	0.339	1.3279	231.0853

NOTES:
a) EXCESSIVE DEFORMATION
b) OBLIQUE IMPACT

MATERIAL: 6061 T6 ALUMINUM
YIELD STRENGTH: 315 Mpa
ULTIMATE STRENGTH: 340 Mpa
DENSITY: 2.71 GRAMS/CUBIC CENTIMETER
FILE WAS UPDATED ON DECEMBER 16, 1988

SHOT NUMBER	L/D	VELOCITY		LF INCHES	IF INCHES	FINAL DIAMETER INCHES	YIELD STRENGTH MPa	TAYLOR MPa	PROPELLANT CHARGE Grains	MASS GRAMS	REMARKS	ENERGY JOULES	ALPHA	BETA	LAMBDA
		ft/s	m/s												
24	1.5	396.4	120.82	0.435	0.252	0.252	677.3	475.24	1	1.48	b	10.81	0.0616	7.1382	862.45
28	1.5	765	227.08	0.401	0.204	0.388	653.4	467.91	2	1.48		38.18	0.2257	2.422	549.37
69	1.5	770.4	234.82	0.391	0.174	0.389	592.8	388.19	2	1.48		40.83	0.2729	2.0542	482.36
66	1.5	785.3	239.36	*****	*****	*****	*****	*****	2	1.48	b	42.42	*****	*****	ERR
76	1.5	1111	338.63	0.326	0.109	0.502	516.4	318	2.5	1.48		84.91	0.6351	1.1931	404.02
50	2	694.1	211.56	0.536	0.256	0.383	600.2	403.9	1.8	1.97		44.19	0.2133	2.6885	568.78
51	2	733.7	223.63	0.525	0.246	0.404	556.8	378.6	1.8	1.97		49.37	0.2736	2.2969	513.65
114	2	786	239.57	0.509	0.224	0.419	515.7	344.19	2.3	1.97		56.66	0.3183	1.9689	471.69
112	2	864	263.35	0.494	0.222	0.449	504.6	355.7	2.3	1.97		68.47	0.3931	1.6027	422.06
113	2	1075	327.66	0.449	0.188	0.517	494.2	360.96	2.5	1.97	b	105.99	0.6213	1.1052	362.12
48	3	560.4	170.81	0.826	0.396	*****	815.6	346.12	1.9	2.96		43.21	*****	*****	ERR
49	3	812.5	247.65	0.765	0.325	0.437	568.4	366.74	1.9	2.96		90.82	0.3086	2.0702	512.68
119	3	914	278.59	0.727	0.293	0.482	532.6	346.99	2.5	2.96		114.93	0.4167	1.6184	450.86
52	4	741.6	226.04	1.045	0.511	0.425	534.1	380.44	2.1	3.95		100.88	0.2736	2.0988	474.41
47	4	758.6	231.22	1.019	0.466	0.449	474.6	327.77	2.1	3.95		105.56	0.3221	1.8987	439.01
120	4	926	282.24	0.97	0.408	0.493	537.5	363.61	2.7	3.95		157.29	0.4239	1.557	439.45
17	5	557	169.77	1.369	0.722	0.381	467.3	334.77	1.5	4.94		71.14	0.1759	2.9482	500.52
67	5	801.1	244.18	1.287	0.595	0.44	568.9	391.77	2.3	4.94		147.15	0.2997	2.0128	491.47
18	5	968.7	295.26	1.179	0.482	0.53	512.9	348.25	3	4.94		215.16	0.4862	1.396	412.18
44	7.5	115.9	35.33	*****	*****	*****	*****	*****	3	7.40	c	4.62	*****	*****	ERR
43	7.5	773	235.61	1.948	0.95	0.444	553.5	396.32	3	7.40		205.51	0.2868	2.0143	474.59
45	7.5	795.1	242.35	1.908	0.865	0.467	518.6	355.79	3	7.40		217.43	0.3239	1.9003	460.53
46	7.5	873.7	251.06	1.908	0.883	0.441	550.6	385.15	2.8	7.40		233.36	0.3274	1.8557	465.89
121	7.5	904	275.54	1.828	0.786	0.49	521.6	358.12	3.4	7.40		281.07	0.4163	1.563	430.66
71	10	770.1	234.73	2.618	1.318	0.429	577.3	421.78	3.2	9.87		271.97	0.2729	2.0542	482.17
68	10	838.9	255.70	2.51	1.13	0.467	527.5	365.43	3.7	9.87		322.73	0.3545	1.7582	449.56
19	10	889.4	271.09	2.482	1.112	0.502	552.2	385.94	4	9.87		362.76	0.3806	1.6534	448.21

Notes:

- a) EXCESSIVE DEFORMATION
- b) OBLIQUE IMPACT
- c) PRIMER FAILURE

MATERIAL: 2024 T4 ALUMINUM
YIELD STRENGTH: 400 Mpa
ULTIMATE STRENGTH: 500 Mpa
DENSITY: 2.78 GRAMS/CUBIC CENTIMETER
FILE WAS UPDATED DECEMBER 16, 1988

SHOT NUMBER	L/D	VELOCITY ft/s	VELOCITY m/s	I.F. INCHES	I.F. INCHES	FINAL DIAMETER INCHES	YIELD STRENGTH MPa	TAYLOR MPa	PROPELLANT CHARGE GRAINS	MASS GRAMS	SEE REMARKS	ENERGY JOULES	ALPHA	BETA	LANBDA m/s
27	1.5	533.7	162.67	0.428	0.216	0.337	852.9	548.37	1.5	1.48		19.59	0.0888	5.858	952.93
81	1.5	653.4	199.16	0.417	0.184	0.339	853.5	511.21	1.8	1.48		29.37	0.1329	4.4475	885.74
83	1.5	929.4	283.28	0.39	0.151	0.393	896.6	523.7	2.3	1.48		59.42	0.256	2.5957	735.31
70	1.5	1197	364.85	0.365	0.13	0.432	987.3	577.12	2.5	1.48 a		98.56	0.3856	1.844	672.77
77	2	726.1	221.32	0.557	0.276	0.353	1033.2	679.64	1.8	1.97		48.36	0.1356	3.9834	881.58
115	2	819	249.63	0.531	0.19	0.382	856.9	460.48	2.5	1.97		61.52	0.208	3.2856	820.18
117	2	850	259.08	0.522	0.198	0.389	779.7	446.21	2.5	1.97 b		66.27	0.2462	2.7214	705.06
82	2	949.5	289.41	0.514	0.18	0.404	888.8	485.84	2.3	1.97		82.69	0.2695	2.5974	751.70
116	2	1088	331.62	0.48	0.19	0.392	847.7	464.93	2.7	1.97 a		108.57	0.436	1.5674	519.78
84	3	873.1	266.12	0.784	0.282	0.392	847.7	464.93	2.5	2.96		104.87	0.2389	2.8739	764.80
102	3	974.6	297.06	0.759	0.263	0.429	841.4	463.39	2.5	2.96		130.68	0.2999	2.3598	700.99
101	3	1190	362.71	0.759	0.263	0.429	841.4	463.39	2.7	2.96 a		194.82	0.2999	2.3598	700.99
85	4	814.1	248.14	1.059	0.425	0.385	791.3	466.24	2.5	3.95		121.57	0.2225	2.9022	720.14
104	4	925.4	282.06	1.03	0.387	0.409	834.4	480.79	2.5	3.95		157.09	0.2727	2.4845	700.78
103	4	1044	318.21	0.759	0.263	0.429	841.4	463.39	2.7	3.95 a		199.93	0.2727	2.4845	700.78
7	5	640.7	195.29	1.387	0.647	0.352	779	489.57	1.5	4.94		94.12	0.14	4.061	793.05
8	5	928.2	282.92	1.255	0.464	0.444	706.2	412.5	3	4.94 b		197.55	0.3242	2.1307	602.80
106	5	947	288.65	1.254	0.453	0.444	738	423.51	3	4.94 a		205.63	0.3229	2.1619	624.02
42	7.5	629	191.72	2.069	0.983	0.355	690.7	444.32	2.5	7.40		136.08	0.1522	3.6998	709.32
41	7.5	874.1	266.43	1.937	0.742	0.411	755.8	440.84	3.5	7.40		262.79	0.2686	2.495	664.73
122	7.5	885	269.75	1.924	0.71	0.404	747.3	426.16	3.7	7.40		269.38	0.2785	2.4577	662.95
123	7.5	953	290.47	1.881	0.673	0.442	750.2	427.24	3.9	7.40 a		312.37	0.3217	2.1789	632.91
20	10	820.5	250.09	2.651	1.113	0.405	799	485.7	4	9.87 c		308.73	0.2239	2.8097	702.67
22	10	820.7	250.15	2.622	1.052	0.405	738.9	440.05	4	9.87		308.88	0.2422	2.6808	670.60
124	10	887	270.36	2.561	0.943	0.413	742	423.19	4.4	9.87		360.80	0.2817	2.4339	658.02
125	10	950	289.56	2.507	0.885	0.433	747.4	421.35	4.6	9.87		413.87	0.3208	2.1973	636.25

NOTES:

- a) EXCESSIVE DEFORMATION
- b) OBLIQUE IMPACT
- c) SPECIMEN IMPACTED ON A PIECE OF ORBITATOR

APPENDIX C
TENSILE SPECIMEN

APPENDIX C
TENSILE SPECIMEN

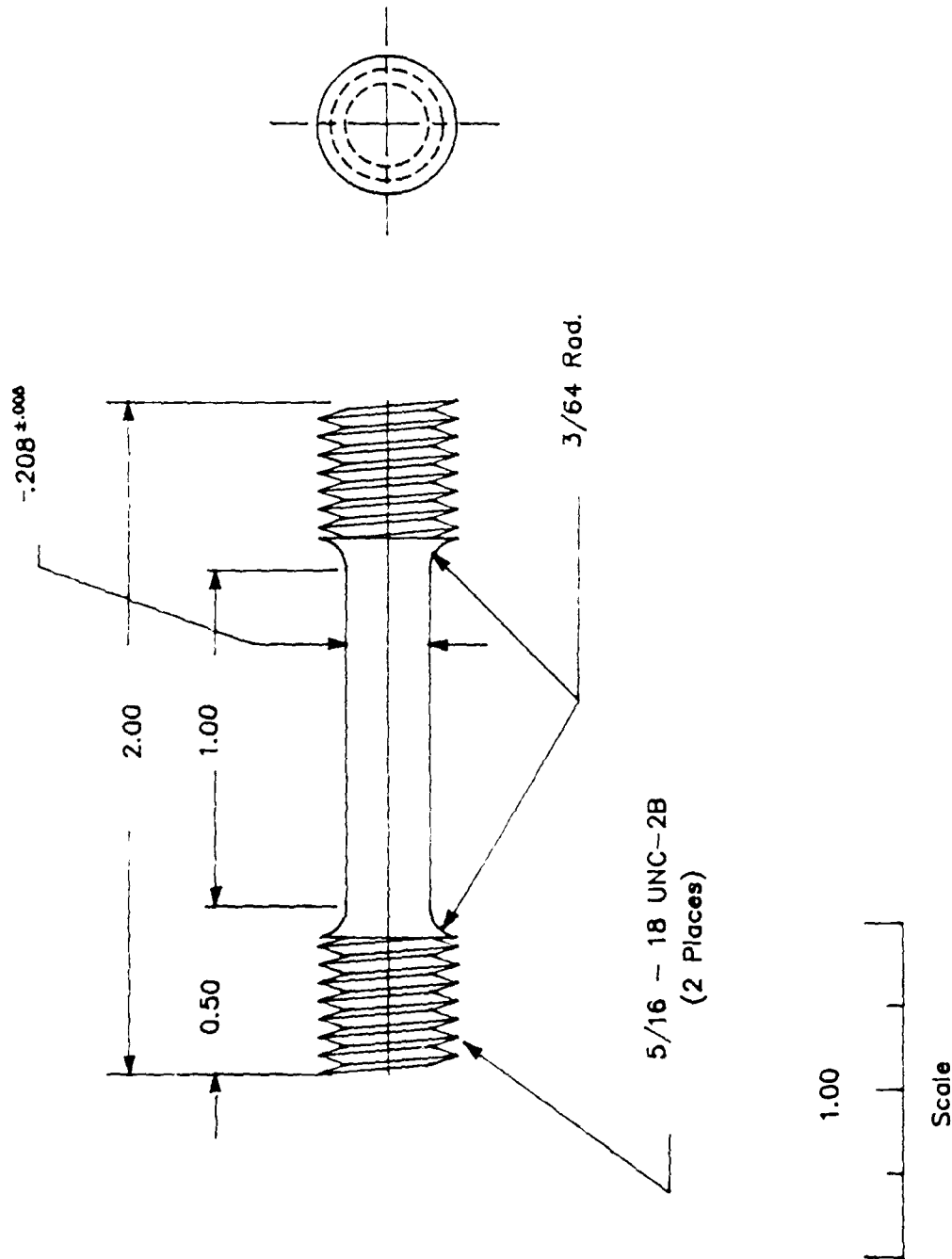


Figure C-1. Dimensions of the Tensile Specimen

APPENDIX D
LOAD VERSUS TIME CHARTS

APPENDIX D
LOAD VERSUS TIME CHARTS

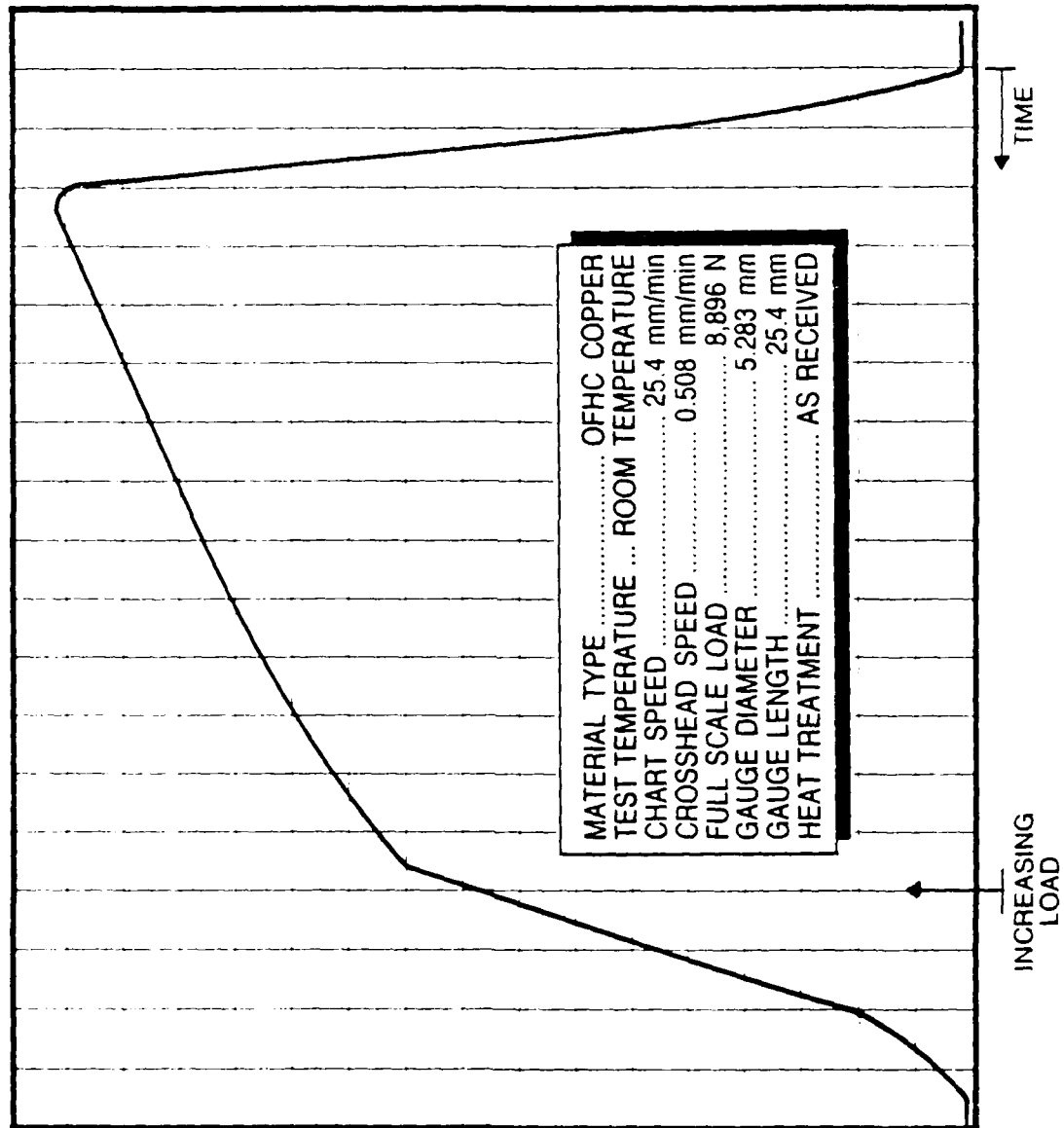


Figure D-1. Load Response of OFHC Copper

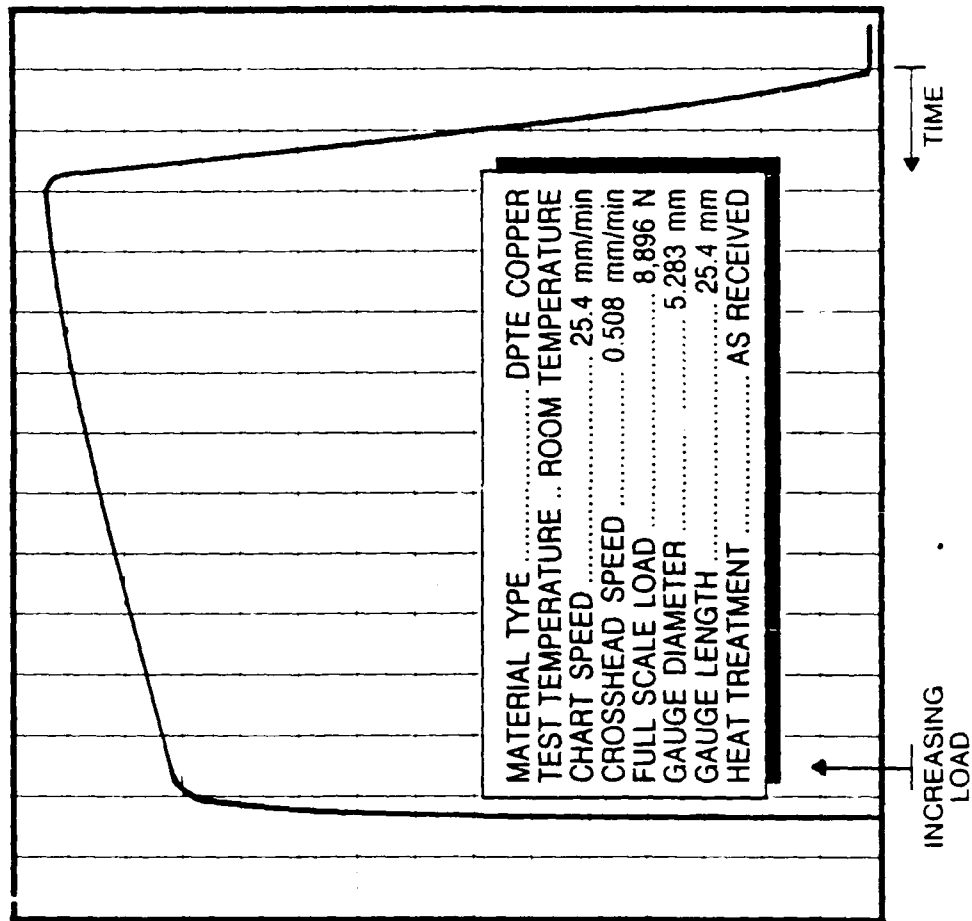


Figure D-2. Load Response of D17E Copper

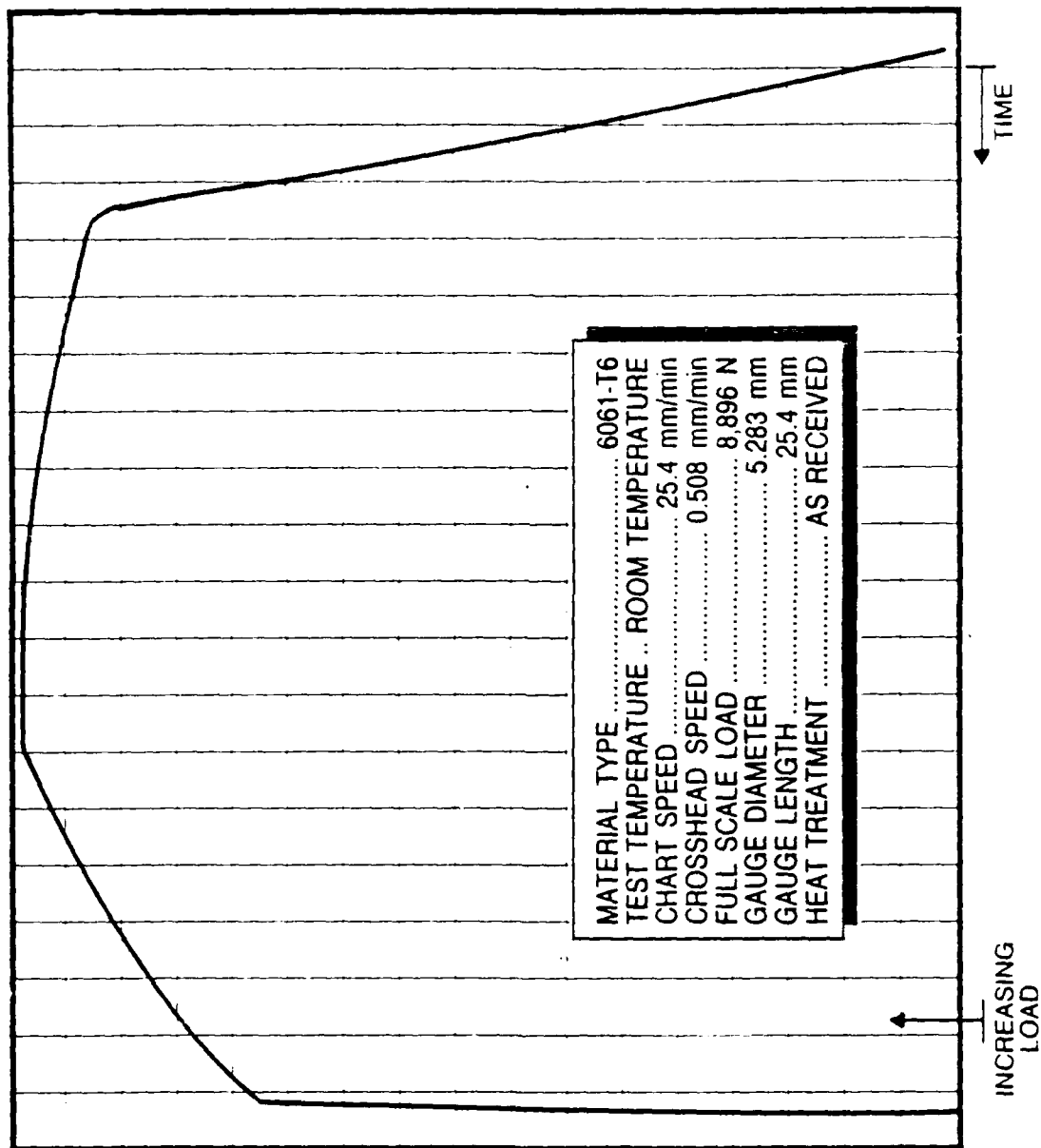


Figure D-3. Load Response of 6061-T6 Aluminum

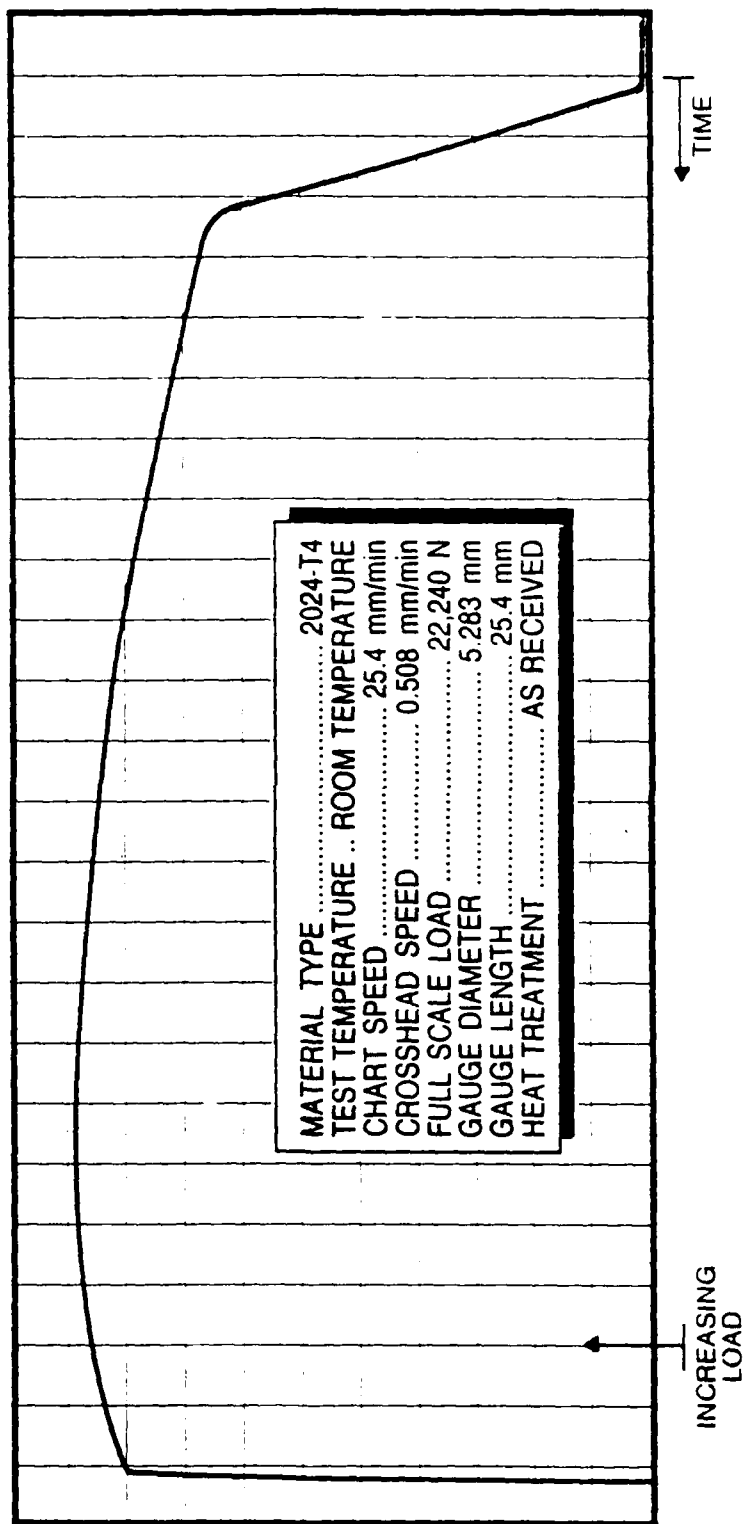


Figure D-4. Load Response of 2024-T4 Aluminum

APPENDIX E
HUGONIOT MODEL

APPENDIX E
HUGONIOT MODEL

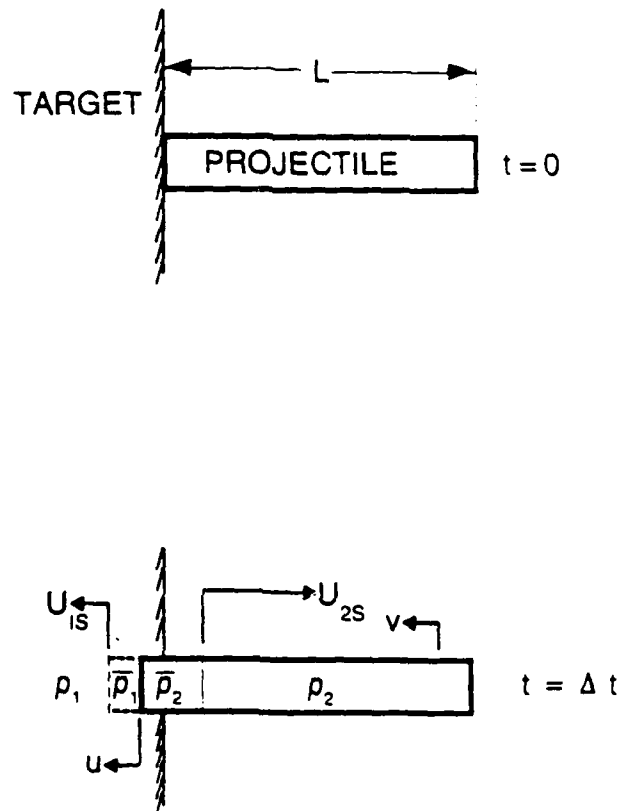


Figure E-1. Schematic Diagram Showing the Parameters Used in the Hugoniot Model

Nomenclature:

- P = Pressure at the target/specimen interface
- ρ_1 = Initial density of the target
- ρ_2 = Initial density of the specimen
- $\bar{\rho}_1$ = Density of the target material behind the shock front
- $\bar{\rho}_2$ = Density of the specimen material behind the shock front
- u = Target/Projectile interface velocity
- U_{1s} = Shock wave velocity in the target

u_{1p} = Particle velocity behind the shock wave
in the projectile
 U_{2s} = Shock wave velocity in the specimen
 u_{2p} = Particle velocity behind the shock wave
in the specimen
 v = Impact velocity
 L = Original length of the specimen
 A = Cross-sectional area, assumed constant
 Δt = Time increment

To predict if deformation twins can form upon impact of pure copper test specimens, a model was developed to predict pressure at impact. The pressure can be determined from a set of equations derived from impulse-momentum and continuity equations, together with Hugoniot relationships. It is assumed for this analysis that the velocity of impact is sufficient to generate shock waves in both the target and the projectile. The analysis is that used in the classical flyer plate experiment, but it is only valid at impact, or for a short time afterwards, in the Taylor test.

At the free boundary of the specimen, radial motion of the material undergoing deformation will invalidate the conditions on the model. Therefore, the model represents only the initial conditions at impact. However, near the axis of the specimen a state of high pressure exists until radial release waves reach this region from the free surface. This region of the specimen was the primary focal point of the microstructural investigation.

Conservation of mass can be used to establish a relationship between the various velocity terms and the density of the material. For the target, the mass under consideration is that volume of material that decreases because of the shock front, Figure E-1. The original mass of material can be equated to the final mass, at some incremental time after impact, as follows:

$$\rho_1 U_{1s} \Delta t A = \bar{\rho}_1 A (U_{1s} - u_{1p}) \Delta t \quad (E-1)$$

Dividing both sides by the common terms gives

$$\rho_1 U_{1s} = \bar{\rho}_1 (U_{1s} - u_{1p})$$

The particle velocity, u_{1p} , in the target is equal to the interface velocity, u . After substituting for the particle velocity, Equation (E-1) can be written as

$$\rho_1 U_{1s} = \bar{\rho}_1 (U_{1s} - u)$$

This expression states that the mass of material must be conserved before and after a shock wave moves through a volume of material.

For the projectile, a similar relationship can be expressed as follows:

$$\rho_2 U_{2s} = \bar{\rho}_2 (U_{2s} + u_{2p}) \quad (E-2)$$

In the projectile, the particle velocity, u_{2p} , is related to the impact velocity, v , and the interface velocity, u , by the expression

$$u_{2p} = v - u$$

Substituting for u_{2p} , Equation (E-2) becomes

$$\rho_2 U_{2s} = \bar{\rho}_2 (U_{2s} + v - u)$$

Using the impulse equation for the same volume of material in the target, a relationship is derived between the velocity of the material and the pressure:

$$PA\Delta t = \bar{\rho}_1 A (U_{1s} - u) u \Delta t \quad (E-3)$$

Dividing both sides by the common terms gives

$$P = \bar{\rho}_1 (U_{1s} - u) u$$

This expression describes the relationship between the velocity variables and the pressure, P . For the projectile, the relationship can be expressed as

$$P = \bar{\rho}_2 (U_{2s} + v - u) u - \rho_2 U_{2s} v \quad (E-4)$$

Equations (E-1) through (E-4) contain six unknown parameters: P , u , U_{1s} , U_{2s} , $\bar{\rho}_1$, and $\bar{\rho}_2$. From shock experiments, two additional expressions can be obtained, giving a relationship between the shock velocities, U_{1s} , and U_{2s} , and the particle velocities, u_{1p} , and u_{2p} . The data from these experiments can be fit to a straight line approximation of the type

$$U_{1s} = a_1 + b_1 u_{1p} = a_1 + b_1 u \quad (E-5)$$

where a_1 and b_1 are quantities determined from shock experiments of the target material, Reference E-1. A similar expression can be used for the specimen material:

$$U_{2s} = a_2 + b_2 u_{2p} = a_2 + b_2 (v - u) \quad (E-6)$$

Solving for the pressure requires that the interface velocity u , be determined. The unknown densities, $\bar{\rho}_1$, and $\bar{\rho}_2$, must be eliminated in Equations (E-3) and (E-4) by substituting from Equations (E-1) and (E-2). The shock velocities can also be eliminated in Equations (E-3) and (E-4) by substituting from Equations (E-5) and (E-6). The pressure equations can be set equal to one another and algebraically manipulated into the following form:

$$u^2 + Mu + N = 0$$

where

$$M = \frac{-(\gamma a_1 + a_2 + 2b_2 v)}{b_2 - \gamma b_1}$$

$$N = \frac{(a_2 + b_2 v)v}{b_2 - \gamma b_1}$$

and

$$\gamma = \rho_1 / \rho_2$$

so that

$$u = \frac{-M \pm \sqrt{M^2 - 4(N)}}{2}$$

Substituting the interface velocity, u , into the equations the unknown quantities, U_{1s} , U_{2s} , \bar{p}_1 , \bar{p}_2 , and P , can be obtained.

A sample calculation using a steel 4340 target material with a copper projectile moving at 200 m/s predicts an interface velocity of 100 m/s. This value of u can be substituted back into the equation set to give a pressure value of 3.9 GPa. This pressure level is almost an order of magnitude higher than the high strain rate flow stress of the material, which is about 0.5 GPa. According to Johari and Thomas, Reference E-2, pressure greater than 2 GPa is sufficient to cause the formation of twins in copper material.

REFERENCES

- E-1. S.P. Marsh, et al, LASL Shock Hugoniot Data, (University of Callifornia Press, Berkely, 1980).
- E-2. O. Johari and G. Thomas, Acta Metall. 12, 1153 (1964).

APPENDIX F
RAW DATA SHEET

APPENDIX F
RAW DATA SHEETS

TAYLOR IMPACT TESTS

TEST
NO. _____

DATE _____

LAUNCHER DESIGNATION _____

STANDOFF DISTANCE _____

TARGET DESCRIPTION: MATERIAL _____

DIMENSIONS _____

HARDNESS _____

OBLIQUITY _____

SPECIMEN DESCRIPTION: MATERIAL _____ SOURCE _____

LENGTH _____

DIAMETER _____

WEIGHT _____

OBTURATION WEIGHT _____

TOTAL WEIGHT _____

PROPELLANT _____ WEIGHT _____

TEMPERATURE _____

HUMIDITY _____

VELOCITY _____

CAMERA _____ FPS _____

TYPE FILM _____ F/STOP _____